Computational modeling of internal mechanical structure of plant cells

Richard Malgat

UNIVERSITÉ DE GRENOBLE

THÈSE

Pour obtenir le grade de

DOCTEUR DE L'UNIVERSITÉ DE GRENOBLE

Spécialité : **Mathématiques et Informatique**

Arrêté ministériel : 7 août 2006

Présentée par

Richard MALGAT

Thèse dirigée par **François FAURE, Arezki BOUDAOUD**

préparée au sein **du Laboratoire Jean Kuntzmann (LJK)**
et de **l'École doctorale EDMSTII**

Simulation bio-informatique de la structure des plantes pour la caractérisation de leurs propriétés mécaniques au niveau cellulaire

Computational modeling of internal mechanical structure of plant cells

Thèse soutenue publiquement le **28 Septembre 2015**,
devant le jury composé de :

Richard SMITH
Directeur de Recherche, Max Planck Institute for Plant Breeding Research, Köln, Rapporteur

René DOURSAT
Chercheur CNRS, BioEmergences Lab, Gif-sur-Yvette, Rapporteur

Évelyne KOLB
Maître de Conférence, Université Paris 6, Examinateur

Bruno MOULIA
Directeur de Recherche INRA, Clermont-Ferrand, Président du jury, Examinateur

François FAURE
Professeur, Grenoble Université, Directeur de thèse

Arezki BOUDAOUD
Professeur, École Normale Supérieure de Lyon, Directeur de thèse

ABSTRACT

Morphogenesis in plants is an active field of research. While the influence of genetics on plant shape has been extensively studied, multiscale rheology : from cells to the whole organism through various tissues or organs, is still poorly analyzed. Nevertheless, it is critical for the understanding of plant evolution, since it directly drives the organism growth.

This work aims at understanding the mechanical characteristics of plant cells, through several realistic and physically based models of various subdomains of our plant archetype : *Arabidopsis thaliana*. In this project, a systematic approach has been developed, where the structures underlying such models rely on experimental data (images of different plant organs), describing precisely the inner structure of *A. thaliana*, which allows the use of realistic meshes for our simulations.

Then, physical modeling allows us to retrieve, through the deformation field of different plant subdomains, the mechanical properties underlying each type of structure described, which is a typical inverse problem applied to a complex biological system. We apply this optimization methodology to several plant organs, beginning with the embryonic stem, then with the root and finally with the meristem, which constitutes the zone where cells can divide and growth typically takes place.

We also develop a theoretical framework, on which biologists may rely, describing a realistic model of plant subsystem, typically a meristem. We hope that this conceptual framework will help experimenters validate hypothesis regarding plant manipulations, for example via Atomic Force Microscopy to experimentally extract mechanical parameters from various plant tissues.

Finally, we present a new approach coupling a coarse physically based simulation to a more detailed one : the Multifarious Hierarchy of Mechanical Models. MHMM is eclectics as it can arbitrarily combine any type of physically based simulation (meshless, modal physics, Finite Elements, and so on). Moreover, it is flexible as it allows the modularity in the various domains containing the underlying models. Finally MHMM is much faster than full Finite Element simulations, at the same level of detail. This should allow the development of fast algorithms for local detailed simulations, as was the case for the numerical Atomic Force Microscope in the previous part.

RÉSUMÉ

Dans le cadre de l'étude de la morphogénèse des plantes, bien que la génétique soit intensivement étudiée, le concept clé de rhéologie à différentes échelles : cellulaire, tissulaire ou de l'organisme entier, qui gouverne directement la croissance des organismes et devrait permettre la connaissance de l'évolution de la plante reste encore très pauvrement analysé.

Ce travail porte ainsi sur la description des paramètres mécaniques des cellules de plantes, à travers la réalisation de modèles numériques physiques et réalistes de différents sous-domaines de l'organisme Arabidopsis thaliana. Dans ce projet, une approche systématique sera développée pour la réalisation de ces modèles où nos structures s'appuieront sur des données expérimentales (images des différents organes de la plante) décrivant précisément la structure interne d'A. thaliana, ce qui permettra l'obtention de structures et maillages réalistes.

Ensuite l'étape de modélisation permettra d'une part de retrouver, à travers le champs de déformation de l'organe décrit, les caractéristiques mécaniques sous-jacentes au modèle, ce qui constitue une forme de problème inverse biologique complexe. Nous appliquerons cette méthodologie à différents sous-domaine de notre plante archétype, commençant par les jeunes tiges, puis les racines et enfin le meristème qui constitue la zone première de croissance de la plante.

D'autre part, nous développerons un cadre théorique, sur lequel pourront s'appuyer les biologistes, décrivant un modèle d'organe d'A. thaliana réaliste, typiquement le meristème, et qui permettra de valider ou d'infirmer certaines hypothèses de manipulations encore sujettes à débat, notamment dans le cadre d'utilisation de microscope à force atomique afin d'extraire expérimentalement les propriétés mécaniques des tissus.

Enfin, nous présenterons une nouvelle approche mécanique hiérarchique couplant des modèles de simulation à différentes échelles : Multifarious Hierarchy of Mechanical Models. Cette nouvelle approche est à la fois éclectique, car elle permet de coupler des modèles physiques variés (sans maillages, physique modale, éléments finis...), mais aussi flexible, car elle autorise la modularité des différents domaines des modèles sous-jacents, et enfin efficace par l'obtention de gains de performance et de temps face à des simulations éléments finis s'appuyant sur le même niveau de détail. Cette approche devrait permettre le développement d'algorithmes rapides pour les simulations physiques où un niveau de détail local est requis. Par exemple, elle pourrait s'appliquer aux simulations de microscope à force atomique décrites dans la partie précédente.

ACKNOWLEDGMENTS

Many people have been involved in this work and it is hard not to forget anyone. I would like to first thank the teams I've been involved with : IMAGINE at INRIA Grenoble, the Biophysics team from the RDP (Reproduction et Développement des Plantes) and the laboratoire Joliot Curie (LJC) in Lyon for their warm welcome.

Among these teams, I have had the chance to personally collaborate with experimenters such as N. Dubrulle and N. Nakayama (thanks for the wonderful images of plant cells), but also with theoreticians such as V. Mirabet and A. Kiss-Gabor (thanks for the various segmentations) in Lyon and M. Nesme in Grenoble or B. Gilles in Montpellier (thanks for the really high-quality work in the last part of this thesis).

Then I am especially grateful to both my PhD directors : F. Faure and A. Boudaoud, in the everyday work for their exceptional scientific skills, but also for their great human qualities in supervising PhD students.

I would also like to express my warm thanks to my whole family for their support during this work : my parents, sister and brother in law, and especially Delphine.

Finally a wink to my really young nephew who will perhaps read this work one day. Who knows ?

This work is dedicated to my sister, Roseline.

OUTLINE

CHAPTER

1

INTRODUCTION

1.1 General overview

Understanding *morphogenesis*, i.e. how organisms achieve their final shape, is a scientific challenge that requires the input of many disciplines : biology, physics, computer science... Biologists commonly agree that gene activity plays a critical part in shape formation [Coen et al., 2004], but only indirectly since shape is determined by the *mechanical elements* of the organism [Mirabet et al., 2011].

Plants are well-suited to investigate morphogenesis, since their mechanics is dominated by a single type of mechanical element, the cell wall [Niklas, 1992]. Accordingly it is essential to quantify the mechanics of cell walls, which is still poorly understood. For instance, elasticity of cell walls, as well as inner cell pressure may vary in experiments in a great range of value (on a ratio from 1 to 1000, as can be found in [Niklas, 1992]), letting the experimentalists uncertain in front of such variability.

The *Morphogenetics* project aims at understanding how shape and architecture in plants are controlled by genes during development. It aims at a better comprehension of plant growth across scale : from single cell, to the whole plant through different types of organs (see section 1.2 for more details on this project). My PhD research is part of the Morphogenetics project, and is thus interested in plant morphogenesis. Our contribution to this project is a **physically based approach of plant cells**. Indeed, mechanics in plants is still poorly understood, while genetics is extensively studied (see [Coen et al., 2004] among many others). While genes control growth in plants, shape is more directly influenced by the mechanical properties of plant cells, since genes drive mechanical properties, which drive the growth. And there may be a feedback loop between physics and genes activity, which influence the whole shape of the organism as stated by [Hamant, 2013].

However, extracting mechanical parameters of plant is still a challenge as explained by [Hild and Roux, 2006], notably for experimentalists whose methods are more and more accurate and sophisticated, but who cruelly lack theoretical models on which to rely. The use of experimental methods to study the mechanics of plants increases exponentially since the past decade [Geitmann, 2006, Routier-Kierzkowska and Smith, 2013, Milani et al., 2013], for experiments of tissues interacting with probes for instance. Available models address mainly simple geometries such as a single cell [Vella et al., 2012b], a single cell layer [Kierzkowska et al., 2012] or non realistic structure like half plane with gradation elastic properties [Lee et al., 2008]. A more detailed overview of computational models in developmental biology can be found in section 1.4.

The lack of precise structure in plant modeling is restraining the development of accurate models. But experimentalists are in need for such models in order to draw conclusion from experiments, since many recent results are still subject to debates, as the first work of [Peaucelle et al., 2011]. In this research, Atomic Force Microscopy is used to deduce mechanical properties of plant samples. It consists mainly in a probe of a size of a few micrometers interacting with a tissue. But hypothesis like the influence of the size of the tip on the measurement of inner layer properties is still cautious to debate.

A great next step to understand the physics of plants may be the development of theoretical, but also *realistic models* of cells, that are crucial for biologists to explain new results. Our method overpass previous limitations as it relies on real topology, originated from confocal microscope images, which gives access to the inside of the structure. We model plant inner cells, which is essential to understand the behavior of plant growth as [Niklas and jr, 1997] explains, but has never been explored.

That is why, our main contributions are **two physically based models** of different types of plant organs, relying on real topology, at cellular level resolution, as well as a **new methodology to couple coarse and detailed simulation**, in order to get a better comprehension of the mechanical properties of these organs and give biologists a theoretical framework on which to rely.

As mechanical properties are key to a better comprehension of growth, the models of plant cells presented in this work will be designed to study the behavior and mechanical characteristics of different plant organs. No genes activity is taken into account. We will consider plants from a pure physical point of view. Shapes are then determined *only* by mechanical parameters.

After this general overview, the introduction will be composed of a global summary of the Morphogenetics project, which constitute the main framework of this PhD research. Then, we will describe the typical plant we are working on : Arabidopsis thaliana, as well as its different organs. Finally, we will briefly introduce the different models developed in this work, which will announce the outline.

1.2 THE MORPHOGENETICS PROJECT

Morphogenetics is aimed at understanding how shape and architecture in plants are controlled by genes during development. However gene regulatory networks act only indirectly on tissue formation, since genetics alone can not explain shape organization [Green et al., 2010]. Collective cell behavior can not be accessed directly through such models. That is why it is essential to study plants at different scales and with different approaches. Plants as biological systems may thus be viewed as complex systems, where “the whole is greater than the sum of its parts”. Here, computational models play a crucial role in order to determine the emergence of collective behavior ([Traas and Moneger, 2010]) and studying the mechanics of plant cells is essential as shape organization is directly linked to these characteristics. That is why the present work aims at analyzing these mechanical properties, even in the most internal subdomains, that should feed back in future studies on gene regulatory networks in order to have a better understanding of shape emergence.

The Morphogenetics project studies the spatio-temporal relationship between genetic regulation and plant shape utilizing recently developed imaging techniques together with molecular genetics and computational modeling. Rather than concentrating on the molecular networks, the project studies plant development across scales. In this context it focuses on the Arabidopsis flower, currently one of the best-characterized plant systems.

Three major research directions :

— Through quantitative live-imaging analysis, or reconstruction at cellular resolution the project tries to determine how specific gene functions affect both growth patterns and the expression of other key regulators, which should constitute an atlas. In particular, by using induced gene disruption together with careful live-imaging analysis, it tries to obtain dynamic, quantitative and causal data that link gene expression and molecular interactions to morphogenesis at a higher scale.

— it aims at integrating the results generated from these experiments in a specially designed database.

— it uses these detailed, multidimensional data as direct input to new predictive computational models for morphogenesis and gene regulation that will then be further tested through subsequent rounds of experimental perturbation and analysis.

By iterating this experimental-theoretical loop the project will continuously refine its models toward a three- dimensional (3D) "virtual flower" at different resolutions, from cells to entire plants. This model will integrate descriptive data with a causal understanding.

This Inria Project Labs (I.P.L.) is an ambitious multidisciplinary project which should last at least four years with many teams involved :

— E.P.I. Virtual Plants (VP) - INRIA/CIRAD/INRA, CR INRIA Sophia-Antipolis Méditerranée – Montpellier
— E.P.I. Imagine (IM) - CR INRIA Rhône-Alpes - Grenoble
— Team Morpheme (MO) - CR INRIA Sophia-Antipolis Méditerranée - Sophia Antipolis
— U.M.R. Reproduction et développement des plantes (RDP) - ENS-Lyon-CNRS–INRA – Lyon : team Meristem and team Biophysics and Development
— U.M.R Physiologie Cellulaire Végétale - CEA-INRA-CNRS – Grenoble : team Regulators of Flower Development (RFD)

These different teams combine their respective skills around these project, which constitute one major axis of research for the next few years to understand plant morphogenesis.

While genetics impact on plant growth is the main goal of the Morphogenetics project, this study needs the comprehension of the mechanical characteristics of living tissues, which are still poorly understood, either at cellular resolution as well as at more global scale.

That is why our *contribution* to this project will be the modeling and understanding of mechanical properties of plant cells, which are at the cross between genetics and plant growth, as they are directly influenced by the genes activity and they do directly influence the whole organism shape. Our typical plant model comes from the description of Arabidopsis thaliana, one of the best characterized plant, and also one of the most studied and cultured in laboratory, and is described hereafter.

1.3 ARABIDOPSIS THALIANA

The plant we are studying is *Arabidopsis thaliana*.

This plant plays the role in plant biology that mice and fruit flies (Drosophila) play in animal biology. Indeed, botanists and biologists began to work on A. thaliana in the early 1900s, and the first systematic collection of its mutations was performed around 1945. It is now widely used in plant sciences, including genetics, evolution, population genetics, and plant development. In 2000, it was the first plant genome sequenced. The reason are multiple :

— it is one of the smallest genomes in the plant world,
— it has a very short life cycle : from seeds to plant to seeds is around two months,
— its size is small, which is convenient to cultivation in laboratory,
— there is no economical interest in this plant, which make share of information easiest from one laboratory to an other.

The different models we developed around Arabidopsis Thaliana rely on a description of each organ of interest. We are interested in three major organs :

1. the *hypocotyl* which is the embryonic plant stem,

2. the *roots*,
3. the *shoot apical meristem* which initiate every aerial organ.

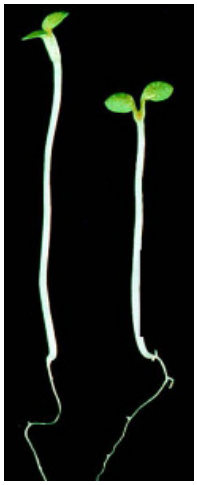

(a) hypocotyls (source Planta 2006)

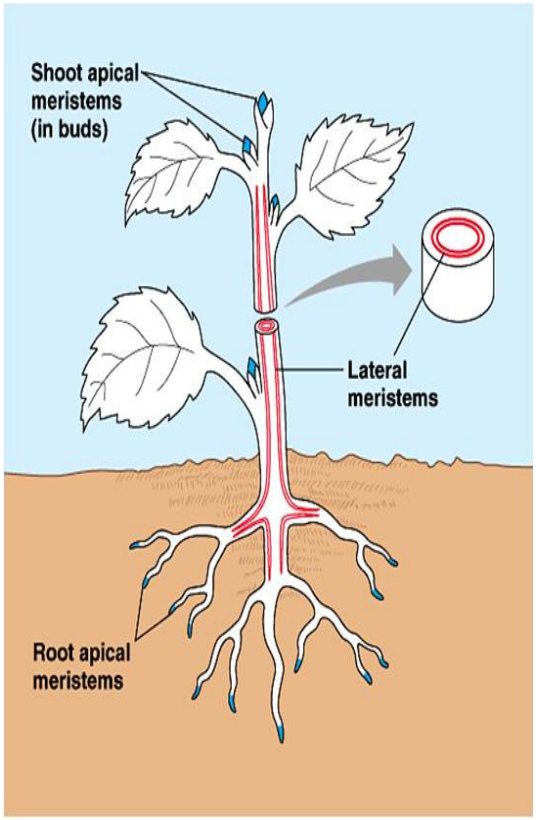

(b) different meristem (source www.ricksci.com)

FIGURE 1.1 – *different plant organs we are interested in*

The *hypocotyl* represented Figure 1.1a (short for "hypocotyledonous stem", meaning "below seed leaf") is the stem of a germinating seedling, found below the cotyledons (seed leaves) and above the radicle (root).

A *meristem* as can be seen Figure 1.1b is the tissue in most plants containing undifferentiated cells (meristematic cells), found in zones of the plant where growth can take place. Meristematic cells give rise to various organs and keep the plant growing. Different types of meristem do exist : the shoot apical meristem (SAM) gives rise to organs like leaves and flowers while root apical meristem (RAM) gives rise to roots. Meristem are key organs in the development of a plant and the comprehension of their properties is essential to understand morphogenesis.

However, physical modeling of these organs is still a challenge, as no models with *realistic geometry* are available. Current mechanical models are limited to simple configurations, such as inflated thin shells that are spherical [Vella et al., 2012b], ellipsoidal [Vella et al., 2012a], half-space with elastic modulus depending on the distance from its plane surface [Lee et al., 2008], or existence of only two types of materials [Roduit et al., 2009].

In this study, we address the question of *internal layers*, by modeling the plant organs with internal layer which may have different properties, e.g. elastic modulus, or pressure, which is crucial to understand plant growth as [Niklas and jr, 1997] states. But until a few years ago, inner plant layers were not accessible in living organisms and have, thus, never been analyzed.

In this work, the method we have developed allows us to handle them and we will often refer to each layer as LX, X being the number of the layer, starting with 1 for the surface and X increasing as we go deeper in the structure. For instance L3 corresponds to the third layer, starting from the surface (see Figure 1.2).

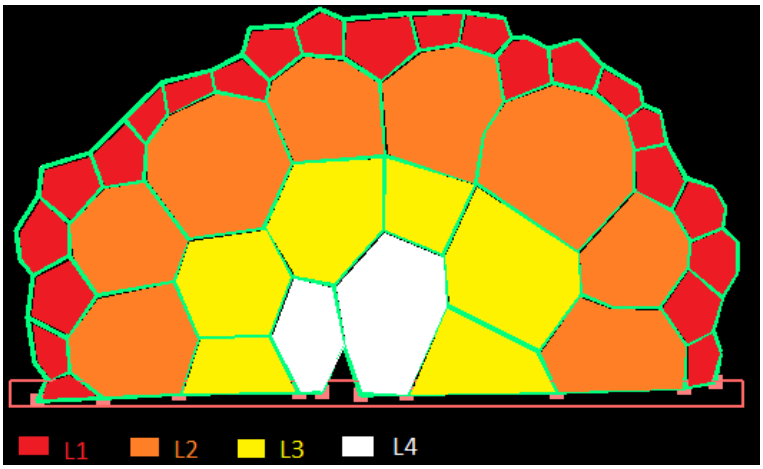

FIGURE 1.2 – *mesh of a cut of a stem : organization by layers*

We will also refer to different types of cell walls as *periclinal* or *anticlinal*, respectively parallel and connecting to the surface. For instance, periclinal walls of the L1 are the surface walls and inner walls not connecting to these surface walls. Whereas anticlinal walls of L1 are the walls connecting to the surface walls (see Figure 1.3).

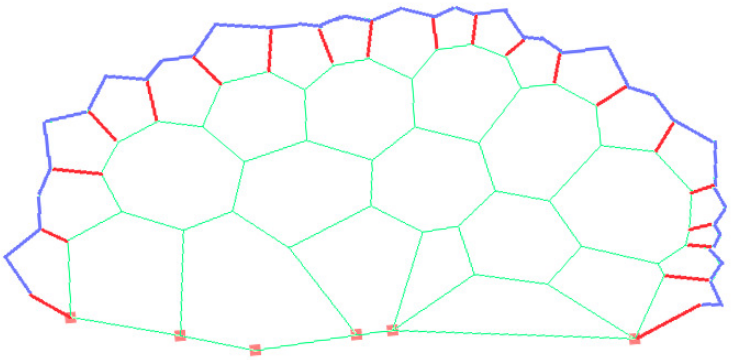

FIGURE 1.3 – *mesh of a cut of a stem : different types of walls. Blue : surface or periclinal walls of L1. Red : anticlinal walls of L1. Green : other internal walls that could also be separated as periclinal and anticlinal.*

The goal is to *go deeper* in the structure as experimental tools are only able to measure, either global properties of the structure, as can be found in [Niklas, 1992, Onoda et al., 2015, Hepworth and Vincent, 1998], and detailed in chapter 2, or local areal properties, with indentation

methods that can be found in [Geitmann, 2006, Routier-Kierzkowska and Smith, 2013, Milani et al., 2013], as explained in chapter 3.

Our models are then designed to describe these typical experimental tools, either measuring *global deformation* of the plant organ considered, or *local deformations*.

For the last part of this introduction, after giving a general overview of the state of the art in the bio-computational area and morphogenesis, I will briefly describe the models developed in this work, i.e. globally deforming models and locally deforming ones, since they give rise to different types of problems.

1.4 State of the Art : Computational models in developmental biology

The word morphogenesis, coming from the contraction of “morpho", which is the form of an organism, and ”genesis“, which stands for the creation, is an active field of research. Studies of morphogenesis from bio-computational point of view include many different area of study. These approaches can be classified following the mathematical rules and assumptions underlying the models developed. We will give an overview of these different models hereafter.

A first interesting approach is given by the network theory as will be discussed in section 1.4.1, since properties of cellular structures can be defined following their underlying gene regulatory networks. Such networks are often represented as boolean as in [Kauffman et al., 2004]. However, it is often not straightforward to analyze such systems, since the data sets generated by gene networks can be really large, even for current computer resources which are still limited. A new trend consist, as in [Moyano et al., 2015], to develop new tools to facilitate their analysis.

A second orientation is given by the L-systems, mostly originated from the work of Lindenmayer in 1968, and that can be found in [Prusinkiewicz and Lindenmayer, 1990]. L-systems consist in a repetitive rule based on a specified grammar in a formal language and from which topology and shape emerge and that are described Section 1.4.2. In this particular modeling, the level of abstraction is different and given a few rules and axioms, complex shapes may arise.

A third interesting point of view is to consider multicellular organism as continuous media as in [CHEN and HOGER, 2000] for instance. Living organisms are composed of thousands of individual cells. Defining a density of cells and its corresponding properties leads to continuous equations like reaction-diffusion, stress-balance or advection, which may be relevant to study the dynamics of growth of living organisms as well as to pattern formation as in the work of Turing in the early sixties or in [Meinhardt, 2008]. This is explained in section 1.4.3.

A fourth approach consist in considering each cell as an individual, possibly containing subcellular species, and derive the dynamics of growth from an agent based modeling. Amongst these, we can separate lattice based models (like cellular automata and Cellular Potts Model originated from the work of [Graner and Glazier, 1992]) and lattice free methods. For the latter, we can distinguish off-lattice models considering only the center of the cells for instance and vertex based models where the cells are considered as polyhedral, and for which a good survey can be found in [Fletcher et al., 2014]. This approach is detailed Section 1.4.4

This work takes place in this last formulation and I will explain the major differences between previous models and ours.

1.4.1 Shape and network theory

Cells characteristics are driven by gene regulatory networks. A better understanding of these properties arise from the network theory. These networks are often represented as boolean as in [Kauffman et al., 2004] and may be used to study cell-fate in flower development as in [Espinosa-Soto et al., 2004]. Their complexity requires the development of new tools to study the major component influencing their structure or to summarize their interactions process as in [Moyano et al., 2015].

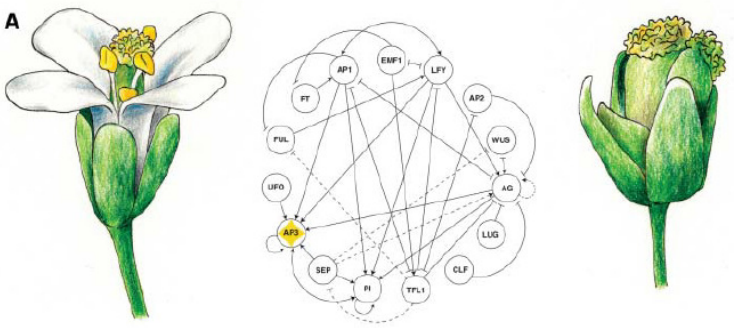

FIGURE 1.4 – *Left : wild type Arabidopsis flower. Identity influenced by gene regulatory network (Middle). Right : mutant Arabidopsis flower (source [Espinosa-Soto et al., 2004])*

However, if gene regulatory network influence shape of living organisms, their influence is not direct as it goes through the structural elements of the organism. That is why we only allude to this approach and focus on literature closer to our work.

An other approach to form emergence that relies on more abstract language and allows to directly visualize tissue development is given by the L-systems theory.

1.4.2 L-systems

L-systems named from the work of A. Lindenmayer, in 1968, are composed of an alphabet and a grammar. The repetitive application of the grammar or rule to the initial axiom gives strings that can be converted into geometric structure. Starting generally from a simple shape represented by an axiom, the repetitive rule allows the construction of complex structures and was used to characterize plant development as in [Prusinkiewicz and Lindenmayer, 1990], but also generate fractals. L-systems can also be coupled with mass-spring systems as in [De Boer et al., 1992], which open the door of coupled systems of different types. More recent studies have been done to facilitate the implementation of L-systems by encoding in Python language as in [Boudon et al., 2012].

However growth emergence within such methods are often limited to repetitive interplay of a given rule and the resulting topology emerges only from branching structure. That is why describing the multitude of heterogeneous cells composing a living organism may appear more efficient as a continuous medium.

1.4.3 Continuous media

The governing equations describing the state of tissues are often the one of continuum mechanics : elastic, plastic or visco-elastic materials are used to account for the global move-

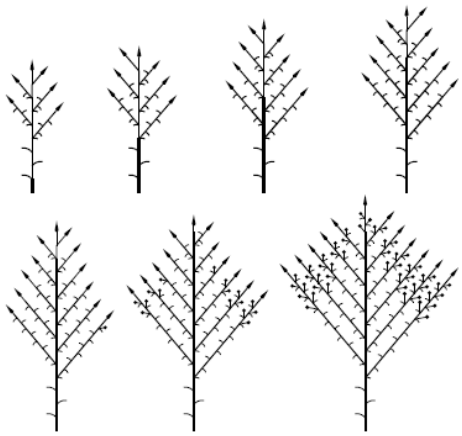

FIGURE 1.5 – *Example of shape emergence from L-system theory (source [Prusinkiewicz and Lindenmayer, 1990])*

ments of cells population as in [CHEN and HOGER, 2000], sometimes coupled with a fluid description. They may also take into account reaction-diffusion or advection process driven by chemical rules as in [Ranft et al., 2010] or driven by a gene regulatory network as in [Kennaway et al., 2011]. These models, since the work of Turing in the early sixties, allows to understand patterns formation in living organisms as in [Kondo and Miura, 2010] A good survey on pattern formation through continuous medium theory can be found in [Meinhardt, 2008].

This theory allows also to study growth and dynamics. Usually, in continuous media theory, two incremental steps are defined : a first growing step where orientation of growth has to be defined through mechanical stress, strain, chemical reactions, gene network... Then, a relaxation following a specified law (elastic, plastic, visco-elastic...) allows finding an equilibrium. Summing up all the incremental step in a cumulative growth step and relaxation step is not straightforward as [Goriely and Ben Amar, 2007] explains. That is why many authors as [Kennaway et al., 2011] use incremental steps to study the dynamics of growth. In this particular study a gene network defines growth orientation through polarity fields. Feedback is then exerted by mechanical interactions following the elasticity theory.

On the contrary, the properties at the sub-cellular or cellular level may appear crucial in some studies. In this case, individual based models seems more appropriate.

1.4.4 Agent based models

Individual based model may rely on a lattice-like cellular automata and Cellular Potts Models (CPM), or be lattice-free-like off-lattice models or vertex based models. Some interesting studies try to link continuous media properties to agent properties in individual based models as in [Byrne and Drasdo, 2009]. But most of the individual based models only account for explicit properties of agents.

Cellular automata

Cellular Automata are discrete models relying on a regular grid. Each element of this grid can take a given number of states. From an initial state and a rule deciding the new state of an element from the current state of its neighborhood, the system goes on and changes state. A popular cellular automaton is the famous game of life from Conway's work in the

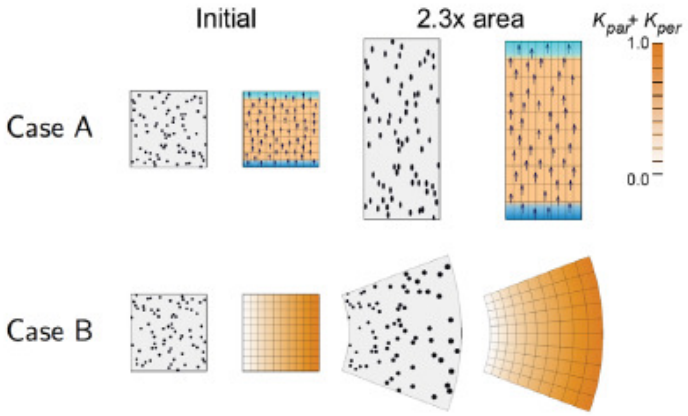

FIGURE 1.6 – *Example of shape emergence from continuous media theory (source [Kennaway et al., 2011]). Column 1 : initial state with randomly distributed cells marked as black circles. Column 2 : visualization of polarity gradient driving growth. Column 3-4 : resulting growth.*

1970s. Since this work, cellular automata have been designed to study numerous problems in morphogenesis, as the morphology of biofilms in [Hermanowicz, , Picioreanu et al., 2001], where various forms may be retrieved, from dense layers to open shapes. Other interesting studies include the dynamics of plants as in [Peak et al.,], where a good agreement is found between the dynamics of stomatal apertures in leaves and a cellular automaton.

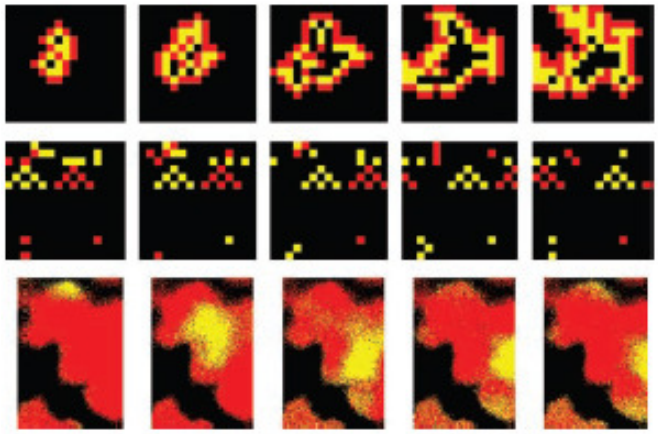

FIGURE 1.7 – *Complex dynamics from cellular automata (source [Peak et al.,]). Top row : a sand pile falls. Middle row : density cellular automaton allows pattern propagation. Bottom row : a leaf under dynamical patchiness of stomata aperture. Red pixels have a higher intensity than they did a few time points in the past, yellow pixels have lower values and dark pixels have the same values.*

Other interesting models relying on a lattice and which may be viewed partially as a generalization of cellular automata are the cellular Potts models.

Cellular Potts model

The cellular Potts model also called extended large-q Potts model or Glazier and Graner model was originally a lattice based model to simulate the behavior of multicellular organisms (see [Graner and Glazier, 1992]). The key idea is the use of a Hamiltonian or energy function defined from the state (or spin) of each individual component and other state like the volume or surface area from the component. A rule decides the next state for the components according to the current state. Cellular Potts models were originally designed to study biological cell sorting process, which leads to the formation of different cell domains. However, it has evolved to a more general framework to study developmental biology for instance. Many morphological processes, from tumor invasion to formation of fruiting body, can be modeled following this approach as can be found in [Merks and A., 2005]. Moreover, they may now be combined with lattice free methods though they are generally used in the context of lattice-based models.

To extract from lattice models which may appear restrictive in a way, off-lattice models have been developed

Off lattice models

In these types of models, only the cells center may be considered for instance, boundaries being given by a radius and cells are considered as spherical, or as ellipsoidal, or even, given a Voronoi tessellation, cell boundaries may be reconstruct. Many studies in this particular area include use of subcellular element as in [Newman, 2005, Sandersius and Newman, 2008], and through multiscale techniques like mean field approximation as in [Newman, 2005] link these subcellular characteristics to more global properties. These methods can be used to study embryogenesis or tumor growth as stated by [Newman, 2005] or to compare with bulk rheology measurements as in [Sandersius and Newman, 2008].

Other interesting studies that may be classified with these types of models are the work of [Douady and Couder,], who developed a general framework to study phyllotaxis and showed that phyllotactic patterns emerge as self-organizing processes in dynamical systems.

Finally a method of interest, in which our work takes place is the vertex based models.

Vertex based models

A good survey can be found in [Fletcher et al., 2014]. The main idea here is to compute forces on vertices of a mesh, generally representing the different cells. A solver allows to move these vertices from one time point to another according to the computed forces.

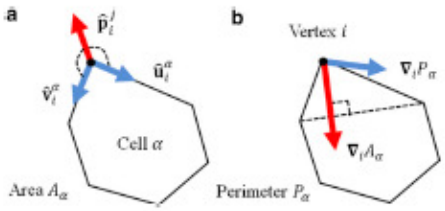

FIGURE 1.8 – *Example of forces acting on vertices in a vertex based model (source [Fletcher et al., 2014])*

These models may be classified following the way forces are computed on each vertex. Forces may be directly computed following some laws of elasticity for instance like in [Weliky

and Oster, 1990, Weliky et al., 1991] or in this work, or models can use an energy formulation from which the forces are derived as in [Honda et al., 2008]. When energy is considered, it may be directly derived to give the force acting on each vertex, or [Merks et al., 2011] for instance uses a Monte Carlo algorithm to minimize this energy and move the vertices according to a Boltzmann probability. Interestingly, in a direct force formulation, studies have coupled the natural Lagrangian method applied to vertices to an Eulerian one representing fluid surrounding the cells as in [Rejniak and Anderson, 2008,Tanaka et al., 2015] or chemical species influencing the cells behavior as in [Smith et al., 2012] or gene regulatory network as in [Shapiro et al., 2013]. However, the interest of all these studies are the dynamics of growth of cell tissues.

In contrast to most studies, we are not interested in dynamics of growth, but in the static behavior of tissues. Therefore, we did not implement any division rule or growth law. Starting from realistic geometries, obtained through confocal images, we try to deduce the mechanical characteristics of the tissues (which are parameters for all these other studies).

This study is more in the line of [Brodland et al., 2010] who implemented Video Force Microscopy, or [Cranston et al., 2010] who computed Cinemechanometry, in order to deduce mechanical stress from in vivo cell displacement. These rising techniques capturing cell mechanics between two images of cellular tissue rely on inverse problem theory. The unknowns are the forces (tensions and pressure) and the known quantities are the displacements observed in the images (or the computed forces leading to such a displacement). Computing the matrices of stiffness and damping on the one hand, the forces on the other hand, allowing the known cell displacements, and summing all forces to zero leads to equations that should be invertible. This allows the inference of mechanical stresses.

However, this work differs from previous one in that we are, in the end, more interested by the mechanical properties than the stress or strain of the cells. Our approach also relies on experiment made at the whole organ scale, or on locally deforming organs.

To our knowledge, large scale experiments in order to infer mechanical properties, mainly rely on continuum mechanics theory and consist in measuring the elastic modulus (or Young modulus) of the organ, which allows the deduction of links between genetics and mechanics as in [Hepworth and Vincent, 1998] on tobacco stems, or [Bargel and Neinhuis, 2004] on fruits, or the inference of specific behavior of tissues, as the sandwich structure of tree leaves from [Onoda et al., 2015]. On the other hand, in order to obtain mechanical properties at a cellular resolution, experiments have been scaled down, with the use of Cellular Force Microscopy or Atomic Force Microscopy as in [Geitmann, 2006, Routier-Kierzkowska and Smith, 2013, Milani et al., 2013], which consist in tissues interacting with probes that are smaller than cell size.

We do combine such nano experimental methods and large scale experiments with vertex based models. In our opinion, more than the model itself, which is quite standard in the bio-computational area, and which is not so different from the ones using a direct force inference as stated above, it is more the whole pipeline we have developed that is of interest, starting from confocal images to get a realistic and reliable geometry and structure, in order to study and infer the mechanical properties of plant cells.

After this general overview of the state of art in the bio-computation and morphogenesis area, I will briefly describe each model developed in this PhD research.

1.5 MODELING

1.5.1 General overview

Through the methodology we have developed, from a pure physical point of view, plant tissue can be viewed as a tiling of a region of space by cells that are approximately *polyhedral* and have a size of a few micrometers. Each cell can be modeled as a liquid under *pressure*, which is in the range 0.1–1MPa [Niklas, 1992]. This pressure is contained by cell walls, which can be modeled as *thin elastic plates* (thickness 0.1–1μm) made of a polymeric material (elastic modulus in the range 1MPa–1GPa), and which lie at the faces of the polyhedra. Instead of a complex biological system involving dozen of free parameters, plant cell properties may be reduced to only few parameters, such as cell wall elasticity, cell wall bending and inner pressure (fig 1.9).

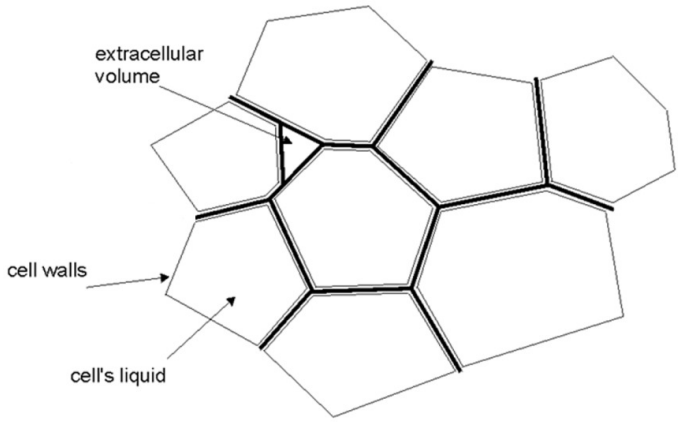

FIGURE 1.9 – *physical representation of plant cells*

That is why current mechanical models in biology as described in [Niklas and jr, 1997] consists in cell wall stretching and inner cell pressure. However such classical models are generally far from realistic concerning the geometry.

Our approach bypass the previous limitations as it relies on *images* from confocal microscope of several plant sub-domains, which gives access to the inside of the structure as can be seen Figure 1.10 and 1.11. Each cell may be described, even in the internal layer that are not directly accessible. This allows us to go deep in the structure and have a realistic topology and geometry. Then, from images meshes are automatically generated for the organ considered, before we physically model the resulting structure.

Following a physically based approach, our methodology can be applied to any plant organ. All our structures are modeled in an unique way, meaning that we consider the different plant cells, either meristematic, hypocotyls or root cells, in a *mechanical* point of view, with the same constitutive elements. These elements are mainly the **stretching** of the cell wall represented by springs in two dimensions and finite elements in three dimension, the **bending** of the cell walls via linear springs depending on the curvature of the element and the internal **pressure**, which is considered homogeneous in every cell.

Our models are designed to mimic the experiments made by biologists, in order to access physical properties of plant cells. These typical experimental tools, analyzing the mechanics of a sample, consists in deforming this sample and studying the deformation field.

Two different types of methodology arise, giving birth to different types of problems :

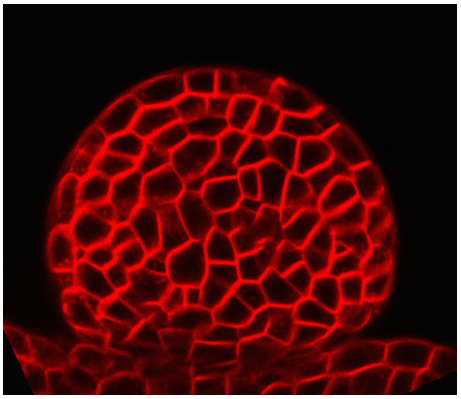

(a) meristem from confocal image

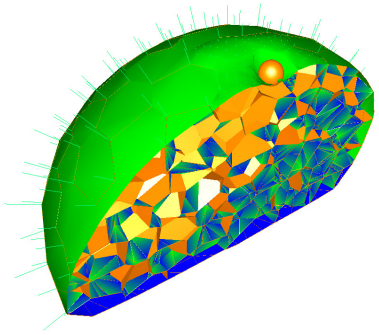

(b) mesh of a meristem

FIGURE 1.10 – *meristem : from image to mesh*

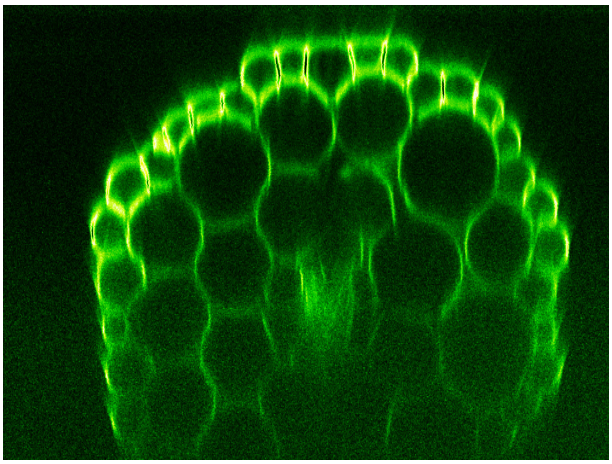

(a) 2D image of hypocotyl

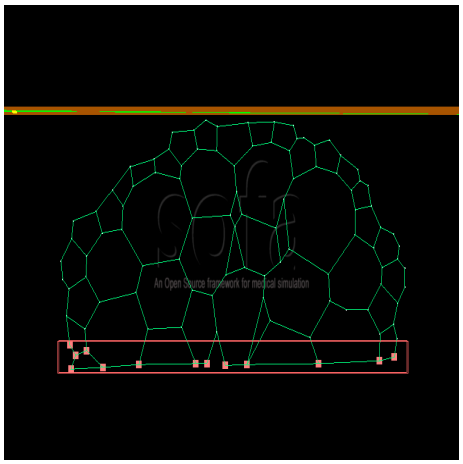

(b) mesh of hypocotyl

FIGURE 1.11 – *hypocotyl : from image to mesh*

— experiments with *global deformation*, which consists in the deformation of the whole organ considered,
— experiments with *local deformation* where only a small part of the organ is deformed.

Following this logic, after an overview of the state of art in the bio-computational area and morphogenesis, our presentation will be divided in three main parts :

1. models of globally deforming organs,
2. models of locally deforming organs,
3. development of a new method to couple a detailed simulation to a coarse one that could be applied to locally deforming problem for instance.

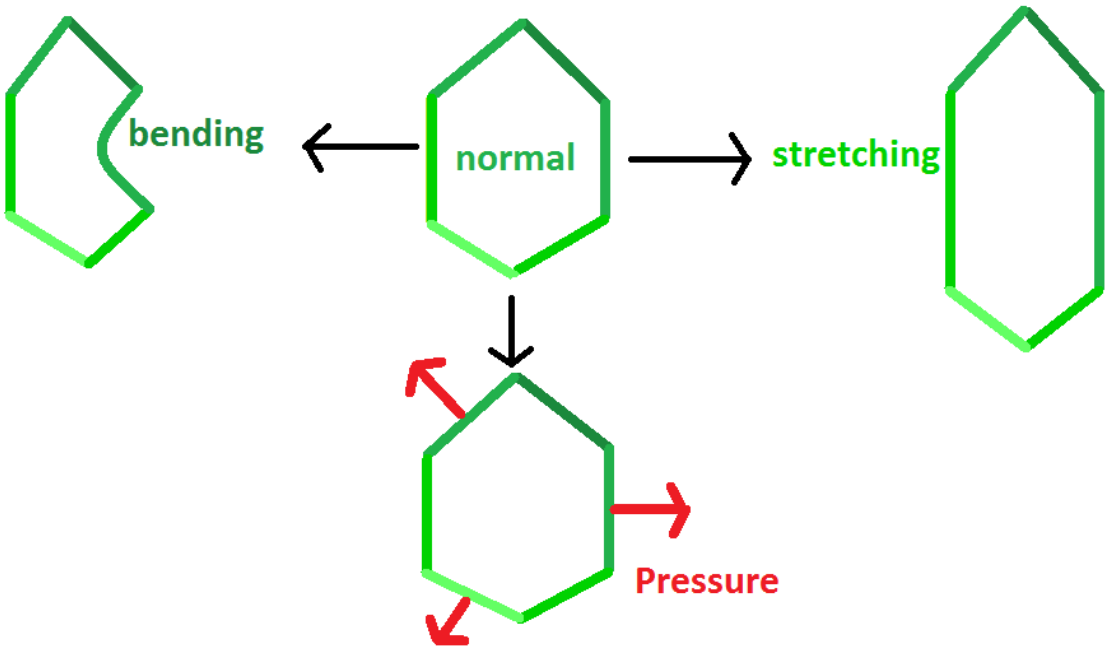

FIGURE 1.12 – *Cell modeling from a mechanical point of view*

1.5.2 2D globaly deforming model

Chapter 2 gives insight into **global deformation models**.

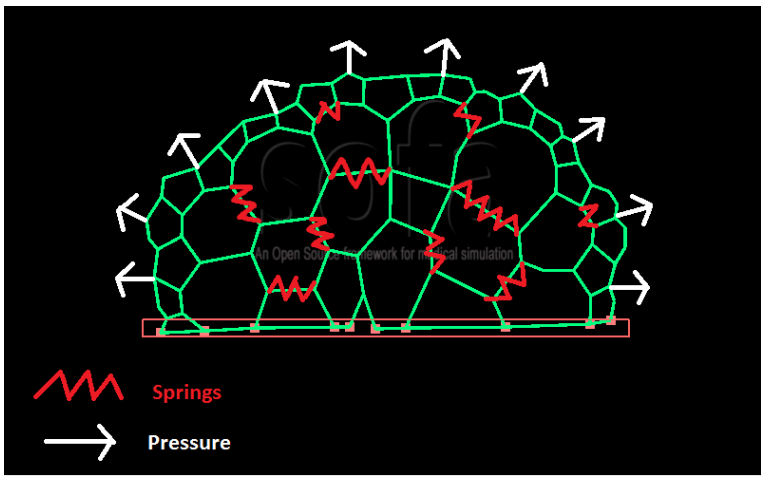

FIGURE 1.13 – *modeling a 2D cut of a stem from a mechanical point of view*

Several plant organs have been experimentally studied through global tissue measurements ([Kerstens et al., 2001, Onoda et al., 2015, Bargel and Neinhuis, 2004, Hepworth and Vincent, 1998]). These experiments consist mainly in tensile and bending measures relying on continuum mechanic theory. However, no precise theoretical framework is yet available to biologists to understand internal cell characteristics, while they seem to play a determinant role in cell mechanics ([Niklas and jr, 1997]).

Despite new promising techniques as Video Force Microscopy from [Brodland et al., 2010], or Cinemechanometry from [Cranston et al., 2010], which deduce mechanical characteristics through deformations, such methods often face ill-posed problems, while they are restricted to surface cells. Indeed, as they rely on inverse problem theory, biological complex systems often lead to poorly conditioned problems as [Brodland et al., 2010, Chiou et al., 2012] did experience. Moreover, no inner plant properties are taken into account.

Our approach is then different from previous one as it relies on inner plant cells topology. Through the development of models with realistic geometries, we enabled the comprehension of internal cell wall characteristics. In a nutshell, we are seeking for static equilibrium through physically based simulation of realistic deformed organs. The mechanical parameters allowing this static equilibrium are then searched in order to minimize the difference between experimental images and the result of the simulation. This is achieved through different optimization algorithms, among which simulated annealing from [Press et al., 2007] and Covariance Matrix Adaptation-Evolution Strategy (CMA-ES) from [Hansen, 2006]. These algorithms allow us to deduce the mechanical properties through the observed deformation field, when the underlying problem is well-posed.

On the contrary, Chapter 3 gives insight into locally deforming models. In this type of problems, the amount of information given by the deformation field of the organ considered should not be sufficient to deduce the mechanical properties of this organ, as only a small part of the region of interest is deformed.

1.5.3 3D locally deforming model

In order to obtain mechanical properties at a cellular resolution, experiments have been scaled down [Geitmann, 2006, Routier-Kierzkowska and Smith, 2013, Milani et al., 2013], notably by using micro- or nano-indentation methods, wherein a micrometric or nanometric probe indents the surface of the tissue while force and displacement are measured.

While biologist are using such methods more and more frequently [Peaucelle et al., 2011, Roduit et al., 2009, Milani et al., 2011, Fernandes et al., 2012, Radotic et al., 2012, Milani et al., 2014], they still need models to help them verifying assumptions and hypotheses, for the different methods they are using. In this chapter, we address the indentation of realistic three-dimensional tissues as can be seen Figure 1.14.

In this type of problem, as the indentation of the structure is only local, the information contained in the deformation field should not be sufficient to retrieve the mechanical properties of the organ. So this part gives a **theoretical framework to biologists** to help them draw conclusion from experiments, but we should not be able to deduce exact values of physical properties from these type of experiments and models.

On addition, Chapter 4 describes a new method coupling local detail on coarse physically based simulation, which could be used for instance to simulate locally deforming zone as described in chapter 3.

1.5.4 Coupling different models

While modal subspace in [Barbič and James, 2005], or frame-based methods in [Gilles et al., 2011] can accurately simulate the coarse motion of an object with a small number of Degrees-of-Freedom (DOFs), they have difficulty capturing the fine-scale details. Instead of requiring fine meshes to capture local detail, resulting in slow computation times, as was the

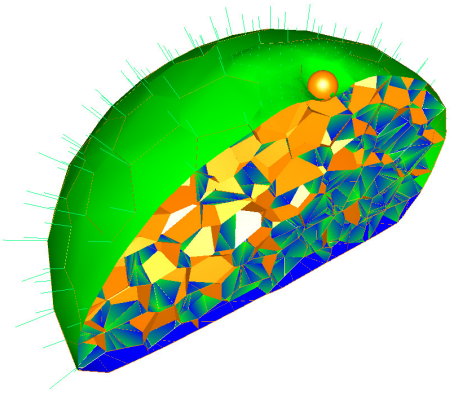

FIGURE 1.14 – *indentation of a three dimensional plant tissue with a sphere in the upper part, acting like Atomic Force Microscopy*

case in chapter 3, or using refinement as in [Debunne et al., 1999, Grinspun et al., 2002]), to accurately capture local detail, we propose a new coupling approach to multi-scale simulation : the **Multifarious Hierarchy of Mechanical Models** (MHMMs).

Multifarious Hierarchies are a general approach that allow a motion to be decomposed using a set of arbitrary, overlapping degrees-of-freedom. For instance, local detail can be added to coarse deformations by embedding a part of the model in a fine FE mesh (Fig.1.15). Thus, MHMMs may be viewed as a new overlapping method, generalizing the work of [Faloutsos et al., 1997], where significant speed-up are obtained in simulation where local detail may be added to coarse deformation.

Finally Chapter 5 sum up the work realized during this PhD. It also concludes by analyzing results and discussing future perspectives.

For every physical model developed, we perform a large number of simulations. That is why we do believe that the Simulation Open Framework Architecture (**SOFA**) software, an open source library designed for physically based simulations in the field of medical simulation and computer graphics [Faure et al., 2012] is well suited to this kind of study.

SOFA is an open-source C++ library primarily targeted at interactive computational medical simulation. It facilitates collaborations between specialists from various domains, by decomposing complex simulators into components designed independently and organized in a scene graph data structure. Each component encapsulates one of the aspects of a simulation, such as the degrees of freedom, the forces and constraints, the differential equations, the main loop algorithms, the linear solvers, the collision detection algorithms or the interaction devices. The simulated objects can be represented using several models, each of them optimized for a different task such as the computation of internal forces, collision detection, haptics or visual display. These models are synchronized during the simulation using a mapping mechanism. CPU and GPU implementations can be transparently combined to exploit the computational power of modern hardware architectures. Thanks to this flexible yet efficient architecture, SOFA

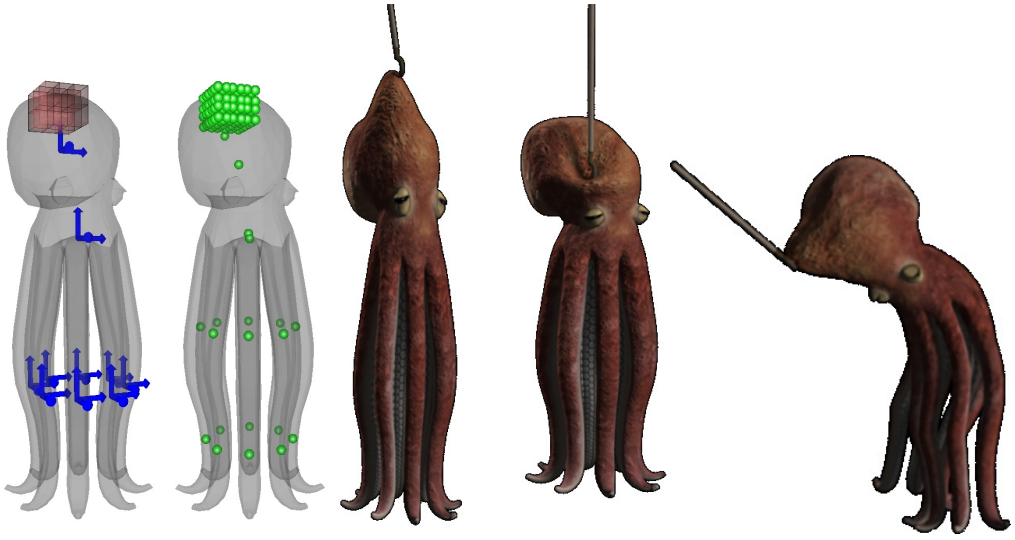

FIGURE 1.15 – *Mixing a coarse frame-based simulation to a local FEM patch with our method : An octopus pulled by a hook. Coarse affine frames (blue), fine embedding FEM (red), integration points (green). The frame-based simulation achieves the global deformations while local deformation are possible around the hook thanks to local FEM.*

can be used as a test-bed to compare models and algorithms, or as a basis for the development of complex, high-performance simulators.

CHAPTER

2

GLOBAL DEFORMATION MODELS OF PLANT CELLS

This part has been done with N. Dubrulle and N. Nakayama for experiments, V. Mirabet and A. Kiss-Gabor for the various segmentations and F. Faure and A. Boudaoud.

2.1 INTRODUCTION

In this part, I describe a physically based model of plant tissue, built to deduce the mechanical properties of plant cells, relying on experiments made at the whole organ scale. To get physical characteristics of any plant structure, common mechanical experiments, involving tensile and bending measures, are made at the organism scale (see [Hepworth and Vincent, 1998, Onoda et al., 2015, Niklas and jr, 1997] where elastic properties of cell walls are deduced for instance). These experiments measure average properties. Indeed, plant cell characteristics can not be directly experienced, since living organisms are composed of thousands of cells. The only possible experiments are then at the whole tissue scale, and constitute, thereby, an indirect measure of cell mechanics.

These large scale experiments rely on continuum mechanics theory and mainly consist in measuring the Young modulus of the organ, which allows the deduction of links between genetics and mechanics as in [Hepworth and Vincent, 1998] on tobacco stems, or [Bargel and Neinhuis, 2004] on fruits, or the inference of specific behavior of tissues, as the sandwich structure of tree leaves from [Onoda et al., 2015], or the anisotropy of onion skin depending of cellulose microfibrils orientation by [Kerstens et al., 2001]. They allow the inference of elastic modulus of the structure considered as a continuum, not the properties of the cells themselves and of the different layers, constituting a complex system. However these properties may vary with the depth in the organ, or follow the complex geometry of the tissue. They are not directly accessible as the real geometry is currently not taken into account in models in the literature.

Furthermore, while several plant organs have been experimentally studied through global tissue measurements, no precise theoretical framework is still available to biologists to quantify inner cell characteristics. In fact, current experiments only apply to the whole organism as a continuum, and theoretical models analyzing the mechanics of plant or animal cells only apply to mono-layer structure as can be found in [Ishihara et al., 2013, Chiou et al., 2012] for instance.

Although last decade has seen new techniques as Video Force Microscopy from [Brodland et al., 2010], or Cinemechanometry from [Cranston et al., 2010] arise, to deduce mechanical stresses from in-vivo cell displacements, these promising new methods have still been unable to take internal layers into account. However, inner layer seem to play a determinant role in tissue mechanics ([Niklas and jr, 1997]). These rising techniques capturing cell mechanics between two images of cellular tissue rely on inverse problem theory. The unknowns are the forces (tensions and pressure) and the known quantities are the displacements observed in the images (or the computed forces leading to such a displacement). These techniques consist in computing the matrices of stiffness and damping on the one hand, and the forces on the other hand, allowing the known cell displacements. Summing all forces to zero leads to equations that should be invertible : basically a stiffness matrix multiplying the unknown forces (tension or pressure for instance) is equal to the known precomputed forces.

This forms an inverse problem that standard inversion matrices techniques may resolve. In this case, the corresponding direct problem is the input of the unknown forces that would lead to the computed forces through the stiffness and damping matrices. But, while they allow the inference of forces and displacements through different time point images, they currently only

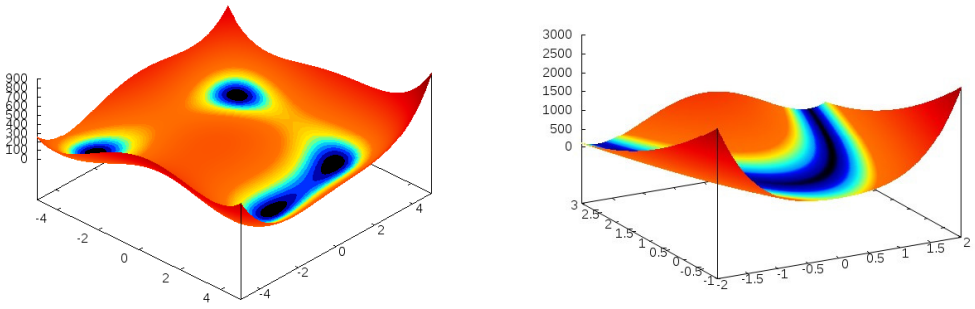

(a) function of inverse problem with several local minima corresponding to an ill-posed problem

(b) function of inverse problem with one global minimum corresponding to a well-posed problem

FIGURE 2.1 – *Two different kind of inverse problems : ill-posed and well-posed*

rely on cell images of the epidermis considered.

Moreover, as is often the case for complex biological systems, such problems are poorly conditioned as [Brodland et al., 2010, Chiou et al., 2012] did experience with Video Force Microscopy and often lead to ill-posed issue as explained by [Engl et al., 2009]. In this case, multiple parameters lead to the same result as can be seen Figure 2.1a, and no precise physical value can be extracted. That is why inferring mechanical properties from complex biological systems is still a challenge as stated by [Hild and Roux, 2006]. And directly inverting a matrix system describing these characteristics constitute a tedious task, even with current algorithms, as the kernel of the matrix equation is often not null. That is why a full space of acceptable solutions may be found with such techniques and no precise physical values may arise.

To get around this difficulty, as the number of parameters in simulation can also grow considerably with the size of the organ considered for physically based simulations (see [Engl et al., 2009]), an easy answer is letting the simulation run until it finds a steady state and thus reach at least a local minimum as [Yadav et al., 2013] did for instance. In this kind of modeling of chemical reactions on the shoot apical meristem, the number of parameters is so large (229 for [Yadav et al., 2013] for instance) that no direct inversion is possible. The author choose instead to input realistic parameters coming from experiments and let the simulation run. Reaching a steady state in agreement with experiments may indicate that they choose the adequate equations. They solve a direct problem instead of trying to solve directly the corresponding inverse problem. But one can not help wondering if the multiple free parameters would not allow to find any desired solution, in agreement or not with the experiments.

That is why we would like to go beyond these limitations, and moreover, determine the mechanical properties of internal layers .

Our approach differs from the previous ones, as explained hereafter.

2.2 Our approach

In physically based simulation of plant tissue, determining the mechanical characteristics of organs through images leads to inverse problem, where the unknowns are the physical properties and the known quantities are the displacements observed in the images (or the computed forces leading to such a displacement).

But as stated in previous section, the inverse problem arising is often not directly invertible and ill-posed.

Our approach relies on images from confocal microscope of plant cells undergoing deformation (deflation or compression). These images are transformed into meshes as explained in section 2.3. As is summed up in figure 2.2 we simulate the direct problem, with, as input, the mechanical properties. This simulation reaches a steady state which correspond to the static equilibrium : the configuration where all forces are balanced. The modeling choices for our simulations will be described in section 2.3. Then, we compare the resulting simulated mesh corresponding to this equilibrium with the mesh from the experimental image through a cost function. Typically, our cost function will be the sum of the difference between the positions of the vertices of both meshes. If both images perfectly match, this error should be null, while it grows as the meshes are different from each other. This will be discussed in section 2.4.4. We enter here a loop, through an optimization algorithm as simulated annealing from [Press et al., 2007], or Covariance Matrix Adaptation Evolution Strategy from [Hansen, 2006], which will be described in section 2.4. The algorithms choose the mechanical properties so that the cost function decreases to its global minimum.

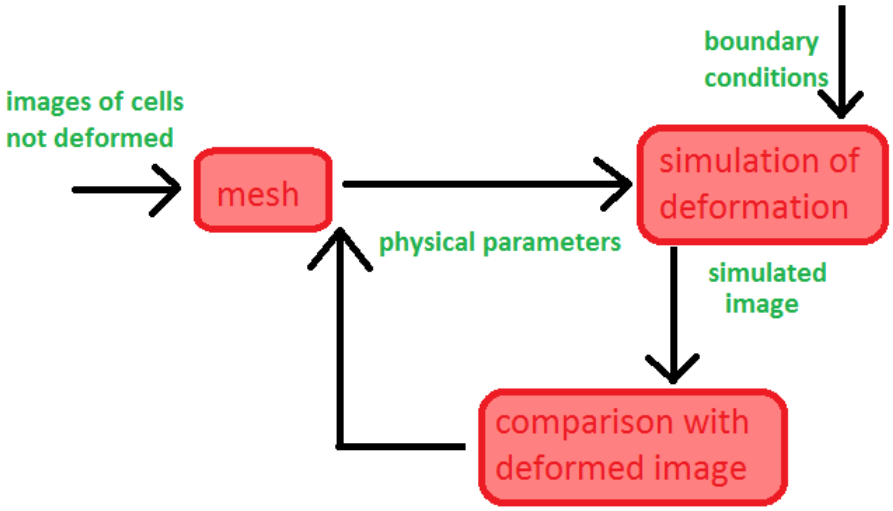

Figure 2.2 – *schematic of our approach : the optimization loop*

In a nutshell, we go over a loop, where each step tries different mechanical parameters, and the optimization process allows to decrease the cost function, which consists in the difference between images and results of simulation.

Thereby, me mix a physically based simulation with an optimization algorithm, in order to deduce the mechanical properties of the structure described.

We will typically consider two different types of deformation :
— deflation of the organ considered,

— compression of a whole organ as can be seen Figure 2.3.

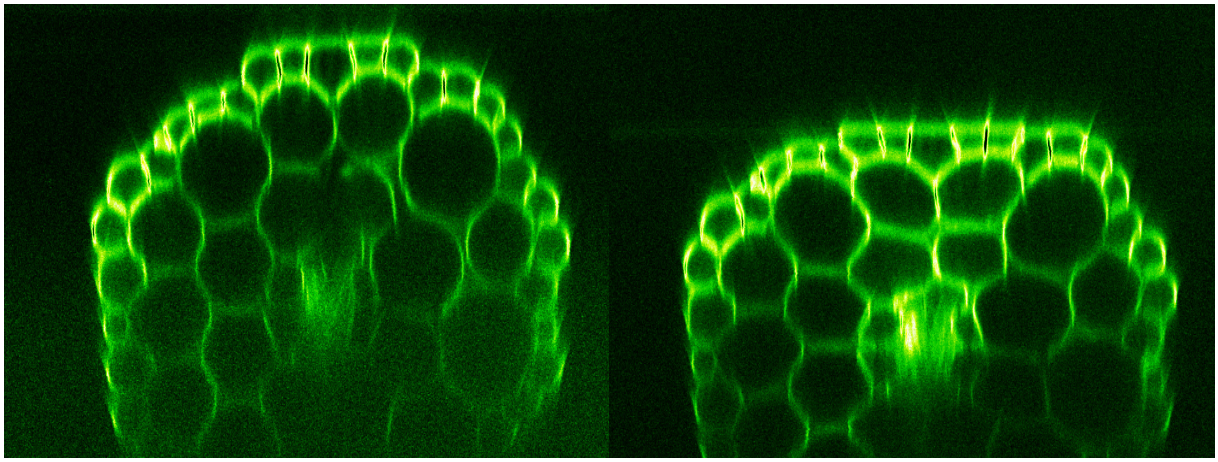

(a) cut of a stem not deformed **(b)** cut of a stem compressed

FIGURE 2.3 – *images of a cut of a stem from normal state to compressed state*

Plants are well suited to this kind of modeling, as their mechanics is dominated by a single type of elements, the cell walls. Each cell can be approximately modeled as a polyhedron, enclosing liquid under pressure. This pressure is contained by cell walls, which can be represented as thin plates made of a polymeric elastic material, and which lie at the faces of the polyhedra.

Thus, plant cells may be physically modeled with only few representative mechanical parameters, such as stretching, inner pressure and bending, which is the core of an homogeneous problem of degree zero as will be discussed in section 2.5.

That is why we can apply this methodology to each plant sub-domain deformed. We focus on cylindrical organs : hypocotyls, roots, stems. Interestingly, deforming these organs may be viewed as a two dimensional problem as these tissues may be considered as infinitely long in one direction compared to the two other directions. We consider a plane perpendicular to the large direction, which reduces the dimensionality of the problem from three to two. That is why we apply the following methodology to the hypocotyl first, before applying it to the roots, for which the same approximation may be valid due to their elongated shape. Finally, we will try to adapt this methodology to the meristem.

Thus, from images of tissues in original state and deflated or compressed, we would like to retrieve the mechanical properties of the plant leading to the deformation observed, through an optimization loop.

In the rest of this chapter, we will describe first the model we have developed. Then we will outline the optimization algorithms we use. Finally, we will discuss results to conclude this chapter.

2.3 MODELLING STEP

The data we have are images of tissues from confocal microscope. Confocal microscope gives access to the inside of the samples as can be seen Figure 2.3. Thus, even internal layers may be accessed, through this imaging technique. We combine this technique with fluorescent

marking of the cell walls. That is why our approach allows to model inner plant cells with a realistic topology. We are able to represent even the most internal sub-domains.

Then, we have to transform these images into a mesh, that can be directly usable in simulations, as stated in figure 2.2. This step has mainly been done by V. Mirabet and A. Kiss-Gabor.

To this purpose, we use the image processing package Fiji from the imageJ software, which is a standard powerful tool to manipulate images. Moreover, it works on every system and is therefor highly portable. On addition images manipulations through this package are quite easy to handle.

A first step consist in applying a Gaussian filter as well as an anisotropic filter through the work of [Schmidt et al., 2014], to smooth the image obtained by confocal microscope and reveal straight sketches. Then, the first segmentation of the first image in the rest state was obtained through a watershed. This technique as implemented in Fiji, takes a grey-level image, that may be seen as a topographic map, where the grey level of a pixel is interpreted as its altitude. "The basic idea of floodind watershed consists of placing a water source in each regional minimum in the map, to flood the entire map from sources, and build barriers when different water sources meet. The resulting set of barriers constitutes a watershed by flooding" (Wikipedia) as can be seen Figure 2.4.

FIGURE 2.4 – *Segmentation with watershed of a 2D cut of hypocotyl, showing single cells*

Through this technique, we get a first segmentation, with every pixel having a value depending on the cell it belongs to. Then, we have to transform this segmentation into a mesh. This second step is done by selecting the pixels corresponding to a triple or more junction, which means that they are at the intersection of several cells. These will be our vertices. Afterwards, we trace the edges between each vertex. Only the surface is handled with one more vertex per edge to allow for a curved wall. Given the curvature of the surface edges, three vertices compose such an edge : two are the extremities and one is at the cross between the edge and the perpendicular bissector of the two first points.

Once the first mesh is achieved, we apply a deformation grid onto the image not deformed through the bunwarpJ plugin of the software based on the work of [Arganda-Carreras et al., 2006] to get the deformed mesh corresponding to the deformed image, with a correspondance vertex by vertex and cell by cell. This method, also called deformable template matching gives us the mesh not deformed as well as deformed and a correspondance is realised between vertices and cells of each mesh.

Finally, as we can see Figure 2.3 that the lower half part is not usable due to the weakness of the signal, we can also mesh only half the cut of the hypocotyl. Thus, we consider that the deformation is symmetric from the upper part to the lower part and apply the deformation only to the upper part, which is consistent with the natural symmetry of the hypocotyl. The symmetry may be achieved by different ways. Either we can fix the lowest vertices in the position of the

deformed mesh and the error made on these vertices will be null. Or we can let them slide on a horizontal line taken at half the hypocotyl and consider the deformation as symmetric. Both methods give us the same optimization results, but the first one is a bit more precise as a null error is made on these vertices.

Once we have our meshes, we still need to describe them physically. As stated in section 2.2, plant cells may be viewed as polyhedra (given by the meshes), with elastic cell walls, that can be modeled by springs in two dimensions, submitted to internal pressure. Moreover, we consider bending in some cases of junction.

We will describe each of these elements hereafter.

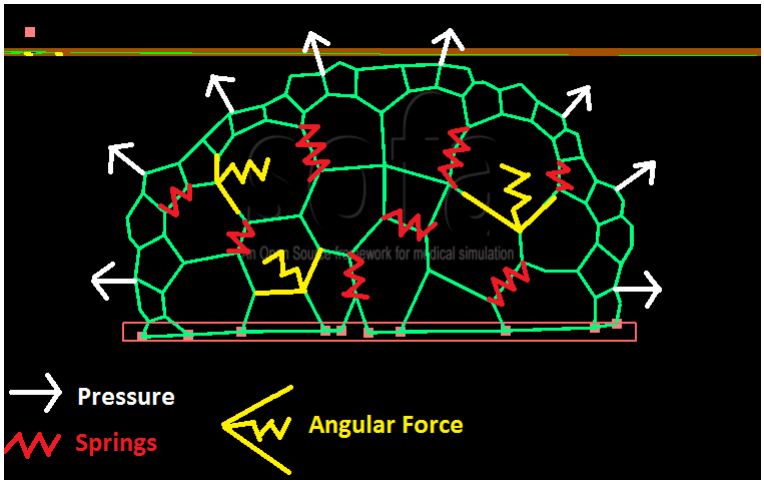

FIGURE 2.5 – *physical model of a 2D cut of hypocotyl*

2.3.1 Elasticity of cell walls

As this model is developed in 2 dimensions, considering the cell walls as elastic may lead to a mass-spring model : each vertex of the structure receive some mass, that we choose uniform in practice, without any prior knowledge of the mass distribution of cells. Which means that every vertex receive the same amount of mass. Notice that, as we are seeking for static equilibrium, the mass influence should be negligible. This will be discussed in section 2.3.4. Then each cell wall is modeled as a spring (see Figure 2.6).

Notice also that each type of cell-wall (e.g. surface cell walls, that are also the periclinal walls or wall tangent to the surface of the first layer of cell or L1 ; anticlinal walls or wall perpendicular to the surface of L1 ; cell walls of L2, etc) may be modeled with different stiffness. This will be discussed in section 2.5

The force acting on each vertex at the extremity of the spring (i.e. the cell wall) is then :

$$F = k_s.(l - l_0)U \tag{2.1}$$

with k_s the spring stiffness, l current length, l_0 rest length and U unit vector in the direction of the spring. k_s may also be decomposed, for each wall in :

$$k_s = \frac{Et}{l_0}$$

with E, the elastic modulus of the wall considered (also called Young modulus) and t the thickness of the wall, the product Et being the surface Young modulus.

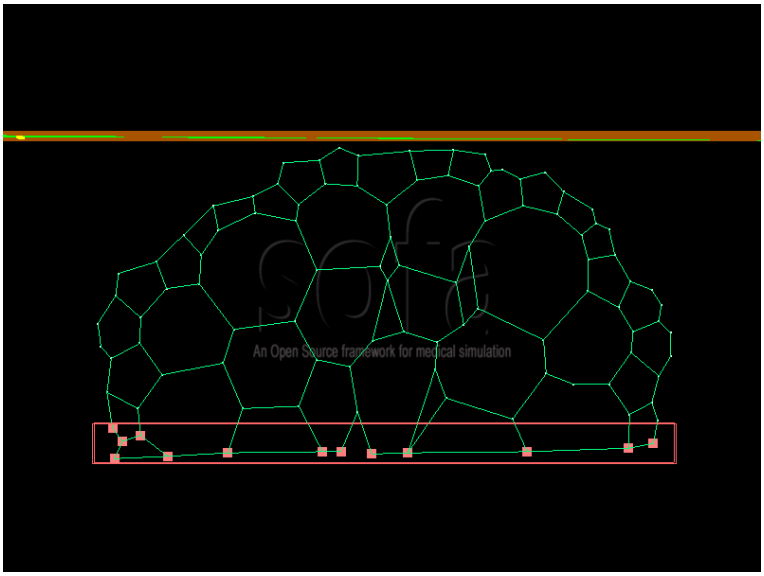

FIGURE 2.6 – *mass-spring model of a 2D cut of stem*

As we use an implicit Euler solver or a static solver (see section 2.3.4) to compute the displacement of the vertices due to the forces, we also need the derivative of the force with respect to the displacement.

The force variation dF comes from length variation dl and unit vector variation dU.

$$dF = k_s.dl.U + f.dU \text{ with} f = \|F\| \tag{2.2}$$

Moreover,

$$dU = \frac{1}{l}.\left(I - U.U^T\right).dX$$

where $dX = dX_1 - dX_0$ with 1 and 0 the indices of extremity of the spring and I the identity matrix.

We also have

$$dl = U^T.dX$$

Finally,

$$dF = k_s.U.U^T.dX + \frac{f}{l}.(I - U.U^T).dX = \left(\left(k_s - \frac{f}{l}\right).U.U^T + \frac{f}{l}.I\right).dX \tag{2.3}$$

These are standard, mass-springs system equations. But our structure undergoes also some inner pressure.

2.3.2 Pressure

The pressure is a force acting on each vertex and perpendicular to the wall the vertex belongs to. The pressure is considered homogeneous in each cell but may be different for different cells, or different layers. Typically, experiments in roots may indicate that pressure in internal layers may be slightly higher than the one of peripheral cells (or L1 cells). It is given by :

$$F = P.\frac{l}{2}U^{\perp} \tag{2.4}$$

with P inner cell pressure, l wall length and $U^{\perp}$ unit vector perpendicular to the wall and going out of the cell. The $\frac{1}{2}$ arise since the pressure is split between the two vertices.

As was the case for the springs, we need to compute the force variation dF with respect to displacement. This variation arises with the length variation dl of cell wall, and with the variation of unit length vector $dU^{\perp}$.

This may be written as follows :

$$dF = P\frac{dl}{2}.U^{\perp} + f.dU^{\perp} \text{ with} f = \|F\| \tag{2.5}$$

As well as above :

$$dl = U^T.dX$$

and :

$$d(U^{\perp}) = (dU)^{\perp} = \left(\frac{1}{l}(I - U.U^T)dX\right)^{\perp}$$

A the matrix 3×3 defined by :

$$A = \left(\frac{1}{l}(I - U.U^T)\right)$$

Then we have :

$$(A.x)^{\perp} = \begin{pmatrix}0\\0\\1\end{pmatrix} \wedge (A.x)$$

Because, in practice, we take the vertices of the cells ordered in the trigonometric way

Then :

$$(A.x)^{\perp} = \begin{pmatrix}-a_{10} & -a_{11} & 0\\ a_{00} & a_{01} & 0\\ 0 & 0 & 0\end{pmatrix}.x = A^{\perp}.x$$

Finally :

$$dF = (\frac{P}{2}U^{\perp}U^T + A^{\perp}).dX \tag{2.6}$$

But, beyond pressure and cell wall elasticity, we decided to introduce some bending, so that the mesh respect the junctions between cells, and does not deform too much around these junctions.

2.3.3 Bending

Bending is a force that reacts to angle displacements. An easy, but not efficient way to compute bending is to compute the various angles at each cell junction of our structure. But as we only have access to the positions of vertices of our structure, computing these angles do require a call to the inverse cosinus function : $\arccos$, which is computationally expensive. As we are seeking for fast algorithms, we have decided to implement some bending springs rather than using this function.

An obvious way to implement these springs would be to apply them to the vertex concerned by the angle (see Figure 2.7). But this method creates an increase in length of the wall and,

thus, a counter force since these walls are modeled by springs. So, a better approach consist in splitting this force in two terms of equal norm, applied to the extremity of the walls and perpendicular to these walls.

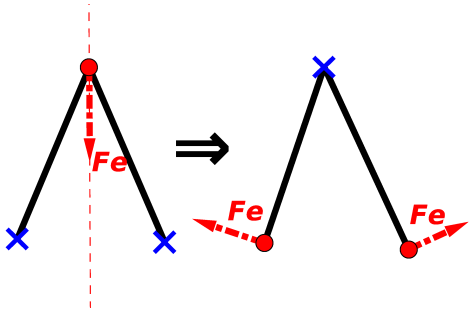

FIGURE 2.7 – *computing bending in two different ways : forces of bending can act on different vertices*

The force acting on each vertex being proportional to the angular variation :

$$F = k\Delta\theta \tag{2.7}$$

with k, the bending stiffness and $\Delta\theta$ the angular variation. But we only have access to the cosinus of the angle, through the vertices positions (with the scalar product for instance).

Instead of computing the $\arccos$ function, we can interpolate this latter by a polynomial function of degree 3 for instance. Lagrange interpolation at the points $-1, -\frac{1}{2}, \frac{1}{2}, 1$ gives Figure 2.8 :

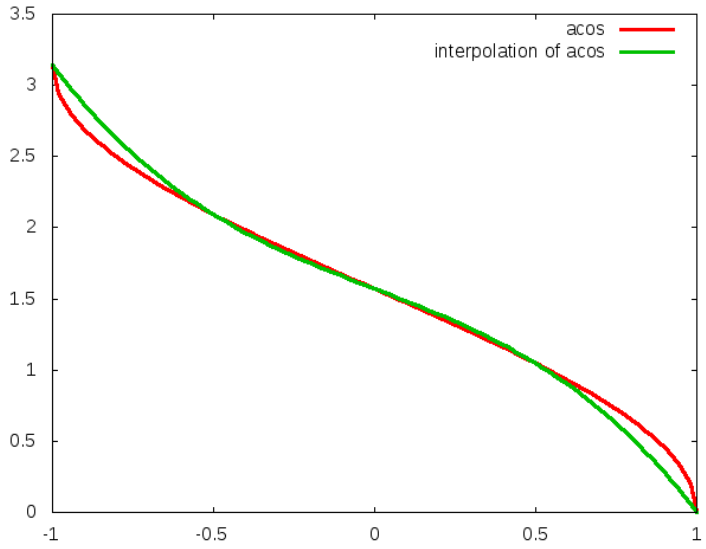

FIGURE 2.8 – *interoplation of the* $\arccos$ *function through Lagrange method*

With this choice, the error is given Figure 2.9.

This error is never up 0.18 radians and, if we are at angular value for instance up $\frac{\pi}{4}$, it is under 8%. Moreover, with this method the error does not depend on angular variation : even if we have some high angular variation, the error stays the same.

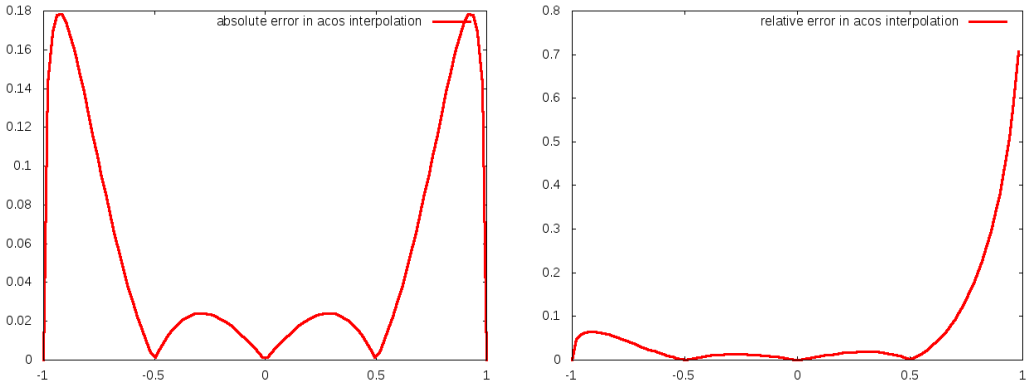

(a) absolute error of interpolation of arccos with Lagrange method

(b) relative error of interpolation of arccos with Lagrange method

FIGURE 2.9 – *error on the interpolation of* arccos *with Lagrange method*

So this seems a really efficient and yet physically plausible way to compute bending in two dimensions.

Figure 2.10 sums up inputs and outputs of the model.

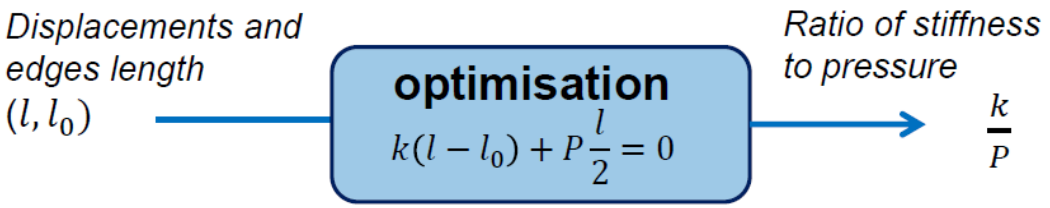

FIGURE 2.10 – *summing up the input and output of the model*

Now that we have designed all our force-fields, we still need to compute and derive the underlying equations of physics to link them.

2.3.4 Solving the equation system

Solving the equation of mechanics arising from our models may be done in various way, which all originate from the same following equation 2.8, but may vary with the different approximations made afterwards. From this equation of dynamics, we can derivate the solution of our simulation in a dynamic form as will be explained in equation 2.10, but also in a static form as will be stated in equation 2.13. Both method have their benefit and their drawback : the static form being more efficient, but less stable the way it is implemented in SOFA, while the dynamic form is more stable, but much more slowly.

Starting with the displacements x_i of each vertex of our model, as well as with the corresponding velocities v_i and forces f_i, the principle of dynamics writes :

$$\frac{d}{dt}\begin{pmatrix} x \\ \dot{x} \end{pmatrix} = \frac{d}{dt}\begin{pmatrix} x \\ v \end{pmatrix} = \begin{pmatrix} v \\ M^{-1} f(x, v) \end{pmatrix} \tag{2.8}$$

with M the mass matrix and f a function dependent on the displacements and velocities.

An easy, but not efficient way would be to use an Euler explicit solver, where the above equation may be rewritten as follow :

$$\begin{pmatrix}\Delta x\\ \Delta v\end{pmatrix} = \tau \begin{pmatrix} v_0 \\ M^{-}1 f_0\end{pmatrix} \tag{2.9}$$

where τ denotes the time step, and $f_0 = f(x_0, v_0)$. Using such a forward approach, the time step should be chosen smaller enough to ensure stability. So the advantage of this method is that, with a sufficiently small time step, stability is ensured. But one weak point is that simulations may be extremely slow to converge to an equilibrium, due to the lack of damping and thus small oscillations may appear before converging. Moreover it does not allow large time step, and is therefore more slowly than implicit methods.

So, an obvious better method is to use an implicit Euler solver for instance based on the work of [Baraff and Witkin, 1998]. In this work, equation 2.8 for the implicit backward Euler method then writes, with a spatial discretization :

$$\begin{pmatrix}\Delta x\\ \Delta v\end{pmatrix} = \tau \begin{pmatrix} v_0 + \Delta v \\ M^{-1} f(x_0 + \Delta x, v_0 + \Delta v)\end{pmatrix} \tag{2.10}$$

A first order Taylor expansion in f is given by :

$$f(x_0 + \Delta x, v_0 + \Delta v) = f_0 + \frac{\partial f}{\partial x}\Delta x + \frac{\partial f}{\partial v}\Delta v \tag{2.11}$$

and solving for v, this can be rewritten as :

$$(\mathbf{I} - \tau\, \mathbf{M}^{-1}\mathbf{D} - \tau^2 \mathbf{M}^{-1}\mathbf{K})\Delta v = \tau \mathbf{M}^{-1}(f_0 + \tau \mathbf{K} v_0) \tag{2.12}$$

where τ denotes the time step, $\mathbf{K}$ the stiffness matrix ($\mathbf{K} = \frac{\partial f}{\partial x}$) and $\mathbf{D}$, the damping matrix ($\mathbf{D} = \frac{\partial f}{\partial v}$). To enter in more detail the derivation, we refer the reader to [Baraff and Witkin, 1998]. We have chosen $\mathbf{D}$ as the popular Rayleigh assumption : $\mathbf{D} = \alpha\mathbf{M} + \beta\mathbf{K}$. But notice that, as we are seeking a static solution, the influence of $\mathbf{D}$ as well as $\mathbf{M}$ is negligible.

The stiffness matrix depends on each force field, i.e. springs, pressure, bending, and is computed for each force field. In the general form, it can be written as :

$$\mathbf{K}_{ij} = \frac{\partial f_i}{\partial x_j}$$

and its general terms have been explained in the previous sections.

This kind of solver allows choosing higher time step. Moreover, while the damping term does not affect the static equilibrium reached at the end of the simulation, it can greatly improve the stability.

The faster way to solve the equations appears to be a static solver as we are seeking for static equilibrium. The static solver we use has the same approach than the implicit backward Euler previously described, where the terms depending on the mass and damping are just removed. So the equations for the static solver write :

$$\begin{pmatrix}\Delta x\\ -\tau^2 \mathbf{K}\Delta v\end{pmatrix} = \tau \begin{pmatrix} v_0 + \Delta v \\ f_0 + \tau \mathbf{K} v_0\end{pmatrix} \tag{2.13}$$

In practice, solving the system with high accuracy and stopping the simulation when the vertices do not move over a certain threshold (around 10^{-5} the size of the mesh), the static

solver may converge within a few dozen of time steps, while the implicit backward Euler one needs a few thousands and sometimes the Euler explicit one needs a few dozen of thousands. But due to damping, the implicit backward Euler one is much more stable. So when contacts are handled, the implicit solver may be required. For instance, when compressing the stem, an implicit solver may be required, whereas, when plants just move from a rest-state with no pressure (in a plasmolysed state) to an inflated state, a static solver is robust enough and much faster.

Beyond the rapidity of each method to solve the equations of dynamics, the results with the three different types of solver are the same. That is why we typically always use a static one when no contacts are required, while we use an implicit backward Euler one when contacts are needed.

We suspect that using a non linear solver may accelerate the convergence, but defer this to future study.

Thus we can simulate the behavior of the structure from a mechanical point of view. But as we are seeking mechanical parameters fitting the images (recall Figure 2.2), we need to design an optimization algorithm to solve our inverse problem. Indeed, the static equilibrium reached at the end of the simulation is used only for the comparison with images, which constitutes our cost function.

Then, the optimization loop requires as input physical properties and should be carefully designed as we have no prior knowledge on the landscape of our error function, which may be rough and non convex.

2.4 OPTIMIZATION

We have tried various optimization algorithm. But as we have no access to the gradient of the function to be minimized, the optimization algorithms we need should only call the function, not its derivatives. That is why we tried determinist algorithms like Powell algorithm which is well designed to fit quadratic problems in any dimensions, and stochastic one like simulated annealing and Covariance Matrix Adaptation - Evolution Strategy (CMA-ES).

2.4.1 Powell algorithm

We tried first the classical Powell algorithm from [Press et al., 2007]. This algorithm uses the parabolic interpolation and Brent's method in one dimension. For each step, we search the minimum along one direction with the Brent's method. Then we use Powell's method to find a new conjugate direction, i.e. a new direction orthogonal to all the dimensions already chosen. In a nutshell, Brent's method tries to fit the function to be minimized by a polynomial of degree 2 as can be seen Figure 2.11. Given 3 points and their function evaluation, we find the parabola which fits these 3 points and the minimum is taken as a next point. We then replace this point instead of one of the three first points and continue iteratively until the minimum is reached. Then Powell algorithm replace the direction by a new conjugate one.

For further details we refer the reader to [Press et al., 2007].

But we realized that starting from two points near each other gave some really different results. This could be the result of a rough landscape for the function to be minimized as well as the fact that the problem is ill-posed. To determine the part of the landscape in the evaluation process, as well as the adequacy of the algorithm used to solve our problem, we choose two stochastic optimization algorithms : simulated annealing and Covariance Matrix Adaptation Evolution Strategy (CMA-ES).

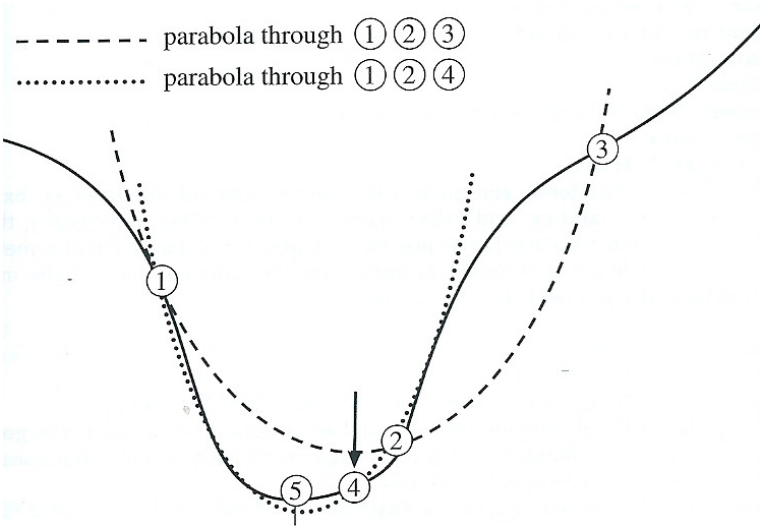

FIGURE 2.11 – *Brent's method in one dimension to find a minimum with parabola interpolation : source [Press et al., 2007]*

2.4.2 Simulated annealing

We implement the simulated annealing algorithm found in [Press et al., 2007]. This method uses a non stochastic algorithm (here the downhill simplex method) and search in a random direction around the point defined as a starting point.

The downhill simplex method is a multidimensional search which takes a simplex, i.e. a geometrical convex figure in any dimension (like a triangle in 2D or a tetrahedron in 3D). Then for each step the algorithm may :

— do a reflection of the simplex from one point (with the highest function evaluation) through the opposite face.
— expand in one direction of lowest function evaluation
— contract itself in one or multiple direction if finding a valley floor

Then the simulated annealing algorithm introduces a notion of temperature : when this temperature is high (at the beginning of the procedure), a large region is explored in a stochastic way. From one step to another, we always accept a downhill step, but sometimes also accept an uphill step, with a probability proportional to the temperature. This allows us not to stay in a local minimum but also explore an entire region.

When the procedure goes on, the temperature is reduced. By reducing this temperature we are back on the original non stochastic method and find a minimum.

Finally, we also implemented one of the key algorithm in non convex optimization for rough landscape : Covariance Matrix Adaptation - Evolution Strategy.

2.4.3 Covariance Matrix Adaptation - Evolution Strategy

Covariance Matrix Adaptation - Evolution Strategy (CMA-ES) is a robust optimization algorithm designed for non convex function. As can be seen Figure 2.12, multiple function evaluation are realized at each step, and a recombination of these evaluation is made to evaluate the next step. An evolutionary algorithm is broadly based on the principle of biological evolution, namely the repeated interplay of variation (via recombination and mutation) and selection : in each generation (iteration) new individuals (candidate solutions) are generated

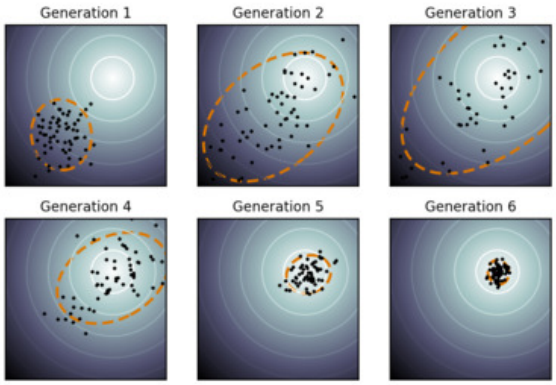

FIGURE 2.12 – *Covariance Matrix Adaptation - Evolution Strategy in action (source wikipedia) : 6 steps are sufficient to reach a minimum*

by variation, usually in a stochastic way, of the current parental individuals. In an evolution strategy, new candidate solutions are sampled according to a multivariate normal distribution. Basically, the idea here is to update the distribution of the new candidates to be evaluated, by updating the covariance matrix of the distribution of these samples.

The detailed algorithm as well as its implementation can be found in [Hansen, 2006].

Covariance Matrix Adaptation - Evolution Strategy appears to be the fastest algorithm for our approach, and its results were close to the simulated annealing. That is why, the various results presented hereafter are mainly obtained through this algorithm. But we have first to design a cost function fitting our problem, which will be called at each optimization step.

2.4.4 Cost function

As the data directly usable in simulations are meshes, our evaluation function for the optimization task should be a distance function between two meshes. The most natural way to compare meshes consist in comparing each vertex and summing the error as can be seen in figure 2.13. This distance function allows to respect the form of each cell and it compares as well the global displacement of the structure. In practice, our distance function will then be the sum of the squared errors between each vertex, since taking the square allows to have a smooth function at the minimum 0, which is not the case for the absolute value for instance, and which can be viewed as a regularization. Moreover, it allows to detect minimum with better accuracy than with an absolute value, since the gap between two function evaluations is higher, due to the absence of squared root, which flatten the error curves.

But as we are currently working in pixels, an approximation of the mesh of one pixel per vertex is an admissible error that is not significant. That means that if we move each vertex by one pixel, the sum of errors made by this approximation should lead to the same results as will be discussed in section 2.5.5.

For now, as we have around 90 vertices in each mesh, we can roughly compute this non-significant error. Indeed, the farthest pixel that is incident to one pixel of our structure is the one in the diagonal. By choosing such an approximation of our vertex, the squared error is 2 per vertex : the diagonal of a square of length 1. If we do this for each vertex of the first mesh and of the second mesh, the admissible error between the two meshes is then of around :

$$\Delta e = 2.\text{ Number of Vertices } .2 \approx 370$$

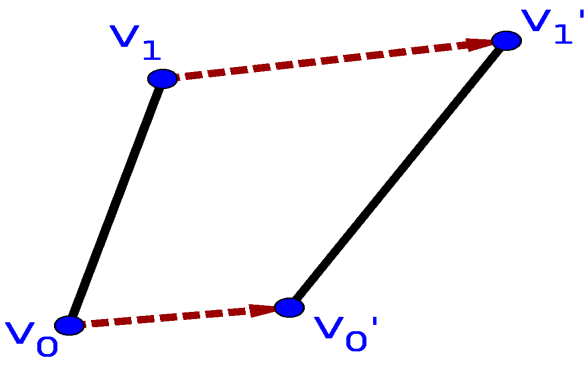

FIGURE 2.13 – *Cost function comparing each vertex displacement and summing the error*

We have also tried a cost function, consisting in minimizing the difference between the length of the walls reached by the simulation and the desired ones given by the image, which could allow more tolerance in the simulated image and was not as restrictive as the first cost function we tried. Indeed it allows, for instance, global rotation of the mesh. It may thus be viewed as a smoothing of the first cost function.

But this smoothing, as it allowed more flexibility in the simulated mesh, lead to more ill posed problems.

Finally, we also tried a cost function independent of the mesh refinement as can be seen in figure 2.14. Distance between edges of the first mesh given by the simulation and the mesh originated from the deformed image is computed. This distance is the area between both edges. Considering a refinement of the mesh with a point on the first edge (V_α, which is transformed in V'_α in the second mesh), the area computed is the same with this new point as can be seen in figure 2.14. This allow for a cost function independent of the mesh refinement.

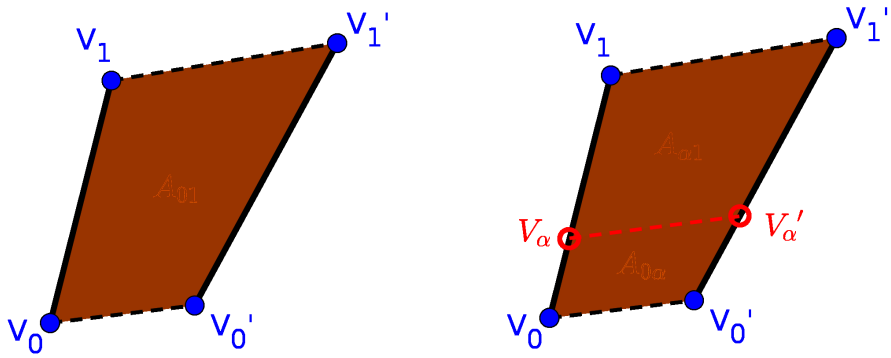

FIGURE 2.14 – *Cost function comparing area from displacement, which is independent of the mesh refinement*

With this choice of cost function, we find the same results as with the first cost function described : when the problem is well-posed, it is well posed for both cost function and the stiffness of cell wall arising from optimization is the same. When the problem is ill-posed, it is ill-posed for both cost function, and no precise value arises from optimization.

However, the value of the error is much more important with this last version of distance function, independent of the mesh refinement, since it compares area, not only distances. That is why it seems easier to reach a minimum with the first cost function described, as the valley containing this minimum is narrower in this case, and the optimization algorithms much more rapid. That is why the results presented hereafter originate from the first distance function described.

The results using such a cost function showed that the problem was still ill-posed with so many parameters (elasticity of cell wall, inner pressure and bending). So a first step was to reduce their number. Afterwards, we will present the results of optimization with our cost function.

2.5 RESULTS FOR HYPOCOTYLS

2.5.1 Statistical tests

Firstly, as in our model, each type of cell wall, i.e. for each layer (L1, L2, L3, etc) and each type of wall within these layers (periclinal or anticlinal), may be modeled with different stiffness and thus elasticity, modeling the interior of the plant organs leads to multiple parameters (here, multiple stiffness). We separate the walls by categories defined according to topological distance to the surface : surface cell walls, anticlinal of L1 cell walls, periclinal of L1 cell walls, etc... So to reduce this number one could observed the different behavior of these walls, through the deformation observed.

To deduce which type of walls were relevant to separate with respect to an elastic model, we observed the deflated cells with respect to the inflated ones. Observing in such a deformation the change of length of different types of cell walls allow us to separate different kind of wall behavior.

Observing the deformation of around 90 different images segmented from around 40 different hypocotyls for such a deformation, the length variation of each type of wall did not seem to follow a Gaussian law. Visually, we could not really recognize the well identified shape of Gaussian data, nor a Shapiro test did indicate that our data seemed to follow such a law (p-value for Shapiro test usually really low for each type of walls : less than 5%).

Therefore, we decided to use a Wilcoxon test, which is quite robust, for variables following non Gaussian law. The p-value of such a test tended to indicate that three different type of wall need to be separated :

1. surface walls,
2. anticlinal wall of L1,
3. all the internal walls.

Indeed, the p-value of the correlation between the surface walls and any other type of walls as well as the one between anticlinal wall of L1 and any other type of walls was really low (less than 5%, and often less than 1%), which seems to indicate a poor correlation between these types of walls and the other types. Whereas, for internal walls, the p-value of the same test was more than 70%, which tends to indicate a high correlation between these types of walls.

So, an obvious simplification for our model was to distinguish only three types of cell walls : the outer cell walls, the anticlinal of the L1 cell walls and all the other inner cell walls.

2.5.2 Geometrical results

By differentiating the three types of wall described in the previous section, we observed that they behave differently when plasmolysed (when deflated). Indeed, Figure 2.15 represents the ratio between each type of wall in inflated state and plasmolysed state (without pressure) versus the average plasmolysis ratio. This ratio is obtained by the following formula :

$$r = \frac{l}{l_0} \tag{2.14}$$

where l stands for the length of the wall considered in inflated state, and l_0 the corresponding one in deflated state.

In this figure, the anticlinal wall of the L1 (in red) seems to be almost rigid as they almost don't inflate, whereas the surface walls (in blue) tends to inflate more. Finally the inner walls (in green) tend to move more than the two first type of walls.

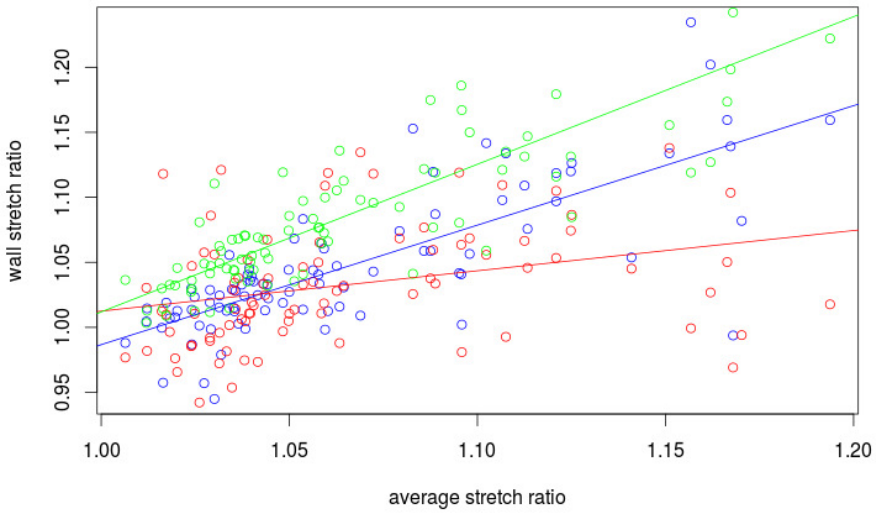

FIGURE 2.15 – *Hypocotyl : wall stretch ratio for different types of wall. Blue : surface, red : anticlinal of L1, green : inner cell wall*

Fitting the wall stretching with a linear model seems to be adequate, since the residual standard error is the same as with a quadratic model as can be seen in figure 2.16. With both models, one can defined the residual :

$$\widehat{\varepsilon}_i = X_i - \overline{X}$$

which is the difference between the observed value X_i and the predicted one $\overline{X}$. The standard error of the residual measures the adequacy of the prediction of the model to the observations. In our case, this residual is of the order of 3% in each case, which is less than the variation of each type of cell wall and shows therefore a relatively good agreement between this kind of model and the data we are using.

Computing the mean value for each type of cell wall (surface, anticlinal of L1 and internal) also shows that anticlinal wall of L1 almost don't move as the surface cell walls. Whereas

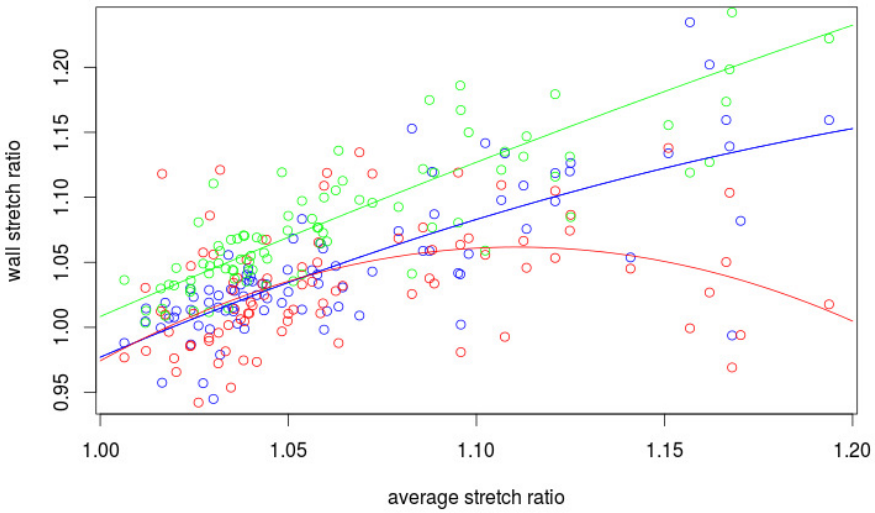

FIGURE 2.16 – *Hypocotyl : wall stretch ratio for different types of wall fitted by quadratic polynomial. Blue : surface, red : anticlinal of L1, green : inner cell wall*

internal cell walls deform much more as can be seen Figure 2.17, where the error bar stands for the standard error of the mean (SEM), which is the standard deviation (σ) divided by the square root of the number of samples :

$$SEM = \frac{\sigma}{\sqrt{n}} \tag{2.15}$$

This error allows tailing apart significant differences in the mean. And in figure 2.17, we can see that the mean comportment of the internal cell wall may be different from the two other types. This will be confirmed by optimization results in section 2.5.4.

2.5.3 Reducing the parameters

The problem of finding the mechanical characteristics of plant cells through the modeling adopted is an homogeneous problem of degree 0. That means that we can only deduce ratios between different mechanical parameters, but not the absolute value.

In fact, this type of problem is the same as two springs in series, compressed by two walls. Observing the length variation of the springs, only gives access to the ratio of stiffness between these two springs, through the equations of mechanics. As can be seen Figure 2.18, compressing two springs in series give rise to the following equation :

$$f = k_0(l'_0 - l_0) - k_1(l'_1 - l_1)$$

with f the force acting at the junction between the two springs, k_0 and k_1 the respecting stiffness of the red and green springs. Here, at a static equilibrium, this force is null. And as we only know the various displacements, we have only access to the ratio of stiffness through the formula :

$$\frac{k_1}{k_0} = \frac{l'_0 - l_0}{l'_1 - l_1}$$

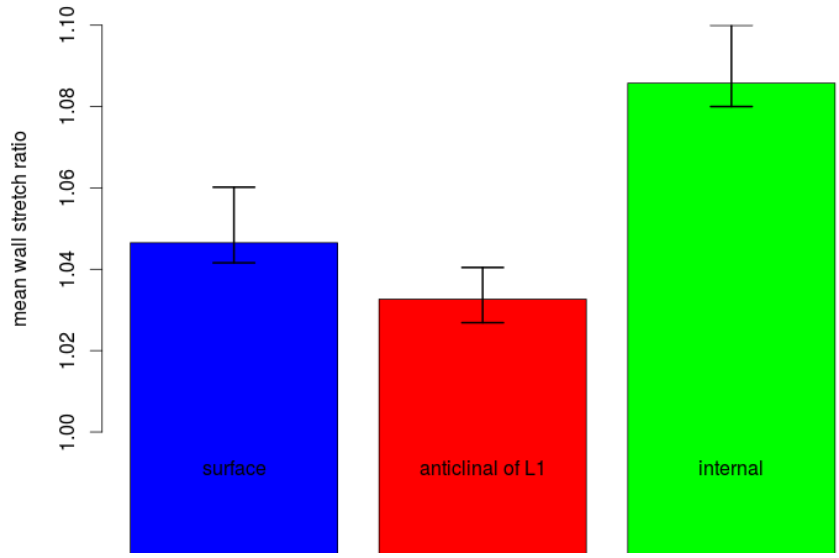

FIGURE 2.17 – *Hypocotyl : mean wall stretch ratio for different types of wall. Blue : surface, red : anticlinal of L1, green : inner cell wall*

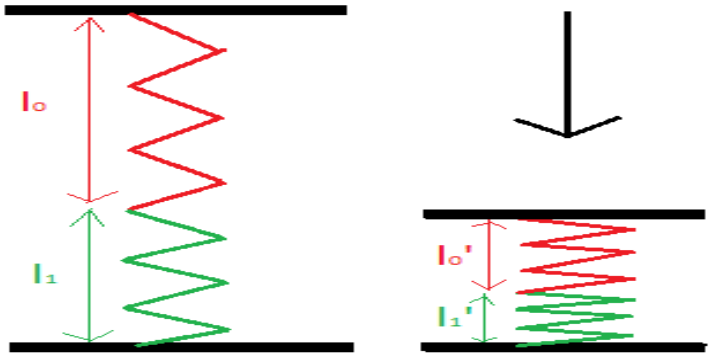

FIGURE 2.18 – *Principle of the method : observation of 2 springs in series undergoing a known displacement yields stiffness ratios*

With the formulation we use in our optimization loop, we face the same type of problem with pressure. In fact plotting the error function for the surface wall stiffness and the interior stiffness with the pressure and the stiffness of the anticlinal walls fixed shows that if we multiply the pressure by a given number, the error function has the same shape but with stiffness multiplied by the same number as can be seen Figure 2.19

As only the ratio between the different parameters can be accessed through this technique, we typically always input the pressure as fixed, and deduce the ratios between stiffnesses and pressure, through optimization.

First results were obtained with deflation experiments. To correlate with these types of experiments, we use the deflated mesh as original mesh. Taking the pressure as input allows to retrieve the inflated mesh through the simulation. So we are doing the opposite way as in expe-

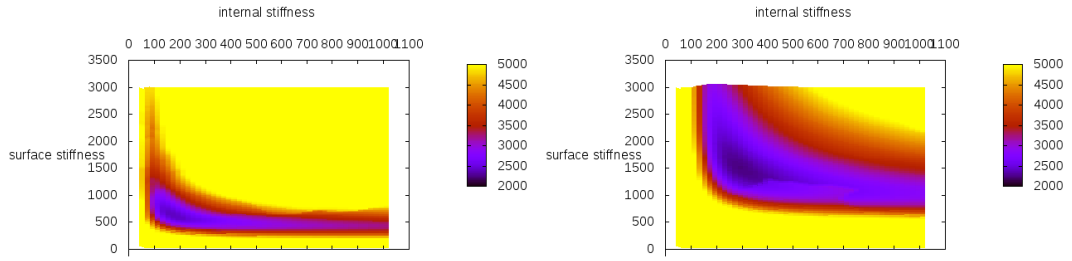

(a) Cost function for surface and internal stiffness with anticlinal of L1 stiffness fixed and pressure = 0.5

(b) Cost function for surface and internal stiffness with anticlinal of L1 stiffness fixed and pressure = 1

FIGURE 2.19 – *Cost function for the optimization problem which is homogeneous of degree 0 : multiplying the pressure by* 2 *scales the error by* 2

riments, but as our system is reversible, the same results should be obtained both ways.

However first results showed that our minimization problem was ill posed : for the same images, we retrieve the same deformation fields with totally different parameters. Even worse : starting with relatively similar mechanical parameters, the optimization process gave us really different results, with determinist as well as stochastic algorithms.

That meant that we had too many parameters in our model, and thus, that different mechanical characteristics had the same impact on the result of a simulation. The obvious unnecessary parameters for our simulation were the bending springs that added a stiffness, which was redundant with the elasticity of cell walls and pressure. In fact, minimizing the same problems without the bending stiffness gave us approximately the same error, or at least a difference in the error that was not significant, but with much less parameters. On the contrary, pressure and elasticity are obvious necessary parameters in order to retrieve the right deformation field from experimental images. Pressure is necessary since it makes the structure inflates. Without pressure, our system is at equilibrium in its rest state and does not move. Elasticity is necessary since the inverse problem could in practice not be solved so accurately without this parameter.

That is why the only parameters left in our model were the stiffness of the cell walls and the inner cell pressure as can be seen Figure 2.20.

The results are much easiest to interpret with this simplified model, as fewer parameters need to be analyzed. Moreover, cell wall stretching and internal turgor pressure refer to well-known mechanical characteristics.

This model with, as physical parameters, the stretching of the cell walls and the inner cell pressure, leads to well posed problems, or to ill posed problem with only one degenerated direction. This degenerated direction is often the surface stiffness or the anticlinal of L1 stiffness, which tend to be really stiff. In this case, when the problem is not well posed, we can explore the stiffness in two dimensions : the surface stiffness as well as the internal stiffness are explored for instance, for a given value of anticlinal stiffness as in figure 2.21. Plotting the resulting cost function shows that the internal cell wall stiffness is always well defined, but that the surface cells stiffness, as well as the anticlinal of the L1 stiffness, often tend to take high values.

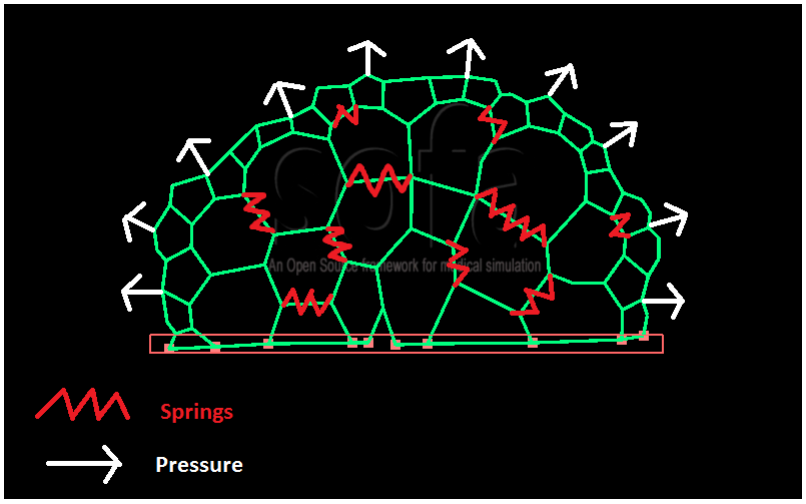

FIGURE 2.20 – *modelling a 2D cut of a hypocotyl from a mechanical point of view*

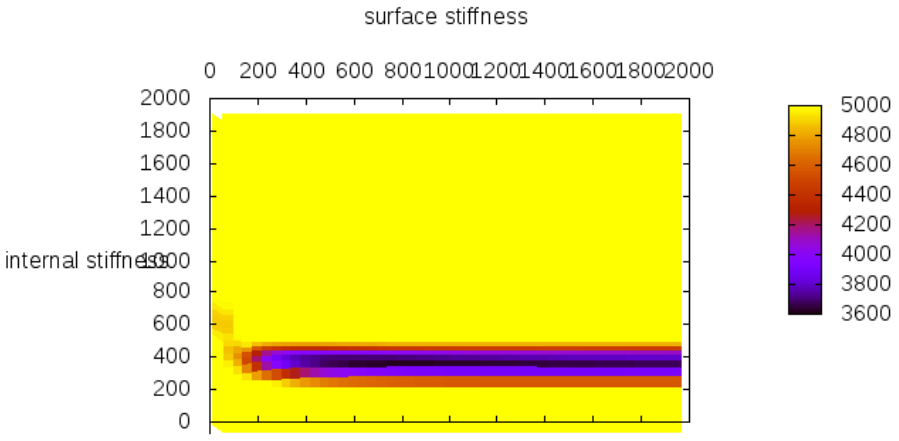

FIGURE 2.21 – *Example of value of the cost function, with a given value of anticlinal wall of L1 stiffness, shows that the problem is ill-posed in the direction of the surface stiffness*

Surface wall and anticlinal wall of L1 tend to be really stiff compared to the internal cell wall, which is in good agreement with the geometrical results of Section 2.5.2.

2.5.4 Optimization results

Figure 2.22 shows that the stiffness of the surface walls as well as the anticlinal walls of L1 are almost similar, or at least can't be distinguished with such an optimization process. Whereas the inner cell stiffness seems to be much lower than the two former. On this figure, the error bars stand for the standard error of the mean, which is the standard deviation divided

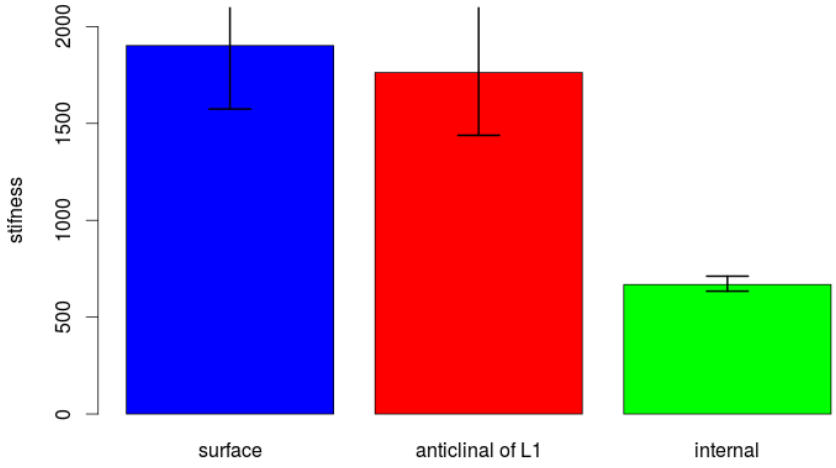

FIGURE 2.22 – *Ratio of stiffness to pressure of hypocotyl for different types of walls. Blue : surface, red : anticlinal of L1, green : internal*

by the square root of the number of samples used. This error allows to deduce that the mean stiffness of the two first type of wall may be statistically different than the mean of the inner cell stiffness, by around a factor 3 at least.

These results were obtained from deflated state to inflated state. However, other types of global tissue experiments involve compression of hypocotyls. Are the results coherent with compression ? And what are the limits of our model when looking at other types of experiments ?

In fact, compressing the hypocotyls gave us the same type of stiffness results : the internal cell wall elasticity is well defined and the mean obtained with optimization on compression is the same as the one obtained in deflation experiments. The inverse problem on compression seems also to be degenerated in the surface and anticlinal of L1 directions, as the stiffness values in these directions tend to be much higher and no global minimum of the cost function may be found in these directions.

However, replacing the surface and and anticlinal of L1 stiffness by the mean obtained with plasmolysis experiments gave us the same results as with the optimization process : our cost function is as good with these values as with optimization. That may indicate that the model fits also with this type of experiment, and that plasmolysis may be enough to deduce stiffnesses, or at least ratios of stiffnesses, since with other types of global deformation experiments, like compression, the results are in good agreement with the plasmolysis results.

2.5.5 Robustness of the model

Moving the vertices of our mesh through a random number of one pixel gives the same results in term of optimization, which means that we are robust enough and may admit one pixel of error per vertex.

2.5.6 Oryzalin treatment

Mechanical properties of the walls depend on the oriented deposition of the cellulose microfibrils, which is directly correlated to the positions of microtubules attached to the inner side of the plasma membrane as stated by [Corson et al., 2009].

Orizalin acts through the disruption (depolymerization) of microtubules, thus blocking anisotropic growth of plant cells, and finally changing the cell wall properties. The results with oryzalin treatment are different than in normal conditions. As stated Figure 2.23, geometrical results shows that the depolymerization of the cell wall leads to softer anticlinal walls of the L1. All internal cell wall seems to move accordingly and have, thus the same wall stretched ratio, according to equation 2.14. Again on this figure the error bars stand for the standard error of the mean according to equation 2.15. Whereas the surface walls seems to be reinforced. They may compensate the relative softness of internal tissue and contain the internal pressure, since the resistance of the cell wall to the internal turgor pressure is the main factor influencing the shape of the organ ([Niklas, 1992]).

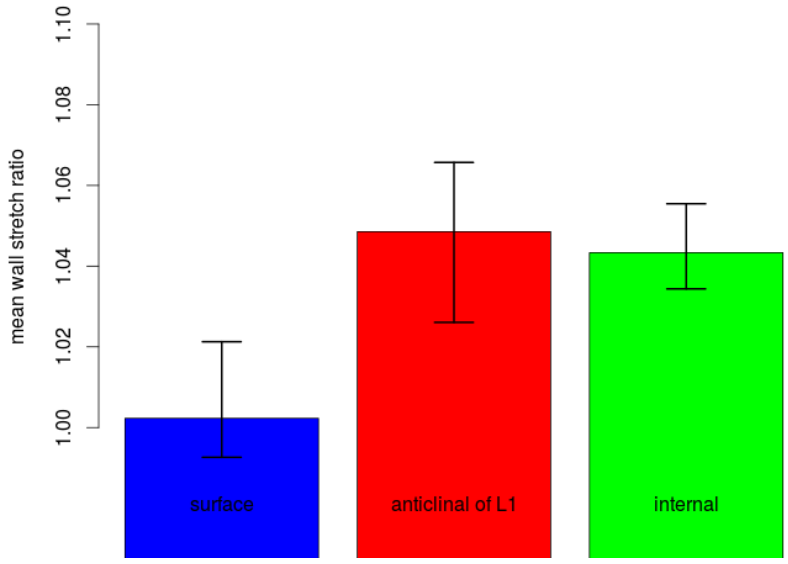

FIGURE 2.23 – *Wall stretch ratio with oryzalin treatment for different types of cell walls. Blue : surface, red : anticlinal of L1, green : internal*

These geometrical results are well correlated by the optimization results. Figure 2.24 shows that the cell wall stiffness of internal cell walls is the same as stiffness of anticlinal walls of L1. Thus all inner cell wall seem to have the same stiffness. Whereas the surface cell walls are much stiffer by a factor at least three.

2.5.7 Pressure variation on L1

Figure 2.25 shows that changing the pressure in L1 only, yields changes in surface stiffness (blue dots in figure 2.25), while the internal stiffness does not seem to change (green dots in the same figure). The optimization problem underlying such results is ill-posed for anticlinal stiffness of L1. That is why we did not represent these types of walls, which would be randomly distributed around 1.

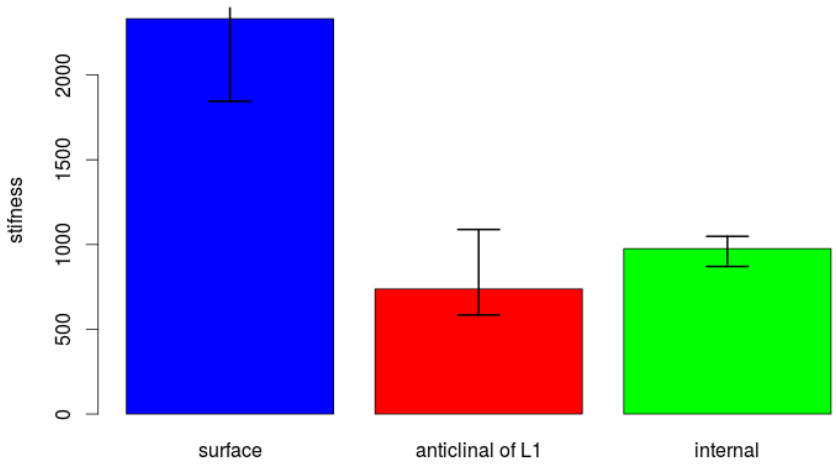

FIGURE 2.24 – *Ratio of stiffness to pressure with oryzalin treatment for different types of cell walls. Blue : surface, red : anticlinal of L1, green : internal*

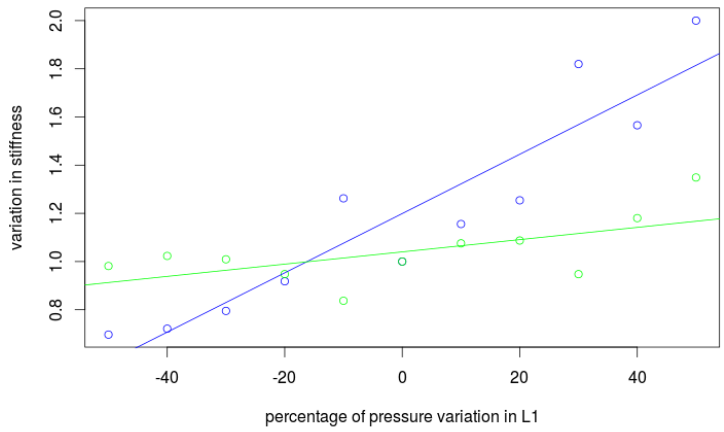

FIGURE 2.25 – *Pressure variation on L1 impacts stiffness of surface in blue, while internal stiffness in green does not seem to change*

Figure 2.25 shows that even with an increase or decrease of 50% in pressure in the L1, the stiffness variation is under a factor 2. Our deduction of relative stiffness between external and internal layers may still be valid since surface and anticlinal of L1 stiffnesses are found to be around 3 times higher than internal stiffness (see section 2.5.4).

2.5.8 Limits of elastic model

From plasmolysed or compressed state, coming back to normal conditions, a perfect elastic structure should retrieve its original position. If we compare the mean wall stretch ratio following equation 2.14, we should find a ratio of 1 for each type of cell wall.

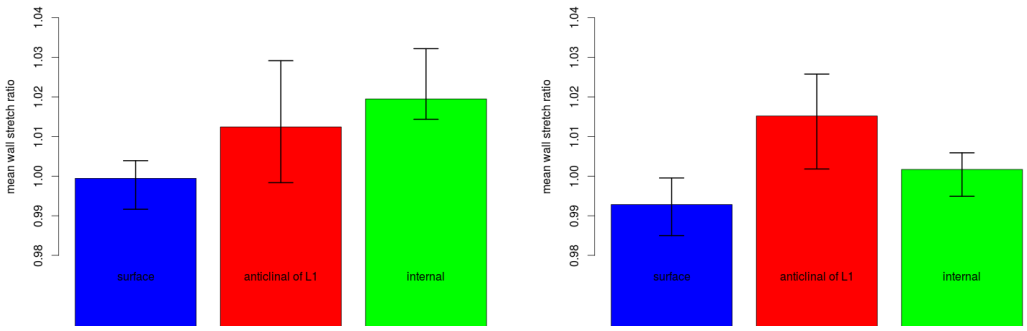

(a) wall stretch ratio for hypocotyls from plasmolysed condition and back to normal state

(b) wall stretch ratio for hypocotyls from compressed condition and back to normal state

FIGURE 2.26 – *Mean wall stretch ratio back to normal state. Blue : surface, red : anticlinal of L1, green : internal*

Figure 2.26 shows that when the deformation is not up to 4%, we are almost back to normal, with a ratio near 1. But, when this deformation is up 4%, the structure does not exactly came back to its rest state. However, in any cases, this mean wall stretch ratio is under 2% and often under 1%, which may indicate a relatively good agreement between the elastic model and the hypocotyl structure.

2.6 RESULTS FOR ROOTS

2.6.1 Statistical tests

Testing the behavior of each type of cell walls as in the case of the hypocotyl, from inflated to deflated state, we are first interested in the shape of the distribution of wall stretch ratio. Does it seem to follow a Gaussian law ? Indeed, like for hypocotyls, the p-value of a shapiro test for the surface and anticlinal of L1 wall was really low (under 5%), whereas the same p-value for all the internal cell wall was much higher (higher than 20% for each type of internal cell walls). The internal cell wall may follow a Gaussian law according to this test, but it seems unlikely that the other types of wall follow such a law.

That is why we used a wilcoxon test to separate the different cell wall behavior. For the roots, results were not as clear as for the hypocotyl. Whereas all the internal cell wall that are not the anticlinal of L1 cell wall seems to behave identically (p-value of wilcoxom test over 40%), it seems much harder to tail apart the other types of wall. Surface walls and anticlinal of L1 walls are in good correlation (p-value around 20%) like anticlinal walls of L1 and internal cell walls (p-value around 40%), but surface cell walls and internal walls may behave really differently (p-value under 1%).

This is correlated when looking at the means of stretch ratio of each of these types of walls as stated Figure 2.27. A smooth transition appears between the means of the surface walls to the mean stretch ratio of internal cell wall through the anticlinal of L1 mean stretch ratio.

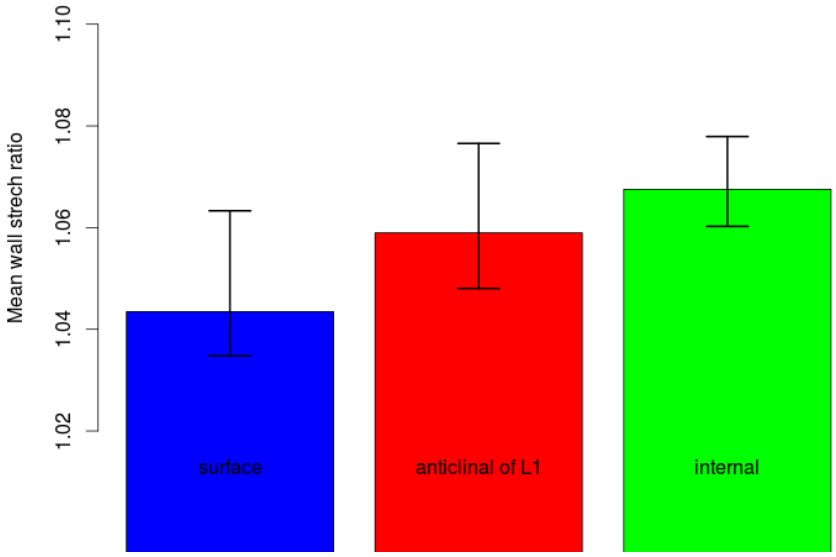

FIGURE 2.27 – *Mean wall stretch ratio of roots for different types of wall. blue : surface, red : anticlinal of L1, green : inner cell wall*

Therefore, it seems harder to separate the different behavior of each type of cell wall. Nonetheless, the surface cell walls as well as the internal cell walls seems not correlated. And the transition between them may be due to the anticlinal of L1 cell walls. That is why we choose to separate, as in the case of the hypocotyl the same types of walls : surface, anticlinal of L1 and internal.

2.6.2 Geometrical results

Differentiating these three types of wall, the analyze of their behavior from deflated state to inflated state can be achieve by computing their ratio of stretching from the same formula as for the hypocotyl (see Equation 2.14). This corresponds to Figure 2.28 where it seems harder than for hypocotyls to deduce different behavior, although anticlinal of L1 cell wall seems to be not as sensitive as other types of wall to inflation and deflation, since the corresponding red curve is more horizontal than the two other (blue for the surface and green for the internal walls).

2.6.3 Optimization results

As was the case for the hypocotyl, the optimization problem from deflated state to inflated state is often ill-posed in the direction of the surface and anticlinal of L1 walls. On the contrary, the internal cell wall stiffness is well defined. Representing the mean values of stiffnesses with, as error bar, the standard error of the mean, shows that, the ratio between pressure and internal stiffness is almost the same as for the hypocotyl. The anticlinal of L1 stiffness being also much stiffer than internal walls by a factor around 3. While the surface walls seems still stiffer than these latter (see Figure 2.29).

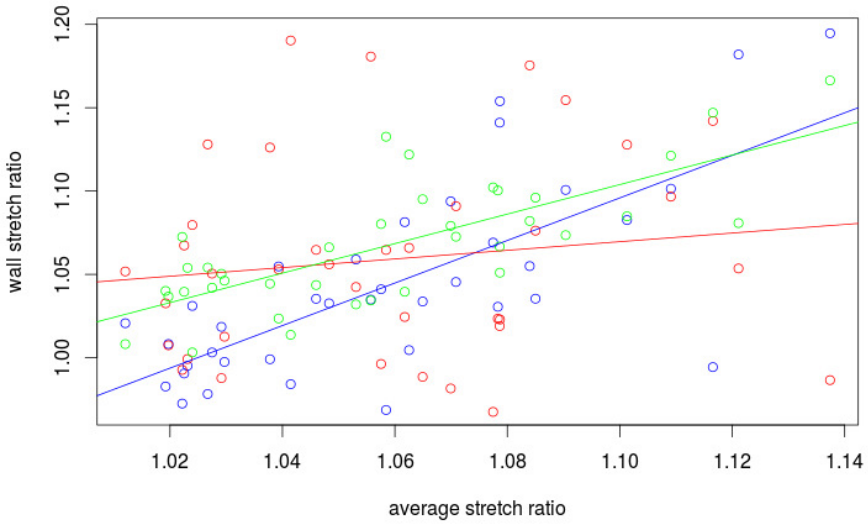

FIGURE 2.28 – *Plasmolysis ratio of roots for different types of wall. blue : surface, red : anticlinal of L1, green : inner cell wall*

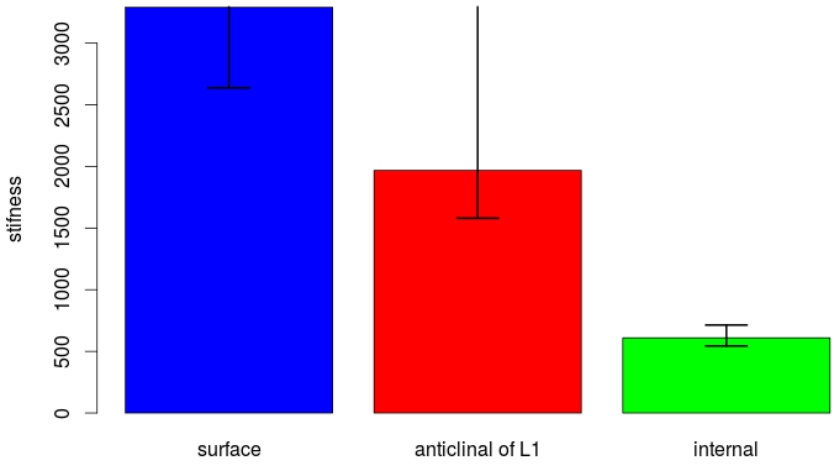

FIGURE 2.29 – *Ratio of stiffness to pressure for roots for the different types of walls. Blue : surface, red : anticlinal of L1, green : internal*

Finally, we will try to adapt the same methodology to the meristem.

2.7 RESULTS FOR MERISTEM

2.7.1 Statistical tests and geometrical results

The structure of the meristem is quite different than the structure of roots or embryonic stems. Its shape is not as elongated as the hypocotyl, and it is composed of several layers : up to 6 in some cases as can be seen in figure 2.30.

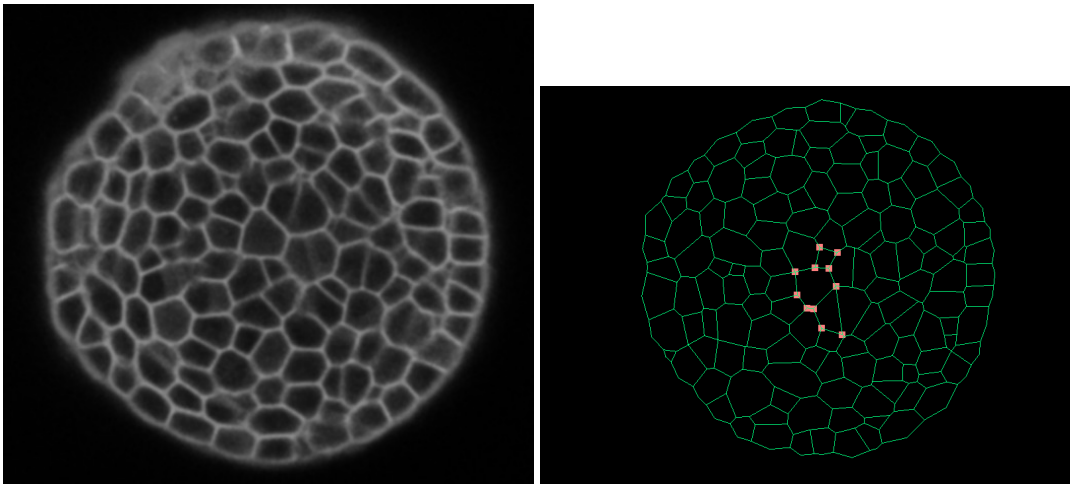

(a) Image of a cut of a meristem

(b) Mesh of a cut of a meristem, most internal layer vertices are red

FIGURE 2.30 – *Meristem in 2D from image to mesh*

As in the case of hypocotyl and roots, we have tested our data and the behavior of each type of cell walls within each layer following Equation 2.14. Like for hypocotyls and roots, there seems to be three different types of cell wall behavior : the surface cell wall, the anticlinal of L1 cell wall and the internal cell walls. This is correlated by the mean wall stretch ratio of each type of cell walls by layer, and can be seen Figure 2.31. This figure shows that the meristem cell walls move less than hypocotyls and roots cell walls. That is why the optimization process described in figure 2.2 could not work in the case of the meristem : the inverse problem arising seems to be ill-posed and no stiffness can be retrieves, since the cell walls undergoes too small deformations.

However, through Figure 2.31, significant differences may be observed in the behavior of surface, anticlinal of L1 and internal cell walls.

In figure 2.31, we can also observe that the anticlinal of L1 cell wall mean stretch ratio is slightly under 1. When the structure inflates under pressure, these walls are retracting, which seems counter-intuitive.

To study this effect, we have developed a simplified theoretical model as can be seen in figure 2.32.

2.7.2 Simplified model for meristem

This simplified model consist in considering all internal layer as a spring with an equivalent stiffness K_i. Such approximation may be found in the work of [Gibson and Ashby, 2001] for honeycombs under biaxial loading. The structure in this case reacts as an elastic structure with an apparent Young modulus depending on the thickness, the length and the Young modulus of

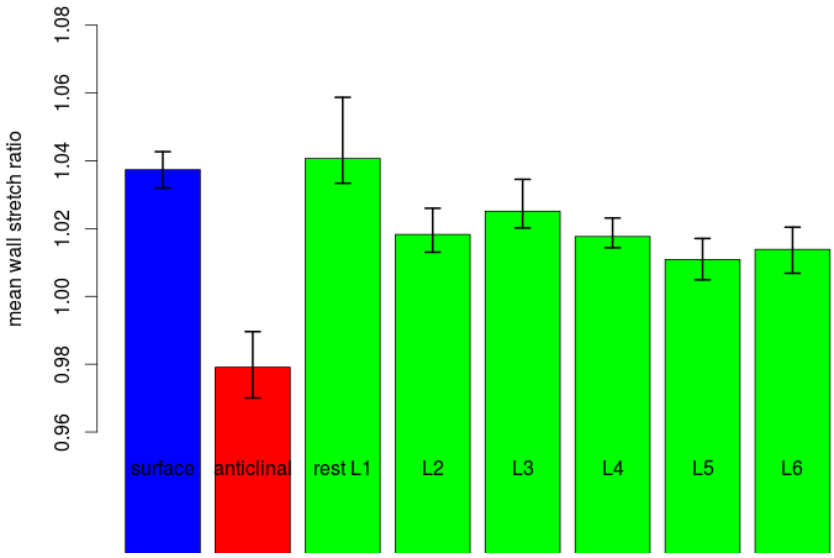

FIGURE 2.31 – *Mean wall stretch ratio of meristem for different types of wall. blue : surface, red : anticlinal of L1, green : inner cell wall*

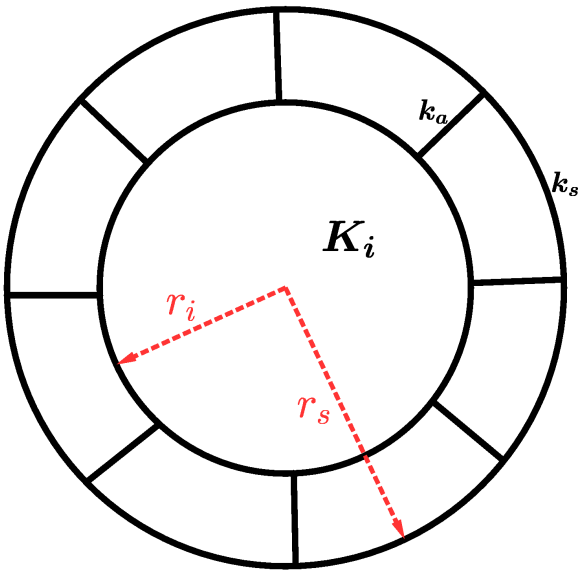

FIGURE 2.32 – *Simplified model of meristem with all internal wall reacting as a spring and L1 cells as concentric*

the cell walls. Here such an approximation may still be valid with a dependence on the structure also. The L1 is modeled with concentric cells with anticlinal walls of L1 as springs and surface walls as curved springs.

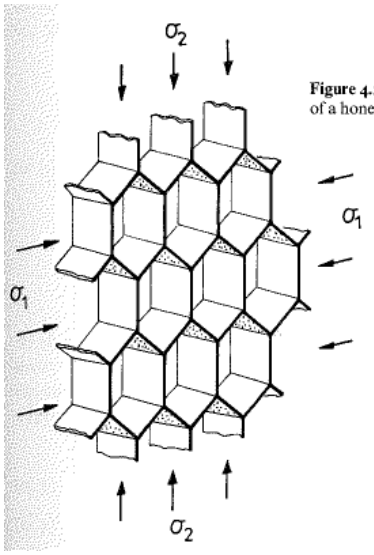

Figure 4.26 Biaxial loading of a honeycomb.

FIGURE 2.33 – *Internal part of simplified model reacts as honeycombs under uniform loading and may be modeled with a elastic continuous material (source [Gibson and Ashby, 2001])*

The energy of such a system is given by :

$$\varepsilon = \frac{1}{2}\frac{K_i}{r_i^0}(r_i - r_i^0)^2 + \frac{1}{2}n\frac{k_a}{r_s^0 - r_i^0}[(r_s - r_i) - (r_s^0 - r_i^0)]^2 + \frac{1}{2}n\frac{k_s n}{2\pi r_s^0}(\frac{2\pi}{n}r_s - \frac{2\pi}{n}r_s^0)^2 - \pi P_i r_i^2 - \pi P_e(r_s^2 - r_i^2) \tag{2.16}$$

with K_i, k_a and k_s, respectively the internal, anticlinal of L1 and surface stiffness, r_s and r_i the external and internal radius, P_i and P_e the pressure in the internal layers and in the L1 respectively, and n the number of L1 cells.

When the structure is at equilibrium, the derivative of the energy with respect to the observable should be null, which is equivalent to :

$$\begin{array}{rcl} \frac{\partial \varepsilon}{\partial r_s} & = & 0 \\ \frac{\partial \varepsilon}{\partial r_i} & = & 0 \end{array} \tag{2.17}$$

which can be rewritten as :

$$\begin{array}{rcl} n\frac{k_a}{r_s^0 - r_i^0}[(r_s - r_i) - (r_s^0 - r_i^0)] + \frac{k_s 2\pi}{r_s^0}(r_s - r_s^0) - 2\pi P_e r_s & = & 0 \\ \frac{K_i}{r_i^0}(r_i - r_i^0) - n\frac{k_a}{r_s^0 - r_i^0}[(r_s - r_i) - (r_s^0 - r_i^0)] + 2\pi(P_e - P_i)r_i & = & 0 \end{array} \tag{2.18}$$

But as we have 3 parameters in our model (K_i, k_a and k_s) and only two equations, we need one more assumption to deduce the parameters from the equilibrium configuration. Here different hypothesis may arise.

Rigid anticlinal walls

Since the anticlinal wall of L1 seems almost rigid, we can make the hypothesis that they are effectively rigid. Then the energy of the structure should not contain the term containing the anticlinal of L1 stiffness, and Equation 2.18 becomes :

$$\begin{array}{rcl} \frac{2k_s\pi}{r_s^0}(r_s - r_s^0) - 2\pi P_e r_s & = & 0 \\ \frac{K_i}{r_i^0}(r_i - r_i^0) + 2\pi(P_e - P_i)r_i & = & 0 \end{array} \tag{2.19}$$

Solving for r_s and r_i, Equation 2.19 yields :

$$\begin{array}{rcl} r_s & = & \frac{2k_s\pi r_s^0}{k_s\pi - 2\pi P_e r_s^0} \\ r_i & = & \frac{K_i r_i^0}{K_i + 2\pi(P_e - P_i)r_i^0} \end{array} \tag{2.20}$$

But remind that $r_s - r_i$ is constant. So there is a link between the two parameters left k_s and K_i. We can't through the observable deduce the free parameters in this case.

Rigid surface walls

An other interesting hypothesis consists in considering the surface as extremely rigid. Under this hypothesis, the term containing the surface stiffness in equation 2.16 vanishes, $r_s = r_s^0$, and Equation 2.18 yields :

$$\begin{array}{rcl} n\frac{k_a}{r_s^0 - r_i^0}[(r_s^0 - r_i) - (r_s^0 - r_i^0)] - 2\pi P_e r_s^0 & = & 0 \\ \frac{K_i}{r_i^0}(r_i - r_i^0) - n\frac{k_a}{r_s^0 - r_i^0}[(r_s^0 - r_i) - (r_s^0 - r_i^0)] + 2\pi(P_e - P_i)r_i & = & 0 \end{array} \tag{2.21}$$

Solving again for r_s and r_i, this equation yields :

$$\begin{array}{rcl} r_s & = & r_s^0 \\ r_i & = & \frac{\frac{K_i}{r_i^0} + \frac{nk_a}{r_s^0 - r_i^0}}{\frac{K_i}{r_i^0} + \frac{nk_a}{r_s^0 - r_i^0} + 2\pi(Pe - P_i)} r_i^0 \end{array} \tag{2.22}$$

Here again, we can find a relation between both parameters left : K_i and k_a. So we can't deduce both parameters under this hypothesis. But the interesting properties of this hypothesis is that we may view the bottom row of Equation2.22 as :

$$r_i = \frac{K_{eq}}{K_{eq} + 2\pi(P_e - P_i)} r_i^0$$

with K_{eq} corresponding to the equivalent stiffness of 2 springs in series corresponding to the interior and the anticlinal wall of the L1. If $P_e > P_i$, then we can observe that the interior will expand under pressure, while the anticlinal wall will retract, since the outer layer is not moving. The results we obtain on meristem through the mean wall stretch ratio shown in figure 2.31 and which tend to indicate that the anticlinal walls of L1 retract when the structure inflates may be due to approximation in the mesh. But they also may be explained by a difference in pressure in internal layer and L1 and a really stiff surface cell wall as described by this simplified model. But the equation in the case of an homogeneous pressure may also be of interest.

General case with uniform pressure

Considering that the pressure is uniform : $P_i = P_e$, we can solve the system described by Equation 2.18 under the assumption of small deformation. This assumption yields, with a Taylor development around r_s^0 :

$$r_s^2 \approx r_s^{0\,2} + 2r_s^0(r_s - r_s^0)$$

The energy of pressure becomes : $-2\pi P r_s^0(r_s - r_s^0)$

And Equation 2.18 yields :

$$\frac{(r_s - r_i) - (r_s^0 - r_i^0)}{r_s^0 - r_i^0} = \frac{2\pi K_i P {r_s^0}^2}{2k_a k_s n\pi r_i^0 + K_i(k_a n r_s^0 + 2k_s\pi(r_s^0 - r_i^0))} \tag{2.23}$$

From Equation 2.23, we can deduce that if the pressure is homogeneous in the structure, the anticlinal wall of L1 can not retract according to an elastic model. Here the limit of a pure two dimensional elastic model arise, since it can not explain the behavior observed in the structure. More accurate modeling should take into account the third dimension or consider a non elastic material. That is currently what we propose in the next section : a simplified model taking into account the three dimensional geometry.

2.7.3 Simplified model with 3 layers

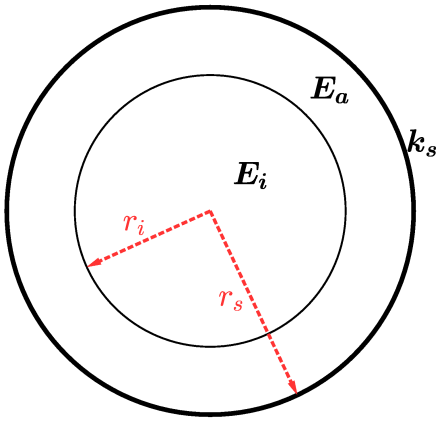

FIGURE 2.34 – *Simplified model with 3 layers : the surface as a thin shell, the L1 as a continuous medium and the inner part as a continuous medium*

Considering that the two dimensional previous model can't explain the retraction of the anticlinal wall of L1 when the meristem is subject to pressure, let us consider the 3D geometry. Taking into account the cell walls in the third direction can be viewed as the input of areal elements. Our new simplified model, as can be seen in figure 2.34 is composed of the surface considered as a thin shell, the L1 and the most inner part as continuous media with different stiffness.

Under plane stress assumption, $\sigma_{zz} = 0$ where σ_{zz} stands for the stress in the direction orthogonal to the plane considered. The displacement u is purely radial and $u = u_r$.

Under this condition the displacement in the L1 part takes the form as van be found in [Landau and Lifchitz, 1970] :

$$\begin{array}{rcl} u_a & = & ar + \frac{b}{r} \\ \epsilon_r & = & a - \frac{b}{r^2} \\ \epsilon_\theta & = & a + \frac{b}{r^2} \\ \sigma_r & = & \frac{E_a}{1-\nu_a^2}(\epsilon_r + \nu_a \epsilon_\theta) \end{array} \tag{2.24}$$

with a and b two constant, u_a is the displacement in the L1, ϵ_r, ϵ_θ are the strain in the radial and orthoradial direction, σ_r is the stress in the radial direction, and E_a and ν_a are the Young modulus and poisson ratio of the L1.

When considering the inner part with an homogeneous deformation, the equation of mechanics yield :

$$\begin{array}{rcl} \epsilon_i & = & \epsilon_\theta(r = r_i) \\ \sigma_i & = & \frac{E_i}{1-\nu_i} \\ u_i & = & \epsilon_i r_i \end{array} \tag{2.25}$$

with ϵ_i and σ_i the strain and stress in the internal part when $r = r_i$, u_i the displacement when $r = r_i$ and E_i and ν_i the Young modulus and poisson ratio in the internal layers.

Finally, as the surface is considered as a thin shell, the tension T in the surface can be expressed as :

$$T = k_s \epsilon_\theta(r = r_s) \tag{2.26}$$

with k_s the stiffness of the surface.

Solving Equations 2.24, 2.25 and 2.26 for a and b under the following boundary conditions :

$$\begin{array}{rcl} \sigma_i & = & \sigma_r(r = r_i) \\ P & = & \sigma_r(r = r_s) + \frac{T}{r_s} \end{array} \tag{2.27}$$

with P the internal pressure, yields some complex expression for a and b, depending on the other parameters : geometry (i.e. r_i and r_s) and material properties (i.e. Young moduli, poisson ratios and pressure). But the quantities we are interested in are :

$$\begin{array}{rcl} sa & = & \frac{u_a(r=r_s)-u_a(r=r_i)}{r_s-r_i} \\ ss & = & \epsilon_\theta(r = r_s) = \frac{u(r=r_s)}{r_s} \end{array}$$

sa and ss representing the ratio of displacement to the radius in the layer considered.

Under the assumption that $r_s - r_i << 1$, so that $r_s = r_m + \frac{h}{2}$ and $r_i = r_m - \frac{h}{2}$ one can expand the above expressions and find :

$$\begin{array}{rcl} sa & \approx & \frac{-Pr_m(E_i-\nu_a E_a-E_i\nu_a^2+E_a\nu_a\nu_i)}{E_a(k_s\nu_i-k_s-r_m E_i)} \\ ss & \approx & \frac{Pr_m(\nu_i-1)}{k_s+r_m E_i-k_s\nu_i} \end{array} \tag{2.28}$$

Considering that the L1 is retracting in the radial direction, when the structure inflates under pressure, sa should be negative. This appends when :

$$E_i(1 - \nu_a^2) < E_a\nu_a(1 - nu_i)$$

With no prior knowledge on the cell wall properties, a plausible assumption is that the cell wall are incompressible. Their poisson ratios are then approximately 0.5. Under the following condition :

$$\frac{E_a}{E_i} > 3$$

the anticlinal walls of the L1 may retract when the structure is inflating. An interesting point is that for hypocotyls and roots, this ratio of 3 is currently the minimum ratio found between both stiffnesses.

Going further, if we want to correlate the observations to this theory, we can analyze the ratio $\frac{ss}{sa}$ and compare to the values observed experimentally. Equation 2.28 yields :

$$\frac{ss}{sa} \approx \frac{E_a(\nu_i - 1)}{E_i - E_a\nu_a - E_i\nu_a^2 + E_a\nu_a\nu_i}$$

Experimentaly, we find that $\frac{ss}{sa} \approx -2.5$. Again, considering the material as incompressible, we have the following relation :

$$\frac{E_i}{E_a} \approx 7\%$$

With such a model, to match the experimental observations, the internal cell walls should be much softer than the anticlinal of L1 cell walls.

2.8 CONCLUSION

In this chapter, we have presented a methodology to extract ratios of mechanical parameters, i.e. stiffness, and pressure of complex biological structure, based on images of whole organs deformed. We have applied this methodology to hypocotyls, roots and meristems. The methodology developed in this chapter was based on the one hand on geometrical data from segmented images and on an optimization process on the other hand.

We have demonstrated that the information contained from the normal state to plasmolysed state is enough to deduce ratios of stiffness to pressure. From such experiments, both methods show coherent results : the more the geometry appears to move from normal state to plasmolysed state, the softer the corresponding cell wall. But as we have seen, the inverse problem arising is often ill-posed. However, we have been able to deduce ratios of stiffness to pressure for different kind of cell walls : surface, anticlinal of L1 and internal cell walls.

For hypocotyls and roots, the surface and anticlinal of L1 seems to be stiffer than the internal cell walls by a factor of at least 3, as showed by the optimization process. Surprisingly, measuring directly the variation of the geometry from normal state to deflated state, the anticlinal of L1 cell wall for the meristem seems to contract as the structure inflates, which could result from conditions linking pressure and stiffness, but that can not be retrieved with a two dimensional elastic model, as shown with a simplified model. However, considering the third dimension by modeling the meristem with areal elements, allows to retrieve this contraction when the structure inflates. This result arise from the continuum mechanics theory. More precisely, it is mainly due to the poisson ratio.

When experiments consist in deforming only a small part of the organ considered, such a method can not be applied, since the information contained in the deformation field should not be sufficient to retrieve mechanical properties. In this case, we can only develop a theoretical model to fit the experiments and verify assumption made by biologists. That is currently what we propose in the next chapter, with a simulated Atomic Force Microscope.

CHAPTER

3

LOCAL DEFORMATION MODEL OF PLANT CELLS

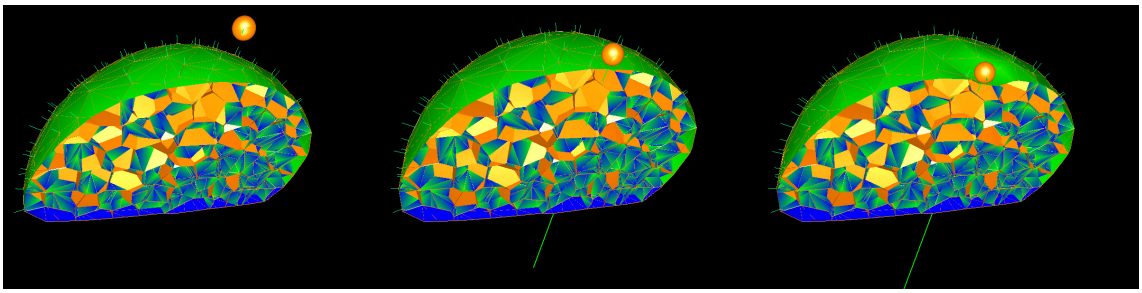

(a) (b) (c)

FIGURE 3.1 – *indentation of a three dimensional plant tissue with a probe acting like Atomic Force Microscopy*

This part has been done with A. Boudaoud and F. Faure.

Morphogenesis in a developing organism depends on the mechanics of the structural elements of the organism. In plants, typical experiments involve indenting tissues with a probe and measuring the force needed to reach a given depth. However, the heterogeneous structure and complex geometry of living tissues makes it a challenge to determine how such measurements are related to mechanical properties of the tissue, such as elastic moduli or internal pressure. Indeed, this task requires to perform a large number of direct mechanical simulations with a mesh representing the tissue. Here we propose a framework to achieve this task, using the Simulation Open Framework Architecture (SOFA) platform. We start from a realistic tissue structure corresponding to an early flower bud. We use a mesh where cells are polyhedral-shaped and are made of a liquid under pressure and where the faces separating two cells are thin elastic plates undergoing bending and stretching, and we model the interaction of this mesh with a spherical rigid probe. We obtain force versus depth curves that can be compared to experimental data. Thus our framework enables a comprehensive exploration of how mechanical parameters and probe position influence experimental outcomes, yielding a first step toward understanding the mechanical basis of morphogenesis.

3.1 INTRODUCTION

Understanding morphogenesis, i.e. how organisms achieve their final shape, is a scientific challenge that requires the input of many disciplines. Gene activity prescribes shape [Coen et al., 2004], but only indirectly since shape is determined by the mechanical elements of the organism [Mirabet et al., 2011]. Plants are well-suited to investigate morphogenesis because their mechanics is dominated by a single type of mechanical element, the cell wall [Niklas, 1992]. Accordingly it is essential to quantify the mechanics of cell walls, which, following experiments, depends on the parametrization of mechanical models of tissues interacting with probes [Milani et al., 2013, Routier-Kierzkowska and Smith, 2013]. However, available models address only simple geometries such as a single cell [Vella et al., 2012b] or a single cell layer [Kierzkowska et al., 2012]. Indeed full 3D models involve thousands of degrees of freedom, and the exploration of the parameter space requires a number of direct simulations that grows exponentially with the number of parameters, raising the issue of the trade-off between precision and speed of simulations. We believe that Computer Graphics simulation libraries

are well adapted for this, and we present an efficient computational framework to model the mechanics of three-dimensional plant tissues indented by a probe.

A plant tissue can be viewed as a tiling of a region of space by cells that are approximately polyhedral and have a size of a few micrometers. Each cell can be modeled as a liquid under pressure, which is in the range 0.1–1MPa [Niklas, 1992]. This pressure is contained by cell walls, which can be modeled as thin elastic plates (thickness 0.1–1μm) made of a polymeric material (elastic modulus in the range 1MPa–1GPa), and which lie at the faces of the polyhedra. Early mechanical measurements relied on macroscopic experiments that yield the (apparent) elastic modulus of a tissue at a macroscopic scale [Niklas, 1992].

In order to obtain mechanical properties at a cellular resolution, experiments have been scaled down [Geitmann, 2006, Routier-Kierzkowska and Smith, 2013, Milani et al., 2013], notably by using micro- or nano-indentation methods, wherein a micrometric or nanometric probe indents the surface of the tissue while force and displacement are measured. These indentation methods are named according to how displacements are controlled and forces are measured ; Cellular Force Microscopy [Kierzkowska et al., 2012] was designed for slightly larger displacement/forces than Atomic Force Microscopy (AFM), which is more suited to small scale / small force measurements [Peaucelle et al., 2011, Roduit et al., 2009, Milani et al., 2011, Fernandes et al., 2012, Radotic et al., 2012, Milani et al., 2014]. If the tissue were a continuous, homogeneous elastic body, it would have been straightforward to deduce elastic modulus from indentation experiments using standard contact mechanics [Johnson, 1987]. However, as plant tissue is heterogeneous and is full of liquid-filled cavities, experimentalists need to resort to (sometimes unverified) assumptions, for instance that the size of the probe enables the measurement of local (e.g. wall-level) or global (e.g. cell-level) properties of the tissue.

Analytical mechanical models were developed to go further, but they are limited to simple configurations, such as the indentation of inflated thin shells that are spherical [Vella et al., 2012b] or ellipsoidal [Vella et al., 2012a], or the indentation of a continuous elastic half-space with elastic modulus depending on the distance from its plane surface [Lee et al., 2008]. Moreover, it appears that the determination of the field of elastic moduli in a body from indentation experiments is ill-posed, unless additional assumptions are made, such as homogeneity [Johnson, 1987], simple gradation of properties [Lee et al., 2008] or existence of two types of materials [Roduit et al., 2009]. Therefore there is a strong need for realistic and efficient computational mechanical models than enable a comprehensive exploration of the parameter space. The more advanced studies addressed a single layer of plant cells with a sub-wall resolution [Kierzkowska et al., 2012], but such sub-wall resolution prevents a comprehensive investigation of the parameter space.

Unlike previous studies, we address here the indentation of realistic three-dimensional tissues. To do so, we use the Simulation Open Framework Architecture (SOFA) software, an open source library designed for physically based simulations in the field of medical simulation and computer graphics [Faure et al., 2012]. We illustrate our approach on the structure of the early floral meristem, which is a very young flower bud in the shape of a dome attached to the side of the shoot, and which consists of a few hundred cells in the plant Arabidopsis. The model accounts for the cellular structure of the floral meristem [Fernandez et al., 2010, Boudon et al., 2014], for cellular pressure, for the mechanics of the cell walls considered as thin elastic plates undergoing stretching and bending, and for the indentation by a spherical probe. We use the same tissue structure as in [Boudon et al., 2014], but instead of modeling tissue growth, we refine the mechanical model (e.g. by adding bending) and we consider the indentation of the tissue. In the following, we present the details of the structure and the model, a validation of the model, and then results that are discussed in the light of available experiments.

3.2 REALISTIC STRUCTURE OF MERISTEM

We reused a tissue structure obtained in [Boudon et al., 2014]. Briefly, this structure was derived as follows. A floral meristem (a young flower bud) from the plant Arabidopsis was imaged from confocal microscope and reconstructed in 3D in [Fernandez et al., 2010]. Then the 3D image was segmented in small volumes corresponding to cells [Fernandez et al., 2010]. Due to the noisy nature of the original images, such segmentation cannot be directly transformed directly in a mesh usable in a mechanical model. Therefore, a Voronoi tessellation of 3D space was constructed from the centers of mass of all cells : the faces of polyhedra are defined from all points that are equidistant to two centers of mass, as schematized in 2D in Figure 3.2. In addition this mesh was closed using the surface of the segmented floral meristem. Thus, [Boudon et al., 2014] obtained a 3D tessellation where each polyhedron corresponds to a cell from the original floral meristem.

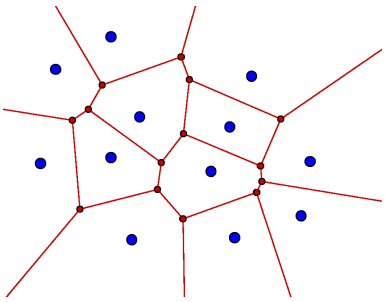

FIGURE 3.2 – *2D Voronoi tesselation*

We triangulated all faces to obtain our simulation mesh. In view of the trade-off between precision and speed of simulations, we chose to use a mesh with the minimal number of triangles, except near the point of impact of the indentor where the triangles were subdivided 16 times in order to improve precision where the model is most deformed. Overall, the mesh consists of 500 polyhedra (cells) with 3000 vertices, and more than 11000 triangles, each cell wall measuring between 5 to 10 units of length for a whole structure of around 80 units (see table 3.10). The radius of the spherical tip of the probe measures between $\frac{1}{15}$ of a cell size to half a cell size. Figure 3.3, shows the floral meristem imaged by confocal microscopy (left, [Fernandez et al., 2010]), the inside of the simulated structure (right), and its whole structure together with the simulated spherical AFM (bottom). The blue part is considered to be fixed since it is linked to the stem.

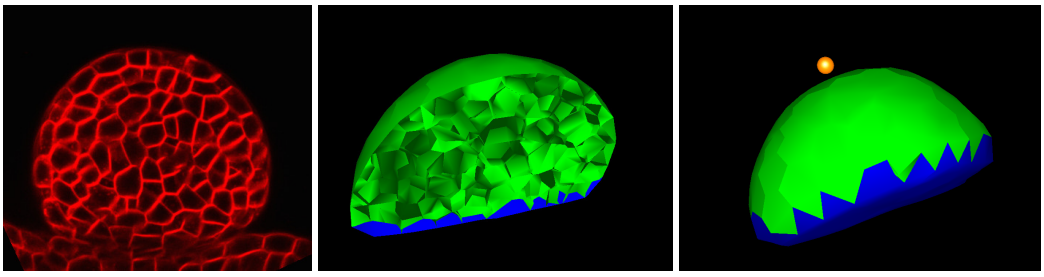

FIGURE 3.3 – *Realistic structure of a meristem : left view of a flower bud with cell contours marked in red ; mechanical structure generated ; simulation of a spherical probe indenting the structure*

3.3 MECHANICAL MODELING

The SOFA framework allows us to divide the simulation into several components, represented in a graph as in Figure 3.4. At the root of this graph are the default components controlling the animation and the detection collision. A time integration solver which compute the dynamics of the whole simulation, associated with a linear solver is added to this node, as well as all our degrees of freedom which correspond to the vertices of the mesh.

Then the meristem topology is filled with our triangulated structure and the mass and bending force field, which are acting on the whole meristem are to be found here. Then the node split in two parts : the surface with the pressure and the stretching, and the interior which reacts on stretching, but not pressure.

Finally, a simulated AFM (a rigid sphere) enters in contact with the structure.

The main elements of this graph : the time integration method, the finite elements representing the stretching, the pressure, and the bending force field are described thereafter.

Each child node whose mechanical structure (i.e. vertices, deformation gradient...) relies on the displacement of its mechanical parent, is displaced via what we call mapping and is described in Section 3.3.2.

3.3.1 Time Integration

Our physical vertex-based model undergoes forces and the corresponding displacements are computed by solving partial differential equations. Based on the work of [Baraff and Witkin, 1998], we use a full implicit Euler solver (coupled with a conjugate gradient solver), which gives us the equations of motion through the corresponding forces. Each vertex has some coordinates x_i and velocity $\dot{x}_i = v_i$. If we denote by $x = (x_i)_{i=1...n}$, the principle of the dynamics yields the following general equation :

$$\frac{d}{dt}\begin{pmatrix} x \\ \dot{x} \end{pmatrix} = \frac{d}{dt}\begin{pmatrix} x \\ v \end{pmatrix} = \begin{pmatrix} v \\ M^{-1}f(x,v) \end{pmatrix} \tag{3.1}$$

with M the mass matrix and f a function dependant on the displacements and velocities. The implicit backward Euler method then writes, with a spatial discretisation :

$$\begin{pmatrix} \Delta x \\ \Delta v \end{pmatrix} = \tau \begin{pmatrix} v_0 + \Delta v \\ M^{-1}f(x_0 + \Delta x, v_0 + \Delta v) \end{pmatrix} \tag{3.2}$$

A first order Taylor expansion in f is given by :

$$f(x_0 + \Delta x, v_0 + \Delta v) = f_0 + \frac{\partial f}{\partial x}\Delta x + \frac{\partial f}{\partial v}\Delta v \tag{3.3}$$

and solving for v, this can be rewritten as :

$$(\mathbf{I} - \tau\,\mathbf{M}^{-1}\mathbf{D} - \tau^2\mathbf{M}^{-1}\mathbf{K})\Delta v = \tau\mathbf{M}^{-1}(f_0 + \tau\mathbf{K}v_0) \tag{3.4}$$

where τ denotes the time step, $\mathbf{K}$ the stiffness matrix ($\mathbf{K} = \frac{\partial f}{\partial x}$) and $\mathbf{D}$, the damping matrix ($\mathbf{D} = \frac{\partial f}{\partial v}$). To enter in more detail the derivation, we refer the reader to [**?**].

We have chosen $\mathbf{D}$ as the popular Rayleigh assumption : $\mathbf{D} = \alpha\mathbf{M} + \beta\mathbf{K}$. But notice that, as we are seeking a static solution, the displacement of the tip of the AFM induced by a certain amount of force, the influence of $\mathbf{D}$ is negligible.

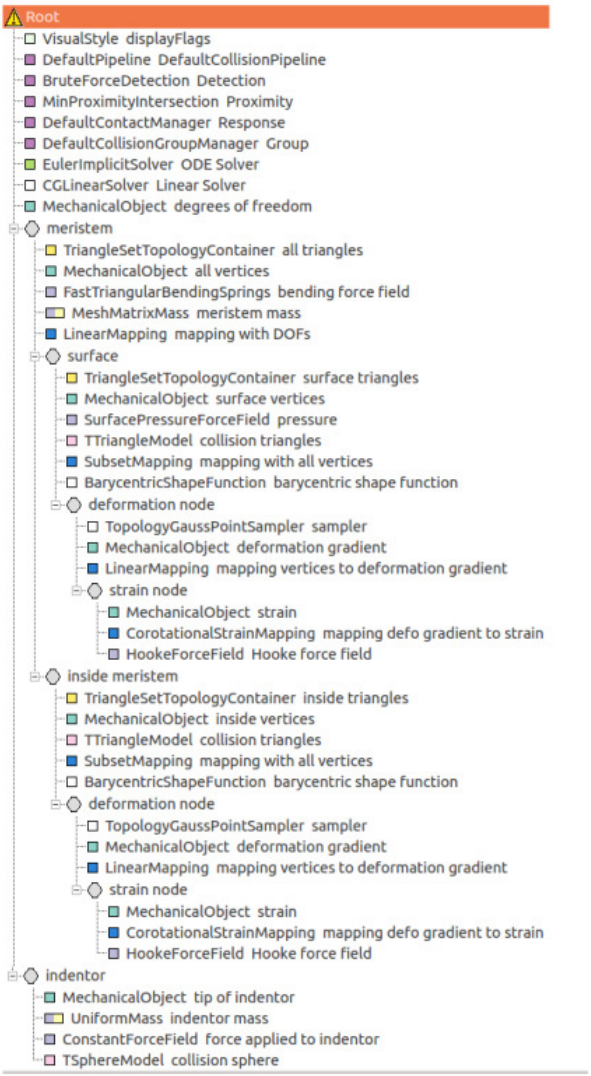

FIGURE 3.4 – *Our Sofa Graph*

The mass matrix is lumped and dependent on the mesh : for each triangle, we compute the mass by multiplying the mass density by the area of the triangle and report one third to each vertex.

The stiffness matrix depends on each force field, i.e. finite element, pressure, bending, and is computed for each force field. In the general form, it can be written as :

$$\mathbf{K}_{ij} = \frac{\partial f_i}{\partial x_j}$$

with

$$f_i = -\frac{\partial W}{\partial x_i}$$

with W being the potential energy of the corresponding force field.

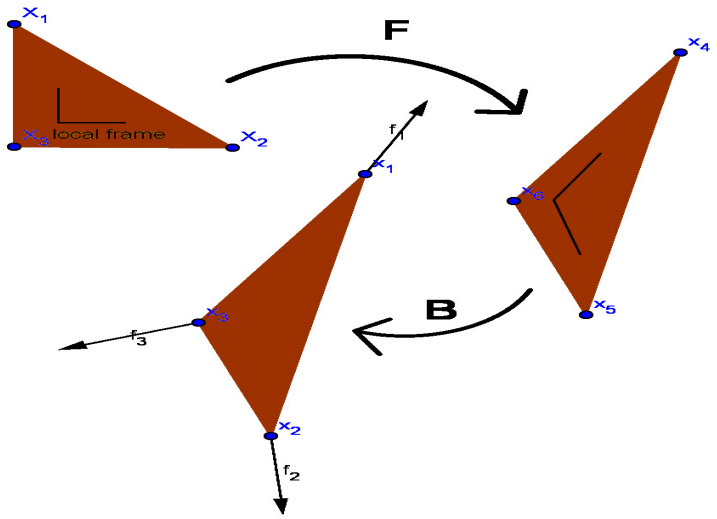

FIGURE 3.5 – *classical implementation of finite element*

3.3.2 Finite Element force fields

Each cell wall of the meristem is triangulated and has an associated finite elements force field, representing the stretching of the structure, i.e. the forces and displacements in the plane of the element. The usual way to compute some triangular finite element, as stated in [Zienkiewicz and Cheung, 1967], is to compute the forces acting on each vertex of the triangle from the displacements of these vertex, through the deformation gradient of the element as shown in Figure 3.5. Usually we start with the displacements of the 3 vertices, then we compute the deformation gradient of the element, $\mathbf{F} = \frac{\partial x}{\partial X}$ with x the displacement of the vertices and ∂X refers to the spatial differentiation. Then the strain measure, which is, in our model a corotational strain

$$\epsilon = \frac{1}{2}[\mathbf{R}^T\mathbf{F} + \mathbf{F}^T\mathbf{R}] - \mathbf{I} \tag{3.5}$$

with $\mathbf{R}$ being the rotational part of the deformation gradient $\mathbf{F}$.

Then from this strain, we calculate the stress thanks to a material law like the isotropic Hooke's law that we have used combined with a corotational strain.

$$\sigma = \lambda tr(\epsilon)\mathbf{I} + 2\mu\epsilon \tag{3.6}$$

with λ and μ the Lame coefficients.

Finally, applying the transposed of the strain-displacement matrix usually called B to the stress converts this stress into forces : $f = B^T\sigma$.

This computation is decomposed in several layers in the SOFA framework. Instead of applying the transposed of the strain-displacement matrix to the stress, which gives us directly the forces per vertex, the stress tensor produces a generalized force at the deformation gradient level, which is in turn converted to vertex forces. The communications between layers are called *mappings* (a generalization of hard bindings introduced by [Sifakis et al., 2007]). The computations traverse the layers up and down as shown in Figure 3.6. This allows more flexibility in the implementation, since we can change only one component in the SOFA graph, to choose, for instance, a non linear material law instead of a isotropic Hooke's law at the bottom layer,

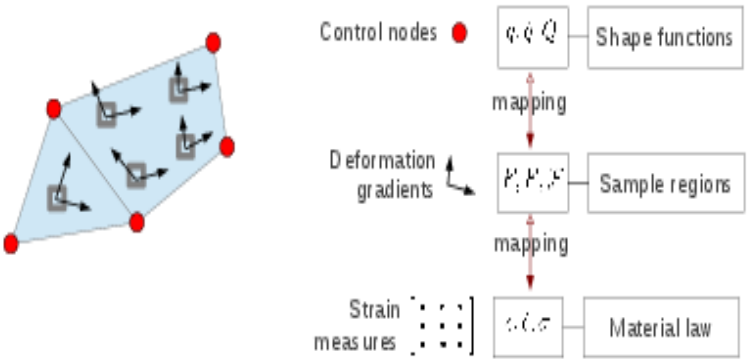

FIGURE 3.6 – *three levels of hierarchies in FE force field*

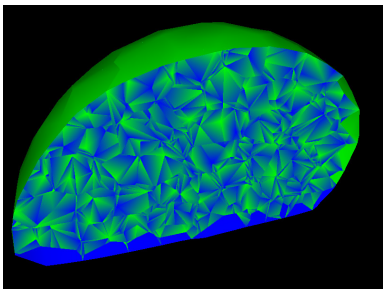

FIGURE 3.7 – *finite element modeling*

or a Green Lagrange strain instead of a corotational strain as mapping between the middle and bottom layer.

The total stretching energy is given by :

$$W = \frac{1}{2} \int \epsilon \cdot \sigma \tag{3.7}$$

Therefore the integrated stress is given by $\frac{\partial W}{\partial \epsilon}$ and the associated forces on the vertices of our elements are given by :

$$f = -\frac{\partial W}{\partial x} = -\frac{dF}{dx}^T \frac{d\epsilon}{dF}^T \frac{\partial W}{\partial \epsilon} \tag{3.8}$$

Then then generalized forces undergone by the stress tensor take the form $\frac{\partial W}{\partial \epsilon}$, which is the integrated stress, and these forces are moved upward to the parent degrees of freedom (i.e. the vertices located at the top of this hierarchy) by the transpose of the Jacobian : $\frac{d\epsilon}{dF}^T$, and $\frac{dF}{dx}^T$.

Without any prior knowledge on cell wall properties, we have chosen to implement a uniform isotropic elastic material.

Mappings

We use the mappings between each levels of the SOFA scene graph. These elements allow to compute the coordinates of a child with respect to one or more parent coordinates. The independent degrees of freedom (DOF) are on the top of the hierarchy. The mapping relation writes :

$$x_c = \mathcal{J}(x_p(t), X) \tag{3.9}$$

with X the initial mechanical state.

The velocity at the child level is given by the jacobian of the mapping :

$$v_c = Jv_p \tag{3.10}$$

with $J = \frac{\partial \mathcal{J}}{\partial x}$. Note that the positions and velocities are propagated top-down (from parents to children), while forces are moving bottom-up. The principle of virtual work states that the power of the force must be the same at the two levels, which gives the following relation :

$$f_p = J^T f_c \tag{3.11}$$

Mass and stiffness matrices can be transferred bottom-up. For instance, if the mass matrix is defined at the child level $\mathbf{M}_c$, its counterpart at the parent level is defined by : $\mathbf{M}_p = J^T \mathbf{M}_c J$.

3.3.3 Pressure force field

In addition to the finite elements model, we add inner turgor (hydrostatic) pressure, making the assumption that the pressure is regulated by the plant so that it is uniform in all the cells. This is equivalent to applying the pressure only on the surface elements. We thus apply a force to each vertex that is proportional to the area of the triangle considered and also proportional to turgor pressure, directed along the normal to the element (See Figure 3.8).

The force applied to vertex i is thus given by :

$$P_i = \frac{1}{3} A_j p \tag{3.12}$$

with A_j the area of the triangle j to which the vertex i belongs, and p the constant turgor pressure in the floral meristem.

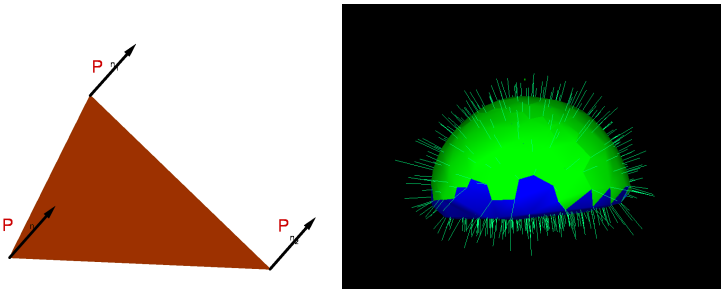

FIGURE 3.8 – *Meristem with pressure represented by arrows*

3.3.4 Bending force field

Finally, computing the bending energy reveals that at low pressure (in plasmolyzed state), bending cannot be negligible. Therefore we implemented the bending model of [P.Volino and Magnenat-Thalmann, 2006], which remains quite accurate for low bending, with low computational cost. In [P.Volino and Magnenat-Thalmann, 2006] the bending is represented via linear springs depending on the curvature between two elements. Their idea is to compute a "bending vector" linearly dependent of the vertices positions. This vector is then applied as a force proportionally to the bending stiffness of the surface.

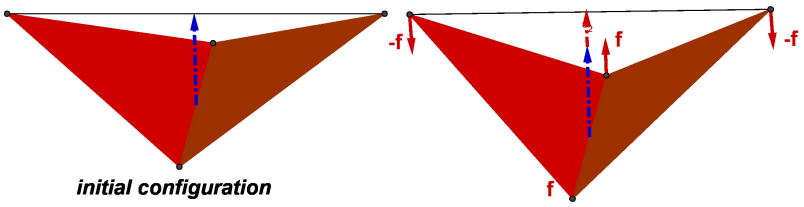

FIGURE 3.9 – *linear bending*

	Young modulus (E)	Pressure (P)	Poisson ratio (ν)	Bending stiffness (μ)
model	50 - 1000 Pa	0 - 40 Pa	0.49	1.8 - 35 J
experimental	1 - 1000 MPa	0.1 - 1 MPa	unknown	unknown

	cell length (L)	wall thickness (h)
model	5 - 10 m	0.7 m
experimental	5 μm	0.1 - 1 μm

FIGURE 3.10 – *Table of typical physical parameters*

This model introduces a bending stiffness, which acts linearly on the forces per vertices. As we are seeking physical parameters, this stiffness must not be chosen arbitrarily, but rather defined from properties of the cell walls.

To scale this bending stiffness, we restart from the equations of elastic thin shells [Landau and Lifchitz, 1970], from which we get the moment per unit of length of bending forces applied to a shell :

$$M = \frac{Eh^3}{12(1-\nu^2)}\gamma \tag{3.13}$$

with E the young modulus, h the thickness of the shell, ν the poisson ratio and γ the radius of curvature. This can be put in correspondance with [P.Volino and Magnenat-Thalmann, 2006] where the moment is given by :

$$M' = l\mu\gamma \tag{3.14}$$

with l the length of the edge between two adjacent triangles, μ the bending stiffness.

By identification the bending stiffness is :

$$\mu = \frac{Eh^3}{12(1-\nu^2)} \tag{3.15}$$

3.3.5 Simulated AFM

Our simulated AFM is a simple sphere of diameter comparable to cell size. We apply a given force in one direction orthogonal to the meristem and we quantify the depth reached by the sphere at equilibrium.

3.3.6 Physical parameters

The main physical parameters of the simulation are summarized in table 3.10. Two different sets of independent parameters constitute our model : on the one hand, the geometrical

parameters (cell length, cell wall thickness), and on the other hand, the material parameters (Young modulus, Poisson ratio, pressure constant and bending stiffness).

We have scaled our parameters, in order to respect the ratio of experimental data.

$$1 \leq \frac{E}{P} \leq 1000, \quad \frac{L}{h} \approx 0.1$$

with L the size of a cell, and h the thickness of its wall. The poisson ratio was chosen so that the material is almost incompressible, while the bending stiffness was calculated according to equation 3.15.

3.4 VALIDATION IN A SIMPLE CASE

To validate our method, we implemented Atomic Force Microscopy on a single plane shell, for which we can compare our curves to analytical results. This simplified model also allows us to find the good trade-off between precision and rapidity of the simulation, as it enables us to tune different criteria, as the number of subdivision steps for the triangles indented, or the precision at which we stop the simulation. The typical dimensions of the plane are that of a cell in the meristem mesh.

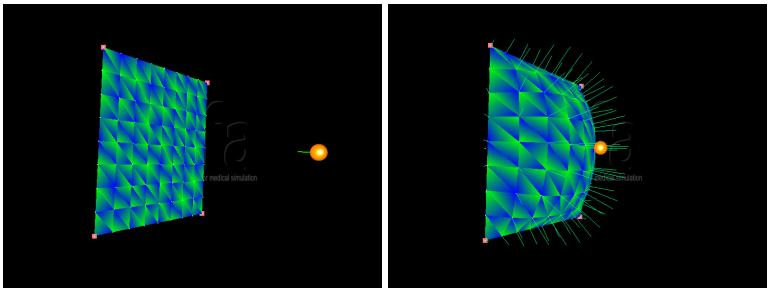

FIGURE 3.11 – *Simplified model used for validation, without and with pressure*

Our simplified model is a square plate undergoing stretching and possibly submitted to a pressure force pressure (Figure 3.11) and the AFM indentor is also represented as a sphere. This simplified model does not take any bending into account since we want to compare it to analytical formulae from the literature.

In Figure 3.12 the sensitivity to the pressure can be seen. The force-displacement curves are straight lines when the plate is submitted topressure, which is in agreement with the analytical model in [Vella et al., 2012a], and the slope of these lines depends on the value of pressure ; whereas Figure 3.13 shows that, with zero pressure the curve is well approximated by cubic function cx^3, which is in agreement with the analytical model given in [Landau and Lifchitz, 1970].

Thus, the simplified model captures the properties of the structure, i.e. the internal pressure and the elastic modulus of the cell walls. The indentation process is also completely reversible as we have chosen to implement an elastic law (Hooke's law for the finite elements) as can be seen in Figure 3.14 : the curve representing indentation almost perfectly matches the de-indentation one, which also demonstrates the convergence of the simulations.

An other advantage of this structure is that it allows us to tune parameters such as the criteria to stop simulations (see Figure 3.15) : when the positions and velocities of the vertices of our model drop below threshold values, we stop the simulation. As can be seen in Figure 3.15,

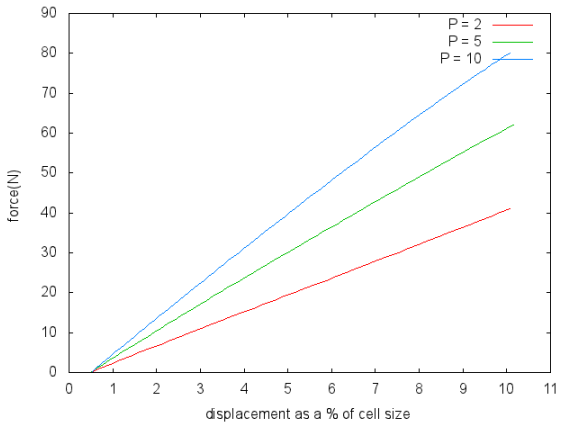

FIGURE 3.12 – *Sensitivity of curves to pressure*

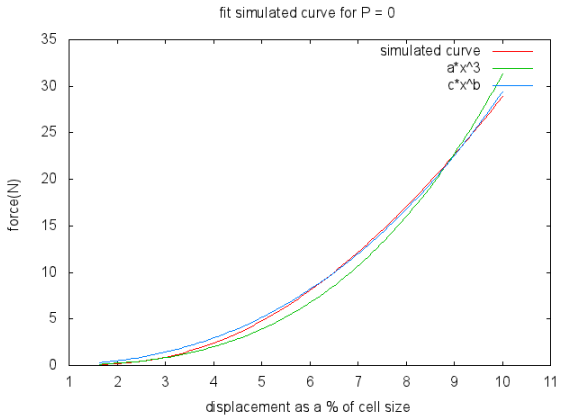

FIGURE 3.13 – *Curves without pressure fitted by polynomials*

the precision needed is at least 10^{-3}m while a typical cell size is between 5 and 10m, and the whole meristem structure is around 80m.

For the subdivision of the triangles of the mesh, we have tried different levels of refinement, (as can be seen in Figure 3.17) and followed the process described in Figure 3.16. Each original triangle is split into 4 smaller triangles, whose vertices are the original vertices and the middles of the original triangle's edges. The geometrical properties of the subidived topology is closed to the previous one and does not lead to degenerate triangles (having great disparity in edges' length).

The curves converge quite rapidly after a given number of subdivision steps. We thus stop the subdivision process when the differences between the curves is small enough. However, small triangles require a small the time step to avoid oscillations (which slows down convergence). A good trade-off has then to be found between the number of subdivisions and the precision, in order to obtain enough accuracy but with sufficiently fast algorithms. Increasing the number of subdivision steps beyond this level does not improve precision, which led us to stop the subdivision process at 16.

Using the SOFA framework, the whole force vs displacement curves of AFM on a single plane is computed in less than a minute with sufficient precision of 1E-3 .

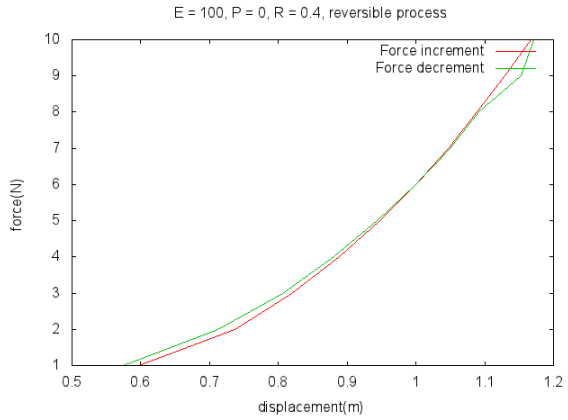

FIGURE 3.14 – *process is reversible as indentation matches de-indentation*

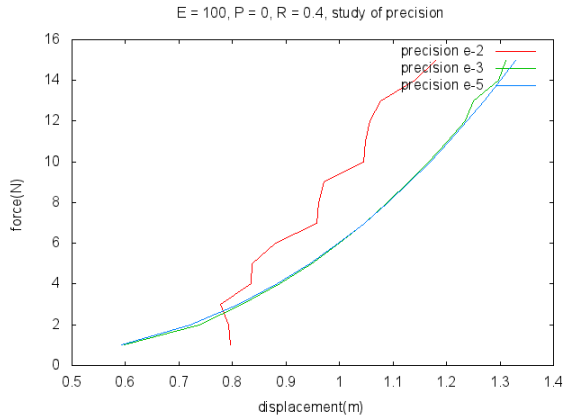

FIGURE 3.15 – *sensitivity of curves to precision criteria*

3.4.1 Range of parameters

As potentially thousands of degrees of freedom are involved in such 3D model, the problem of fitting physical parameters with respect to simulation and experimental data is often ill-conditioned and not invertible. However, dimensional analysis allows us to compare the ratio between forces and displacement, obtaining by solving many direct problems.

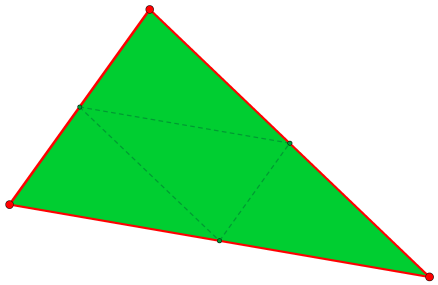

FIGURE 3.16 – *process to subdivide a triangle of our mesh*

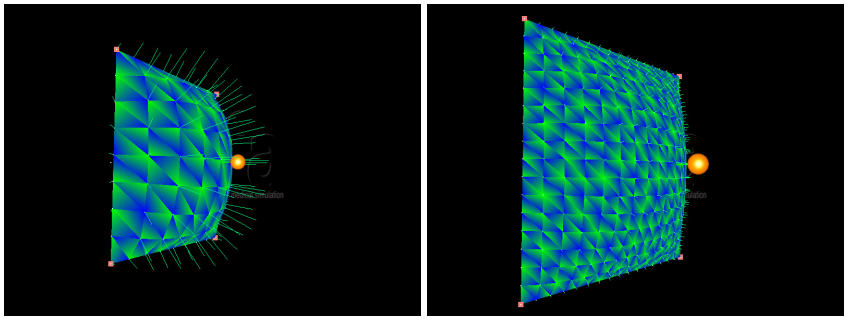

FIGURE 3.17 – *Different levels of subdivision*

To get non-dimensional parameters we scaled the forces, F, with respect to Young Modulus and cell length, and the indentation, I, with the cell length :

$$[F] = \frac{F}{EL^2}$$

$$[I] = \frac{I}{L}$$

Experimental data without internal pressure (plasmolyzed state) were obtained by [Peaucelle et al., 2011], where a typical displacement of $0.5\mu m$ was observed for a given force of around $1\mu N$. Replacing these parameters in $\frac{[F]}{[I]}$ gives us around the same value as our model, where, for a typical displacement of 10% of cell size also, we need an amount of force of around 400N, for a Young modulus of 1000Pa.

Our model is thus positioned in an acceptable range of values.

3.5 RESULTS AND DISCUSSION

3.5.1 Homogeneous elasticity of cell wall

The first simulations we performed were with an homogeneous elastic modulus as can be seen Figure 3.18a. In this case, at 0 pressure, we obtain different curves if we indent in the middle of a cell or near an anticlinal wall. The latter being stiffer than the former as can be seen Figure 3.18b : with the same elastic modulus, more forces should be applied to the indentor to reach the same depth. The curves obtained at 0 pressure and with indentation in the middle of a cell (red curves Figure 3.18b) are well fitted by polynomials of type : $y = ax^b$, b being constant while a linearly depends on the elastic modulus (red curve Figure 3.18c). Whereas, when indenting near an anticlinal wall at 0 pressure (curves green and blue Figure 3.18b), the beginning of the curve is linear and directly proportional to the elastic modulus (curve green Figure 3.18c), whereas the end of the curve is well fitted by polynomial of type $y = ax^b$, with b being constant and a linearly depends on the elastic modulus (curve blue Figure 3.18c).

Thus under these hypothesis : at 0 pressure and with a constant elastic modulus, we can roughly invert the problem of finding the mechanical properties of the cell walls through the results of some indentation experiments. Indeed, through a single curve, either corresponding to an indentation in the middle of a cell or near an anticlinal wall, we can retrieve the elastic modulus by fitting the curve with the appropriate polynomial.

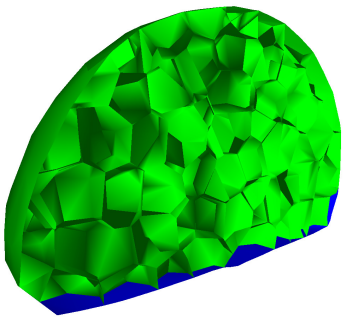

(a) homogeneous elasticity in the whole meristem

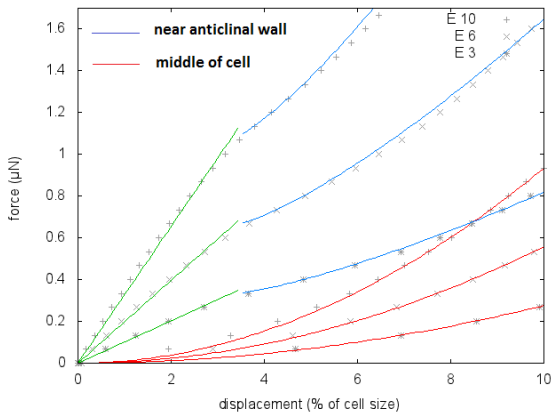

(b) P = 0, different elastic modulus, indentation near anticlinal walls and in the cell middle

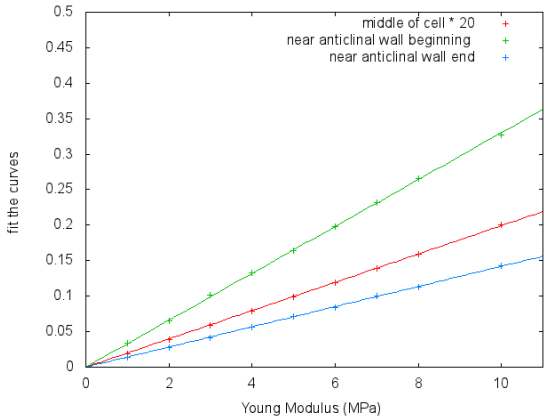

(c) polynomial coefficients fitting previous curves depends on elastic modulus

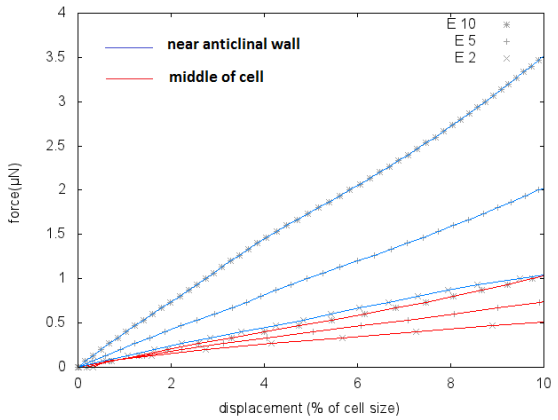

(d) P = 5, different elastic modulus, indentation near anticlinal walls and in the cell middle

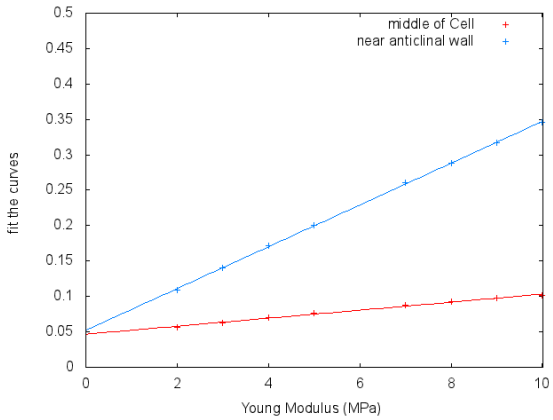

(e) polynomial coefficients fitting previous curves depends on elastic modulus

FIGURE 3.18 – *indentation of meristem with homogeneous elasticity, with different pressures and at different locations*

When the pressure is not null anymore, curves tend to be more linear as can be seen Figure 3.18d, either when indenting near an anticlinal wall (curve blue) or in the middle of a cell (curve red). Indeed, if we fit these curves with linear ones, the coefficient we obtain depends on

an affine way of the elastic modulus Figure 3.18e for a given pressure. But when changing the pressure, the affine relationship changes and no simple dependance exists through the pressure coefficient.

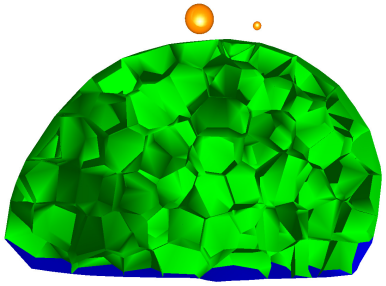

(a) sphere size impact : two sizes of sphere are studied

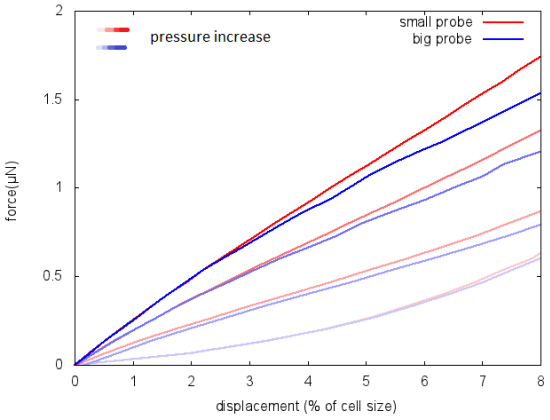

(b) sphere size impact middle of cell

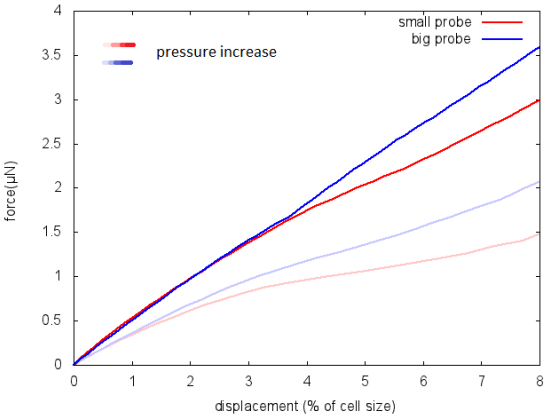

(c) sphere size impact near anticlinal wall

FIGURE 3.19 – *indentation of meristem with homogeneous elasticity, with different pressures and at different locations*

The impact of the probe size can be studied, when indenting at different pressure in the midlle of a cell (Figure 3.19b) or near anticlinal wall (Figure 3.19c). Investigating the impact of probe size at low pressure, when indenting in the middle of a cell revals that its influence under these conditions is negligible (the blue and red curves at low pressure Figure 3.19b are almost the same). Whereas, when rising the pressure, the influence of probe size can not be negligible anymore (blue and red curves at high pressure Figure 3.19b tend to disconnect from each other) after 4 or 5% of indentation in term of cell size.

Figure 3.19c reveals that sphere size impact near anticlinal wall is not negligible after also 4 or 5% of indentation in term of cell size. On the contrary to previous figure, the impact of sphere size is not negligible at low pressure. It seems on the contrary more relevant than at high pressure since its impact can be seen after only 1 or 2% of indentation.

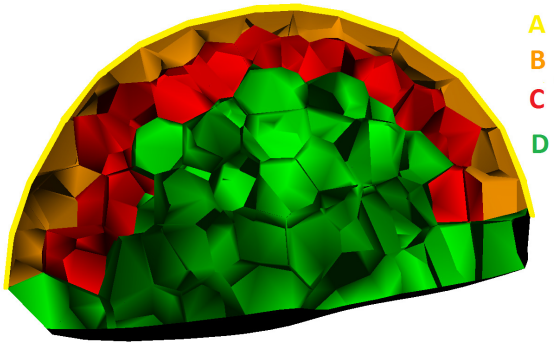

(a) elasticity varying following the layers in the meristem

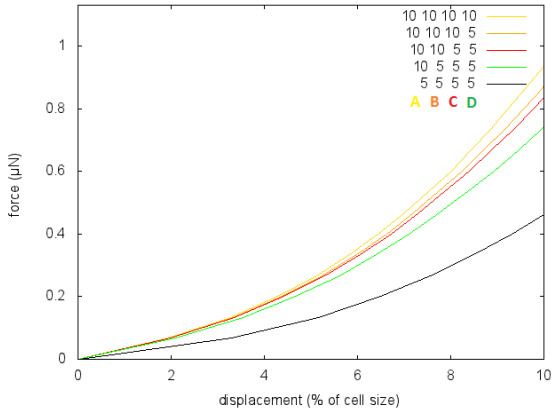

(b) P = 0, different elastic modulus, indentation in the cell middle

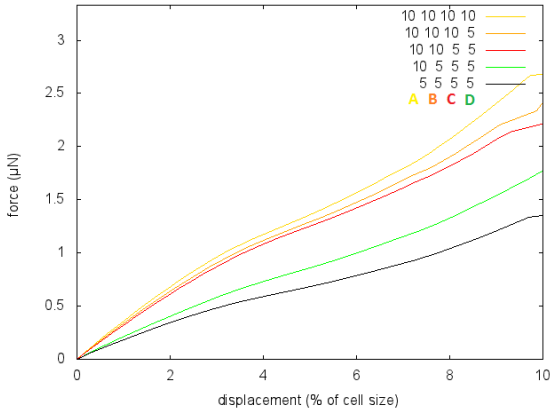

(c) P = 0, different elastic modulus, indentation near anticlinal walls

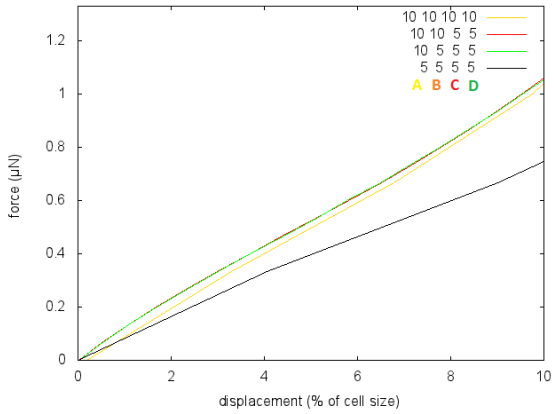

(d) P = 10, different elastic modulus, indentation in the cell middle

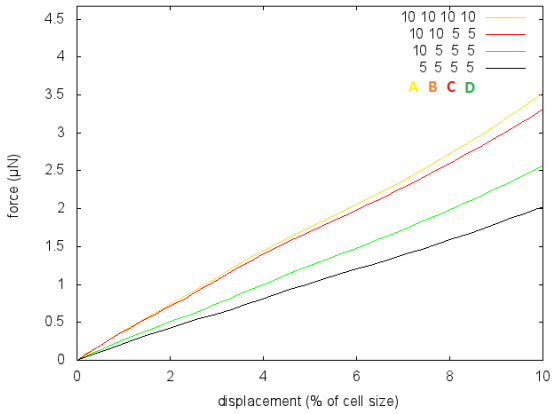

(e) P = 10, different elastic modulus, indentation near anticlinal walls

FIGURE 3.20 – *indentation of meristem with elasticity varying following the layers, with different pressures and at different locations*

3.5.2 Cell wall elasticity differs by layers

In this part, cell wall elasticity varies with the different layers as can be seen Figure 3.20a. We start with a given elastic modulus and gradially change the elastic modulus of the different

layers to finally get an elastic modulus of half the previous one.

When indentation is realised at 0 pressure in the middle of the cell (Figure 3.20b), we can observe a smooth transition from a given elastic modulus to an elastic modulus 2 times lower, by changing the properties of the different layers. When the two first layers are at a given elastic modulus, and the inner layers are 2 times lower, the curves is slightly lower than when the elastic modulus is constant. Thus we can deduce that the first 2 or 3 layers should have impact on indentation whereas the more inner layer may have a negligible impact. If we change the elastic modulus of the 2nd layer by deviding it by 2 (like the inner layers), the curve decreases, if we just keep the surface at a given elastic modulus, the curve decreases again. There is a quite smooth transition from one curve to the next. But changing after the elastic modulus of the surface changes a lot the curve since we are then at a constant elastic modulus 2 times lower thant the first one and the curve jumps from the last curve to this one.

When indentation is realised at 0 pressure, near anticlinal wall (Figure 3.20c), like in the middle of the cell (previous image), there is a smooth transition from a given elastic modulus as long as the anticlinal wall and the surface of the L1 is the same. But on the contrary to previous image, when the elastic modulus of the anticlinal wall of the L1 changes, there is a gap in the curves, as well as when the elastic modulus of the surface changes. We can then conclude here that the properties of the anticlinal wall of the L1 are of more importance than when indenting in the middle of a cell.

When pressure is taken into account and indentation is performed in the middle of a cell (Figure 3.20d) ,only the elastic modulus of the surface is relevant there. On the contrary when we indent at a given pressure near anticlinal wall (Figure 3.20e), the anticlinal walls of the L1 as well as the wall of the surface are relevant.

3.5.3 Cell wall elasticity changes locally

In this part, local elasticity near the impact of the indentor is changed (see Figure 3.21a). We start with a given elastic modulus and change it locally with different radii in order to obtain in the end an elastic modulus half the previous one.

When indentation is performed in the middle of a cell with 0 pressure (Figure 3.21b), if the radius of the local stiffness is the one of three cells, the results are the same as with a uniform elastic modulus. Which confirm the results of the previous figure that only the 3 first layers plays a role in indentation under these hypothesis (no pressure and indentation in the middle of a cell). Then decreasing the radius of the local stiffness, makes a transition to a structure with half the given elastic modulus.

When indentation is performed near anticlinal wall at 0 pressure (Figure 3.21c), unlike the previous figure, only the two first layer plays a role in indentation. Otherwise the results are really similar for the two first layers.

When indentation is performed in the middle of a cell for a given pressure (Figure 3.21d), all the layers seem to play a role, since we get a smooth transition from a given elastic modulus constant over the structure and when we locally change cell by cell this elastic modulus. It may be explained by the fact that under pressure, the meristem growth is different when the elastic

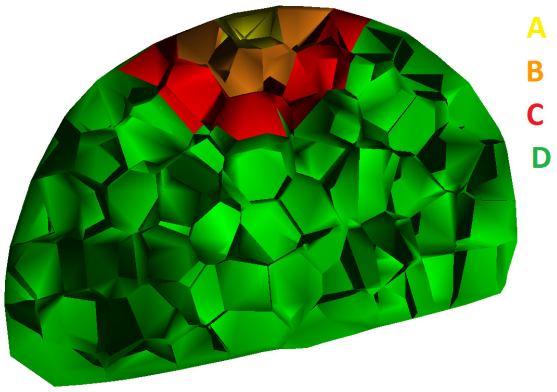

(a) elasticity varying locally in the meristem

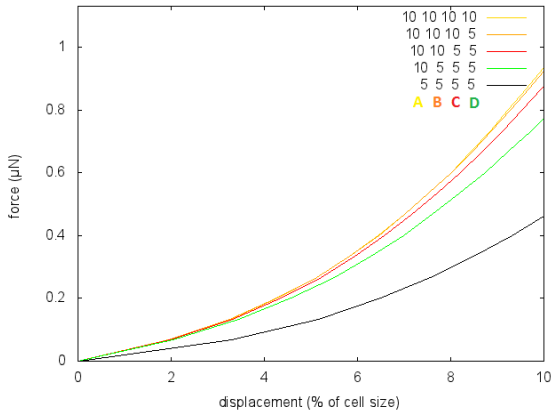

(b) P = 0, different elastic modulus, indentation in the cell middle

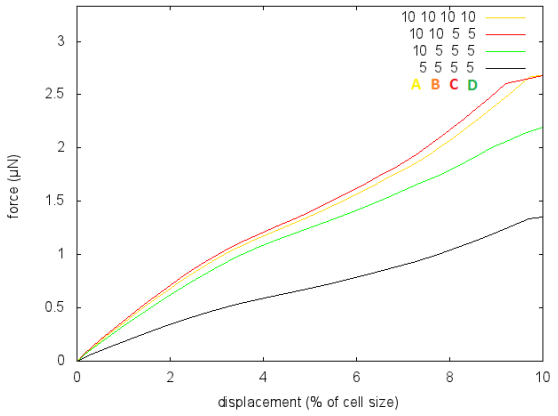

(c) P = 0, different elastic modulus, indentation near anticlinal walls

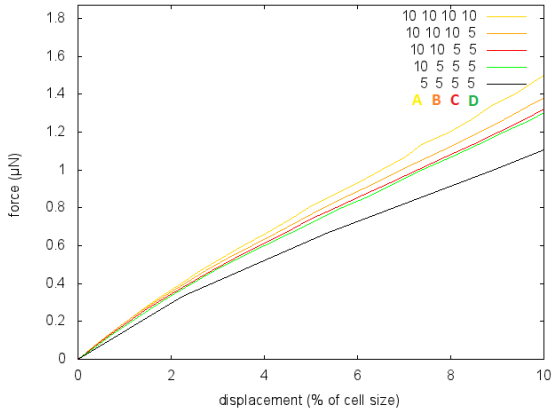

(d) P = 10, different elastic modulus, indentation in the cell middle

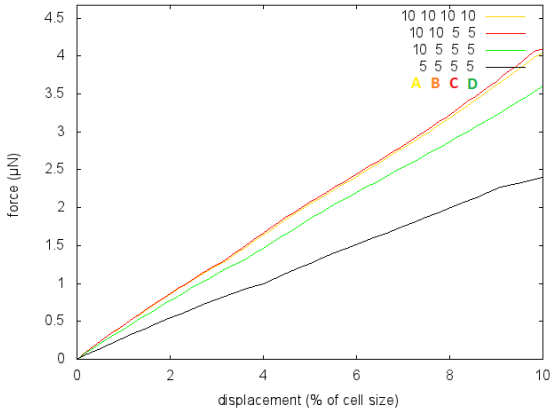

(e) P = 10, different elastic modulus, indentation near anticlinal walls

FIGURE 3.21 – *indentation of meristem with elasticity varying locally, with different pressures and at different locations*

modulus changes. So the initial state in which the meristem is indented (the organ inflated un-

der pressure), is different in all these cases.

When indentation is performed near an anticlinal wall at a given pressure (Figure 3.21e) with a radius of 2 cells around the impact of the indentor, the result is the same as with a given elastic modulus. This results emphasize the fact that indenting near an anticlinal wall measures the properties of the surface locally and of the anticlinal wall of the L1 locally.

3.5.4 Anisotropy

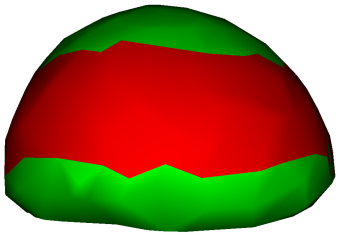

(a) Anisotropy in surface around the meristem

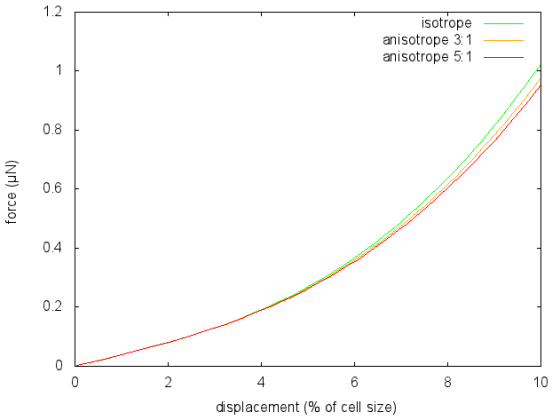

(b) P = 0, different anisotropy degree, indentation in the cell middle

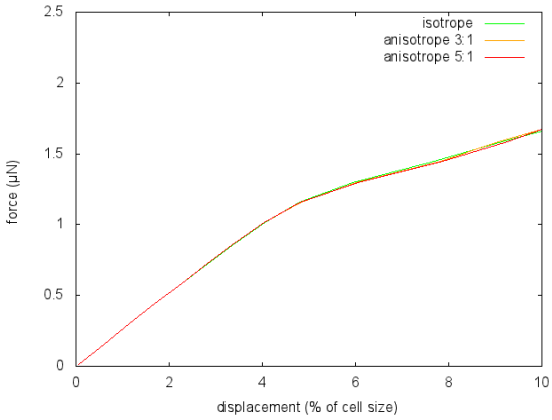

(c) P = 0, different anisotropy degree, indentation near anticlinal walls

FIGURE 3.22 – *indentation of meristem with different degree of anisotropy in surface, at different locations*

In this part, the surface of the meristem is locally anisotropic in the direction of the circumference as can be seen in figure 3.22a. The degree of anisotropy varies from 1, which is totally isotropic, to 5 where the elastic modulus in one direction is 5 times higher than in the other perpendicular direction. Indentation is realized with no pressure and at different locations (near an anticlinal wall or in the middle of a cell).

When indenting in the middle of a cell, one can observe that anisotropy allow for a softer apparent cell wall (Figure 3.22b). However this results is valid only after 6 to 7% of indentation in term of cell size. For lower indentation, curves tend to be identical. When indenting near

an anticlinal wall, no differences arise from the model, since the effect of anticlinal walls is dominating the effect of the surface (see Figure 3.22c).

3.5.5 Robustness of the model

To explore the influence of the geometry on the results, we tried to change the structure by moving all vertices by a random number. Then choosing this random number as around one sixth of the cell size does not lead to great change in the curves since their variability is the same as indenting one cell from another with the original structure.

3.6 CONCLUSION AND PERSPECTIVES

We proposed here a framework to systematically study Atomic Force Microscopy curves on a plant organ. This method has been applied to the meristem but may also be applied to any other type of plant organ.

Exploring the whole space of parameters indicates the influence of many different factors on every curves. Thus biologists should be really careful as for the conditions underlying the use of A.F.M. Because each hypothesis made may lead to a different result : either indentation near anticlinal wall or in the middle of the cell, in a plasmolysed state (without pressure) or with a given pressure, indenting with a small probe or with a big probe...

We can then, under the light of the simulation, reread some experimental results.

In [Peaucelle et al., 2011], the authors make the assumption that with a big probe, they are sensitive to the internal layers, whereas with a smaller one, they are only sensitive to the L1. We should say, that our model has not enough level of detail to compare with probes that are more than two order smaller than a cell size (as can be found in [Milani et al., 2014]). Nevertheless, for bigger indentor, our simulation fit relatively well with such an assumption, when indenting in a plasmolysed state : with probes of the size of a cell we are sensitive to internal layers (at least the first three layers), whereas with a smaller probe, we are more sensitive to the L1, unless great disparity in elasticity in the organ do exist.

But in turgid state, the model shows that we are more sensitive to pressure and elasticity of L1, even with a relatively big probe. So measurements in this state should reveal the impact of pressure as well as the one of elasticity and taking apart each of this effect is a complex task.

Finally, drawing parallels with experiments made on other plants can reveal some limits of the model. For instance [Kierzkowska et al., 2012] finds that in a turgid state, experiments on onion skin, reveals a lower apparent stiffness above anticlinal wall, than in the middle of cells, which may seem counter-intuitive. This surprising result may be explained by the fact that an additional material takes place above anticlinal wall of the L1, which is softer than the rest of the cells. But as there is no thickness in our model, such a result can not be retrieved. Taking into account the thickness of the cell wall may then lead to other interesting results and could provide a natural future development of our model.

3.6.1 Concluding remarks

Exploring the space of parameters from the model indicates that different factors play a major role in AFM measurements. The key factors as shown by the force-displacement curves are :

— tip size of the AFM,
— properties of the structure, i.e. elastic modulus, turgor pressure,
— localization of indentation : near anticlinal walls or in the middle of cells.

However these factors are combined, which means that experiments require a careful interpretation, since none of these parameters can be isolated from the others to entirely explain the curves obtained. The framework that we present here allows a comprehensive exploration of all assumptions.

We have presented in this chapter a physically based model of meristem coupled with a simulated Atomic Force Microscope. This has lead us to develop a comprehensive framework accessible to biologists, in order to verify assumptions that were still not clear, as no theoretical model was available in order to draw conclusions from experiments.

Nevertheless a weak point of our method is the rapidity of the algorithms, which may take a few hours to extract a force-displacement curve composed of dozens of points.

As the deformation of the structure of the organ considered is only local, the model may be composed of several cells that are playing almost no role in the simulation, but are still represented. Thus, an interesting approach would be to add details in simulation, only where needed : in the contact zone for instance.

That is currently what we propose in the next chapter, through a novel coupling approach : the Multifarious Hierarchy of Mechanical Models, which consists in adding a detailed simulation to a coarse one, without adding redundancy in the degrees of freedom, or in the computed forces for the underlying models.

ACKNOWLEDGEMENTS

To the whole Sofa team for their everyday support, especially Benjamin Gilles for outstanding plugins. To P. Das, J. Chopard and F. Boudon for the realistic structure of meristem. To O. Ali for suggesting dimensional analysis.

CHAPTER

4

MULTIFARIOUS HIERARCHY OF MECHANICAL MODEL

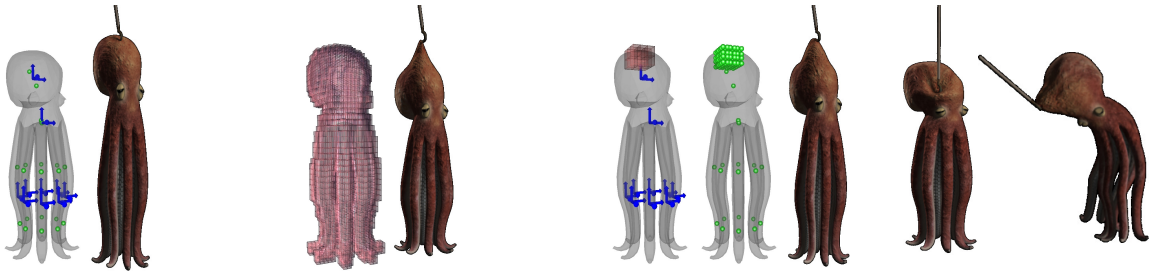

(a) Coarse frame-based simulation

(b) Fine FEM simulation

(c) Mixing a coarse frame-based simulation to a local FEM patch with our method

FIGURE 4.1 – *Using a hook to catch a coarsely discretized, frame-based octopus is challenging due to the lack of deformation at the contact point (4.1a). One could resolve this problem with a high-resolution set of finite elements (4.1b) but, at the expense of runtime performance. Multifarious Hierarchies of Mechanical Models allow arbitrarily located detail simulations to be easily combined with underlying coarse deformation models to achieve accuracte deformation response without sacrificing peformance (4.1c). An octopus pulled by a hook. Coarse affine frames (blue), fine embedding FEM (red), integration points (green). (4.1a) : A coarse simulation cannot capture fine deformation around the hook. (4.1b) : The fine simulation as a reference. (4.1c) : Our approach : (from left to right) non-nested, arbitrarily located detailled FEM model (red) combined with coarse affine frames (blue). Integration points (green) are distributed automatically, with higher density in the fine deformation area. The frame-based simulation achieves the global deformations while local deformation are possible around the hook thanks to local FEM.*

This work has been done with B. Gilles, D.I. Levin, M. Nesme and F. Faure.

4.1 ABSTRACT

We present a new framework for level of detail in solid simulations. Simulated objects are simultaneously embedded in several, separately designed deformation models with their own independent degrees of freedom. The models are ordered to apply their deformations hierarchically, and we enforce the unicity of the dynamics solutions using a novel kinetic filtering operator designed to ensure that each child only adds detail motion to its parent without introducing redundancies. This new approach allows artists and engineers to easily add fine-scale details without introducing unnecessary degrees-of-freedom to the simulation or resorting to complex geometric operations like anisotropic volume meshing. We illustrate the utility of our approach with several detail enriched simulation examples.

Computational Physics has become an indispensable tool for many disciplines, including computer graphics. Algorithms for simulation are widely utilized for tasks ranging from biomechanical analysis to surgical training to animating scenery and characters in the latest video games and hollywood blockbusters. Commensurate to this, we have seen the development of a myriad of methods for numerical simulation. Typically, each method is well-suited to simulate a particular phenomenon at a particular resolution. For instance, Finite Elements have been used to simulate solids and fluids. They generally require fine meshes to capture local detail, resulting in slow computation times. Alternatively, modal subspace or frame-based methods

can accurately simulate the coarse motion of an object with a small number of Degrees-of-Freedom (DOFs), but have difficulty capturing the fine-scale details. No single methodology is ideal for handling all the types and scales of motion that may occur during a given simulation. Accordingly, the search for such methods is still an open problem.

Currently this problem is addressed with specialized algorithms which can be divided into two classes : refinement approaches and coupled approaches. Refinement approaches alter the number of DOFs in the simulation as a function of performance and accuracy. Refinement algorithms have several drawbacks. First, they are not general, a refinement operation for a particular discretization will probably not be applicable to a different one (i.e. a triangle edge split cannot be used to refine a hexahedral mesh). Second, refinement is not guaranteed to be a local operation, as such it is difficult to predict what effect it will have on the overall simulation. Finally, refinement algorithms can be difficult to implement, especially in 3D. On the other hand, coupled approaches avoid refinement by using two (or more) simulation techniques which operate on different scales. These methods are common for turbulence simulation in fluids wherein a coarse fluid simulation is coupled (one-way or two-way) to a fine scale turbulence model. Coupled methods avoid refinement but current formulations are not sufficiently general for wide-ranging application.

In this paper we propose a new coupling approach to multi-scale simulation : the Multifarious Hierarchy of Mechanical Models (MHMMs). Multifarious Hierarchies are a general approach that allows a motion to be decomposed using a set of arbitrary, overlapping degrees-of-freedom. For instance, local detail can be added to coarse deformations by embedding a part of the model in a fine FE mesh (Fig.4.1). The geometry in the overlapping region experiences a hierarchically combined deformation field and this eases modeling since no geometrical operation is required to achieve the coupling. Furthermore, it increases computational efficiency due to the small total number of independent DOFs. To achieve physically sound coupling of the models, we introduce a novel Kinetic Filter to automatically cancel out redundancies between the deformation fields, and to consistently distribute the forces across the models.

MHMMs are fast, allowing tight control of the number of DOFs used to perform a simulation but they accomplish this without relying on complicated refinement operations. They reduce the construction of robust, high-performance, multi-scale simulation algorithms to compositions of existing techniques yielding a whole that is greater than the sum of its parts.

Contributions

The major contribution of this work is a general formulation for Multifarious Hierarchies of Mechanical Models : A method for superimposing deformation models of differing resolutions in an easy and physically sound manner. MHMMs allow for efficient, detailed numerical simulations and in comparison to other methods, have the following advantages :

- *General* : Any combination of discretizations or deformation models can be combined into a hierarchy
- *Fully-Coupled* : Forces and motions applied at one hierarchy level are propagated to the rest of the hierarchy
- *Spatially-Varying Layers* : Deformation models can be applied globally or locally allowing detail to be limited to appropriate regions of the domain (i.e. at contact points etc...)
- *Layers of Varying Dimension and Material* : Combine rods, shells and volumetric models seamlessly ; the detail can be used to represent a different material from the coarse model

— *Arbitrary Number of Levels* : The extension to more than two levels allows a tight control of the resolution of the detail
— *Efficient* : MHMMs can be decomposed into independent systems that can be solved in parallel at runtime
— *Controllable* : Users can add additional detail to a simulation with the guarantee that underlying gross motion will be unaffected.

The remainder of our paper is organized as follows. Background is provided in sections 4.2 and 4.3, while our contributions are explained in sections 4.4 through 4.6. Results are presented in sections 4.7 and 4.8.

4.2 RELATED WORK

Adding relevant fine-scale details has long been an important area of research in graphics and engineering. As in the introduction we can divide previous methods into refinement approaches and coupling approaches. We begin by reviewing refinement approaches which can themselves be categorized by their degree of h-adaptivity and p-adaptivity. H- and p-adaptivity describe the ways in which simulation methods attempt to balance fidelity and performance. H-adaptive methods concern themselves with introducing new degrees-of-freedom by splitting individual elements while p-adaptive methods increase the degree of the polynomial approximation used for field variables. Both approaches have been well studied. In terms of h-adaptivity. Debunne et al [Debunne et al., 1999] introduce a multi-resolution, particle-based methodology for simulating linearly elastic objects. They provide a formalism for dynamically adding and removing particles in order to maintain a desired level of accuracy, and to locally switch between resolutions. Other h-adaptive remeshing approaches for Finite Element Simulation have been proposed, most recently in the context of thin shells, elastoplastic simulation and mixed fluid solid simulations [Wicke et al., 2010,Narain et al., 2012,Clausen et al., 2013,Narain et al., 2013]. However, these techniques are limited to triangular and tetrahedral meshes which are unsuitable for many applications [Belytschko et al., 2000]. Grinspun et al [Grinspun et al., 2002] present a h-hierarchical approach which reformulates remeshing as basis refinement. Their method is generally applicable to all element types but is limited to a single mechanical model and aligned levels of detail. This can require complicated mesh coarsening as a preprocessing stage. P-adaptive methods suffer from similar problems. Because the polynomial basis is refined, p-adaptive methods begin with a coarse mesh that reasonably captures the geometry. As such, mesh generation can be problematic [Szabó et al., 2004].

Next we review coupling approaches which attempt to add detail to a simulation by "gluing" differing representations of an object together. These methods can be further divided into surface embedding methods, attachment methods and overlaying methods. Surface methods augment coarse volumetric simulations with high-resolution surfaces. Attachment methods provide a mechanism for coupling two different, non-overlapping simulations and overlaying methods use the superimposition of overlapping discretizations to add detail.

Surface embedding methods are popular in graphics and are used to retain reasonable surface detail for rendering while achieving fast simulation speed. Muller et al [Müller et al., 2002] use barycentric coordinates to map a coarse deformation to a high resolution surface mesh. Similar approaches have been used to simulate viscoelastic objects with thin features [Wojtan and Turk, 2008] as well as liquids [Wojtan et al., 2011]. Wojtan et al [Wojtan and Turk, 2008, Wojtan et al., 2011] use the surface to track features but limit its influence on the underlying simulation (limited to computing surface tension forces). Some recent approaches

procedurally deform the embedded surface, either from geometric analysis [Rohmer et al., 2010] or based on examples [Wang et al., 2010, Seiler et al., 2012, Zurdo et al., 2013]. In these methods the fine detail cannot fully respond to user manipulation, relegating it to a more cosmetic role. In general these methods only deal with high-resolution detail at the surface of an object.

Attachment methods have also received a great deal of focus since Sifakis et al [Sifakis et al., 2007] proposed a general methodology to connect models on mesh boundaries. Twigg et al proposed Point Cloud Glue [Twigg and Kačić-Alesić, 2010] to easily attach any sets of points using the Procrustes transform. Because simulations of differing resolutions can be attached, this method could be used to resolve details at certain parts of the model. However, attachment methods lack a mechanism for dealing with overlapping discretizations and so dynamic level-of-detail in a particular simulation domain would require an additional refinement algorithm. Furthermore, there are complications when allowing the detail level to be fully dynamic. Other methods based on substructuring are also commonly applied in engineering and graphics [Barbič and Zhao, 2011, Kim and James, 2012]. Often per-component reduced models are used to improve performance. Again, an additional algorithm for controlling level-of-detail within each substructure is required.

Overlapping methods have also been explored since the early work of Faloutsos et al [Faloutsos et al., 1997] where local Freeform deformation (FFD) lattices are embedded into larger global ones to allow for fine grained animator control. This method illustrates a particular instance of an MHMM and in our paper we focus on generalizing the concept to layerings of arbitrary discretizations. Two-way coupled algorithms were initially explored by Terzopoulos and collaborators [Terzopoulos and Witkin, 1988, Terzopoulos and Metaxas, 1990] using hierarchies of superquadrics imposed on rigid frames. More recently, Remillard et al. [Rémillard and Kry, 2013] embed a high-resolution thin shell inside coarse FEM to resolve volume objects with stiff hulls. The mechanical coupling is perfomed using position constraints specific to the behavior of the stiff hull. Harmon et al [Harmon and Zorin, 2013] enrich a space of modal deformations (see Barbic et al [Barbič and James, 2005]) with analytically defined detail functions (for a point force applied to an elastic half-space) to increase the expressivity of the model. These methods are very much in line with the spirit of our work but are, again, limited to particular instances of MHMMs (rigid modes and deformable superquadrics, poking functions adding details over modal models). Finally, the Eulerian-on-Lagrangian method [Fan et al., 2013] allows the coupling of a fine scale Eulerian simulation to any coarse scale Lagrangian simulation. The method is general but limited to Eulerian-Lagrangian coupling. Additionally the Eulerian simulation must cover the entire simulation domain meaning that detail cannot be added locally thus negating any potential performance gains.

4.3 EMBEDDINGS

This section provides background on embeddings, introduces notations and motivates our approach. Embeddings are used to synchronize different models of the same object. Popular embeddings include rigid, FEM and affine blendings. The embedded DOFs can be 3D points as well as differential values such as deformation gradients used to compute deformation forces. More generally, any mapping from a set of DOFs to another, such as vibration modes to local strains, can be seen as a generalized as an embedding. Let us consider a set of material points, with $\mathbf{X}$ the vector of all their material coordinates, constant over time. As the state vector of the object, $\mathbf{q}$ (containing the displacements of the master DOFs from their initial coordinates),

(a) Discretization **(b)** Kinematic dependencies

FIGURE 4.2 – *Structure of a traditional model. Control nodes (here, moving frames), control surface vertices (empty circles) and volume sampling points (crosses). Contact forces are applied to surface points (filled circles) controlled by the surface vertices. (4.2a) : Discretization with control nodes and sampling points. (4.2b) : Kinematic dependencies.*

changes over time t, so do the displacements of the embedded, or slave, points, $\mathbf{u}_e$. The mapping relation writes :

$$\mathbf{u}_e(t) = \mathcal{J}(\mathbf{q}(t), \mathbf{X}) \tag{4.1}$$

For the sake of clarity, we will drop the dependence on t in subsequent notations. Slave DOFs may in turn be the masters of other sets of DOFs, forming a hierarchy with the root as only set of independent DOFs (Fig.4.2). The velocities $\mathbf{v}_e$ at the embedded level are given by :

$$\mathbf{v}_e = \mathbf{J}\dot{\mathbf{q}} \tag{4.2}$$

where $\mathbf{J} = \frac{\partial \mathcal{J}}{\partial q}$ is the Jacobian matrix of the mapping. Note that positions and velocities are only propagated top-down, from the master to the slave DOFs. The Jacobian matrix is generally rectangular, and so mapping the velocities in the opposite direction requires solving an inverse kinematics problem, which generally has no unique solution, if any. Conversely, the forces and impulses are only propagated bottom-up, as shown in the following. Let $\mathbf{f}_e$ be forces at the embedded level, and $\mathbf{f}_q$ the corresponding forces at the master level. The Principle of Virtual Work states that the power of the forces must be the same at the two levels : $\mathbf{v}_e^T \mathbf{f}_e = \dot{\mathbf{q}}^T \mathbf{f}_q$, for any value of $\mathbf{v}_e$. This, combined with Eq.4.2, implies that

$$\mathbf{f}_q = \mathbf{J}^T \mathbf{f}_e. \tag{4.3}$$

Mass and stiffness matrices can be transferred bottom-up. For instance, if the inertia of the object is defined as a matrix $\mathbf{M}_e$, the equivalent matrix at the top level is $\mathbf{M}_q = \mathbf{J}^T \mathbf{M}_e \mathbf{J}$. While the complete derivation of all the properties of embeddings is out of the scope of this paper, we note that the above relations between forces and displacements at different levels of the kinematic hierarchy hold for any set of generalized coordinates and forces.

Consider the following example as can be seen Figure 4.4 for the sake of clarity on embeddings, where the master levels are points denoted as x_{ci}, while the embedding level is constituted of one point denoted as x_e.

Notice that instead of a point as embedding level, one could have choosen any type depending on the master layers, like deformation gradient or any other measure depending on these levels. In practice, we will only use points for surface detections as well as deformation gradients to derivate material laws as embeddings.

On this simple example the position of the embedding level may be written as follows :

$$x_e = \Sigma_{i=1}^{3} \alpha_i x_{ci}$$

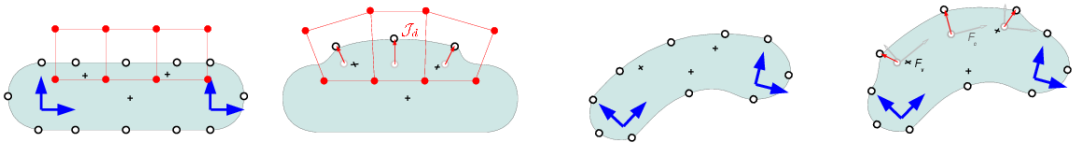

(a) Rest state **(b)** FEM deformation only **(c)** Frame-based deformation only **(d)** Combined deformations

FIGURE 4.3 – *Example of a two-level MHMM, using a frame-based coarse model (blue) and an FEM detail model (red). The detail displacements $\mathcal{J}_d$ (4.3b) are applied in local frames defined by the deformation gradients $\mathcal{F}_c$ of the coarse displacements (4.3c) to generate the combined deformations (4.3d).*

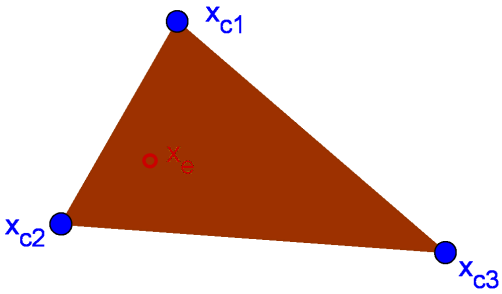

FIGURE 4.4 – *simple embedding example*

where the α_i stands for the barycentric coordinates of the embedding point with respect to the master points for instance. Here the derivation of the jacobian matrix of the mapping is straightforward :

$$v_e = \Sigma_{i=1}^{3} \alpha_i v_{ci} = \mathbf{J} v_c$$

where v_c is the vector of master points velocities : $v_c = \begin{pmatrix} v_{c1} \\ v_{c2} \\ v_{c3} \end{pmatrix}$ and $\mathbf{J}$ stands for a matrix which takes the following form :

$$\mathbf{J} = \begin{pmatrix} \alpha_1 & 0 & 0 & \alpha_2 & 0 & 0 & \alpha_3 & 0 & 0 \\ 0 & \alpha_1 & 0 & 0 & \alpha_2 & 0 & 0 & \alpha_3 & 0 \\ 0 & 0 & \alpha_1 & 0 & 0 & \alpha_2 & 0 & 0 & \alpha_3 \end{pmatrix}$$

Then, the positions and velocities are moving from the master layers to the slave (or embedding) level, while the forces are transfered bottom-up as follow :

$$f_c = \mathbf{J}^T f_e$$

4.4 HIERARCHIES OF EMBEDDINGS

4.4.1 Principle

We propose to set up embedding hierarchies, where embeddings are used to add detail to coarser displacements created by other embeddings, not to be confused with DOF hierarchies

introduced in the previous section. In this section we study the two-level case, as illustrated in Fig.4.3. While the simple sum of embeddings $\mathbf{u}_e(t) = \mathcal{J}_1(\mathbf{q}_1(t), \mathbf{X}) + \mathcal{J}_2(\mathbf{q}_2(t), \mathbf{X})$ may be an option for small displacements, its uncorrelated terms result in unacceptable artifacts as soon as large deformations or rotations occur. The obvious idea is to generalize Eq.4.1 by using the second embedding to change the material coordinates used by the first :

$$\mathbf{u}_e = \mathcal{J}_c(\mathbf{q}_c, \mathbf{X} + \mathcal{J}_d(\mathbf{q}_d, \mathbf{X})) \tag{4.4}$$

where $\mathcal{J}_c(\mathbf{q}_c, \mathbf{X})$ is a coarse displacement field and $\mathcal{J}_d(\mathbf{q}_d, \mathbf{X})$ is a finer model used to add detail, as if a deformable object was embedded in the coarse model. In this approach, the detail changes the material coordinates used in the coarse model. The corresponding hierarchy of embeddings is illustrated horizontally using the dotted arrow in Fig.4.5a, while the DOF hierarchy is illustrated vertically using the plain arrows. Note that the two models of the embedding hierarchy, coarse (c) and detail (d), contain independent DOFs. We say that they compose the *master layer* of the DOF hierarchy.

Combining embeddings using Eq.4.4 may require intense computations at each time step to update the coarse embedding based on the modified material coordinates, and may even introduce discontinuities when an embedded point moves from one cell of a mesh-based coarse model to another. To alleviate this problem, we propose to express the detail motion in a local frame associated with each embedded point. This is essentially a first-order expansion of Eq.4.4 :

$$\mathbf{u}_e = \mathcal{J}_c(\mathbf{q}_c, \mathbf{X}) + \mathcal{F}_c\mathcal{J}_d(\mathbf{q}_d, \mathbf{X}) \tag{4.5}$$

where $\mathcal{F}_c$ is a block-diagonal matrix. For each embedded point i, the diagonal block represents the deformation gradient $\mathcal{F}_c^i = \frac{\partial \mathcal{J}_c^i}{\partial X^i} + \mathbf{I}$ of the coarse displacement at embedded point i. This non-orthonormal basis represents the rotation and deformation created by the coarse displacement, in which the detail displacement is applied, as illustrated by the example in Fig.4.3. Following Eq.4.2, the embedded velocity can be expressed as :

$$\mathbf{v}_e = \mathbf{J}\dot{\mathbf{q}} = \begin{bmatrix} \mathbf{J}_c & \mathbf{J}_d \end{bmatrix} \begin{bmatrix} \dot{\mathbf{q}}_c \\ \dot{\mathbf{q}}_d \end{bmatrix} \tag{4.6}$$

where the Jacobian is a sparse matrix with only two non-null blocks per embedded point : $J_c^i = [\frac{\partial \mathcal{J}_c^i}{\partial \mathbf{q}_c} + \frac{\partial \mathcal{F}_c^i}{\partial \mathbf{q}_c}\mathcal{J}_d^i]$, and $J_d^i = [\mathcal{F}_c^i \frac{\partial \mathcal{J}_d^i}{\partial \mathbf{q}_d}]$ for the coarse and detail models, respectively. However, it is easy to see that straightforwardly combining arbitrary embeddings using this method is not physically correct. Naïvely propagating a force from the embedded layer to both the coarse and detail layers (Eq.4.3) results in its duplication. Therefore, a partition of unity is necessary to retain physical consistency.

Similar issues arise when dealing with other intrinsic object properties. Properties such as mass and stiffness are defined independently of the kinematic discretization either analytically or on a fine voxel map. These properties are sampled using embedded particles, as illustrated in Fig.4.5a. A given mass matrix $\mathbf{M}_e$ at the embedded level is not directly exploitable in Newton's law $\mathbf{f} = \mathbf{Ma}$, since the latter is only valid for independent DOFs, which requires us to cast the mass matrix at this level. Using the Jacobian of Eq.4.6, the equivalent mass matrix at parent level would be :

$$\mathbf{M} = \mathbf{J}^T\mathbf{M}_e\mathbf{J} = \begin{bmatrix} \mathbf{J}_c^T\mathbf{M}_e\mathbf{J}_c & \mathbf{J}_c^T\mathbf{M}_e\mathbf{J}_d \\ \mathbf{J}_d^T\mathbf{M}_e\mathbf{J}_c & \mathbf{J}_d^T\mathbf{M}_e\mathbf{J}_d \end{bmatrix} \tag{4.7}$$

As noticed by [Fan et al., 2013], while the diagonal blocks are PSD, this mass matrix is generally singular, due to the off-diagonal coupling blocks. This happens in case of redundancies

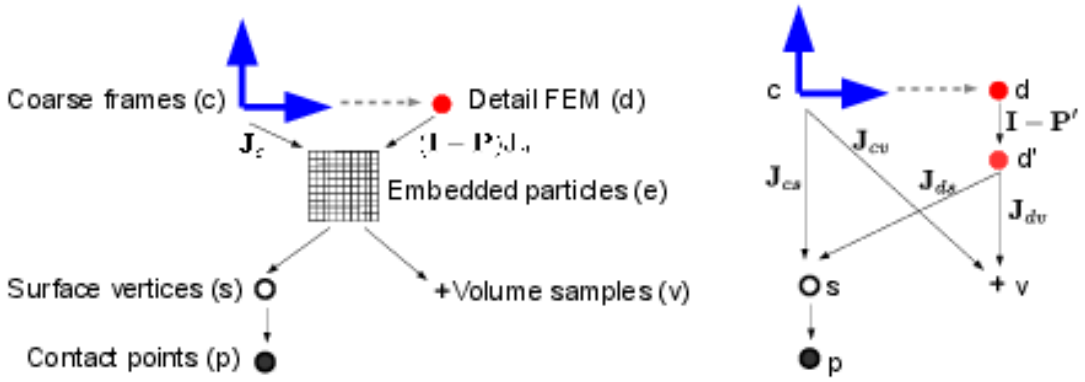

(a) Basic **(b)** Optimized

FIGURE 4.5 – *Structure of the two-level MHMM shown in Fig.4.3.*

between the coarse and detail embeddings. For instance, if the coarse field is a rigid displacement and the detail is an FEM mesh, then a translation of the embedded object can be obtained using a translation of the frame as well as a uniform displacement of the FEM nodes. To alleviate the singularity, they use a least-squares approach to transfer fine scale Eulerian displacements onto a coarse Lagrangian discretization. In contrast to this, we propose a more physically-based approach, using the mass matrix, as explained in the next section.

4.4.2 Kinetic Filtering

We propose a mass-orthogonal decomposition of the hierarchical embedding into coarse and detail fields. We attempt to find the corresponding generalized velocities at the coarse level, $\dot{\mathbf{q}}_c$, that best match $\mathbf{v}_e$, the velocity at the embedded level. This can be done by solving a mass-weighted least squares problem, the solution of which yields $\dot{\mathbf{q}}_c = \mathbf{M}_c^{-1}\mathbf{J}_c^T\mathbf{M}_e\mathbf{v}_e$, where $\mathbf{M}_c = \mathbf{J}_c^T\mathbf{M}_e\mathbf{J}_c$. Note that, if one takes $\mathbf{M}_e$ to be a multiple of identity, this reduces to the classical pseudo inverse solution to a system of equations. Now we can define $\mathbf{v}'_e$ the embedded velocity captured by $\dot{\mathbf{q}}_c$ as

$$\mathbf{v}'_e = \mathbf{P}\mathbf{v}_e \tag{4.8}$$

$$\mathbf{P} = \mathbf{J}_c\mathbf{M}_c^{-1}\mathbf{J}_c^T\mathbf{M}_e. \tag{4.9}$$

We can also define the complementary operator $\bar{\mathbf{P}} = \mathbf{I} - \mathbf{P}$. It is straightforward to see that $\mathbf{M}_e\bar{\mathbf{P}}\mathbf{v}_e$ yields an embedded momentum in the nullspace of $\mathbf{J}_c^T$. Thus using $\bar{\mathbf{P}}$ as our kinetic filter enforces mass-orthogonality between the coarse and detail levels.

Concretely, we define the filtered Jacobian as

$$\mathbf{J} = \begin{bmatrix} \mathbf{J}_c & \bar{\mathbf{P}}\mathbf{J}_d \end{bmatrix} \tag{4.10}$$

and consequently the momentum computed by the off-diagonal blocks of the generalized mass matrix for an arbitrary detail velocity $\dot{\mathbf{q}}_d^*$ is

$$\mathbf{J}_c^T\mathbf{M}_e\bar{\mathbf{P}}\mathbf{J}_d\dot{q}_d^* = \mathbf{J}_c^T\mathbf{p}_e^* = \mathbf{0}. \tag{4.11}$$

Because $\dot{\mathbf{q}}_d^*$ was chosen arbitrarily, this is equivalent to the off-diagonal mass matrix block being $\mathbf{0}$.

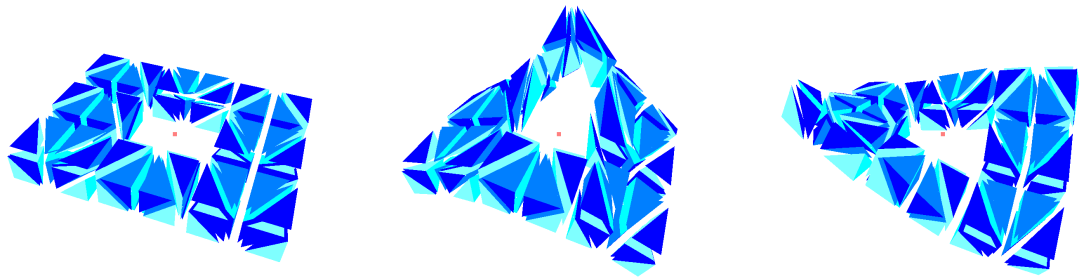

FIGURE 4.6 – *Filtered detail motion. Left : rest shape. Middle, right : detail deformations generated by external forces.*

The resulting form of Newton's equation is :

$$\begin{bmatrix} \mathbf{J}_c^T \mathbf{M}_e \mathbf{J}_c & \\ & \mathbf{J}_d^T \bar{\mathbf{P}}^T \mathbf{M}_e \bar{\mathbf{P}} \mathbf{J}_d \end{bmatrix} \begin{bmatrix} \mathbf{a}_c \\ \mathbf{a}_d \end{bmatrix} = \begin{bmatrix} \mathbf{J}_c^T \mathbf{f}_e \\ \mathbf{J}_d^T \bar{\mathbf{P}}^T \mathbf{f}_e \end{bmatrix} \tag{4.12}$$

The upper-left block is PSD provided that $\mathbf{M}_e$ is symmetric and $\mathbf{J}_c$ is not rank-deficient. While the lower-right block is singular due to the filter, it can be solved using a Filtered Conjugate Method [Ascher and Boxerman, 2003].

An example of tetrahedral FEM detail combined with a rigid coarse motion is shown in Fig.4.6. The rigid frame is fixed for illustration purposes, so that only detail deformations are shown. An external force applied to a single point creates deformations. The force is split by the transposed Jacobian, and the FEM model gets a force distribution which can only generate null linear and angular momenta. It can thus generate any displacement but a rigid one. Notice that there is no fixed point in our detail model. Contrary to previous approaches, the connection between the two models is made by the filtered Jacobian, not by attachment points. This allows us to straightforwardly combine linear modal deformations modes as detail on top of rigid motion, as shown in Section 4.7.2, to avoid the computation of nonlinear deformation modes.

4.4.3 Forces

Our framework is compatible with all the usual material laws and contact behaviors. In the simple approach illustrated in Fig.4.5a, the surface layer s, as well as the deformation energy integration samples (Gauss points in layer v), are embedded in layer e using interpolation. Embedding deformation gradients in layer v allows us to implement all the standard strain measures (such as corotational and Green-Lagrange), and associated constitutive laws (such as Hookean or hyperelastic). The associated generalized forces are stresses, which are propagated as forces to layer e, which also collects the contact forces mapped from p through s. These forces are split between coarse and detail forces as explained in Section 4.4.2. However, layer e typically contains a large number of particles, since the density must be finer than the detail layer d, at least in the range of the detail deformation. Matrix $\mathbf{P}$, used by the kinetic filter, is dense and is of dimension of the number of particles in the embedded layer. This may result in large computation times. One potential solution would be to use a sparse sampling in layer e. However, each sample of layers s and v typically 4 non-coplanar parent points in e. Since the sampling may be irregular, especially in layer s, it is also difficult to accurately model the mass distribution of the object using sparse sampling. This issue is addressed in the next section.

4.5 OPTIMIZED HIERARCHIES

4.5.1 Pre-computed filter at the master layer

To reduce the computation time without modifying the sampling scheme, we present an optimization to by-pass the embedded layer e completely, thus directly connecting v and s to the master layer c-d. Each point in layers s and v has material coordinates and can thus be directly embedded by c-d.

For layer v, we compute deformation gradients $\mathcal{F}_v$ by spatially differentiating the embedding of Eq.4.5 with respect to the material coordinates of the sampling points :

$$\mathcal{F}_v = \mathcal{F}_c \mathcal{F}_d \tag{4.13}$$

This corresponds to the composition of the coarse and detail deformation gradients as shown in Fig.4.3. The stresses $\mathbf{f}_v$ are computed using the deformation gradients and the local material constitutive law, and integrated in space using standard cubature. Stresses could be directly mapped up as forces on layers c and d based on the transposed Jacobian matrix (Eq.4.3). However, the question is how to filter the Jacobian of this embedding, to avoid "double counting" stresses while converting them to forces at the master level.

Let $\mathbf{J}_{cv}$ be the Jacobian of the embedding of deformation gradients in the coarse model, and $\mathbf{J}_{dv}$ be the *unfiltered* Jacobian in the detail model, obtained by differentiation of Eq.4.13 with respect to the coordinates of the DOFs. We convert stresses to filtered forces in the following way :

$$\mathbf{f}_d = \mathbf{J}_d^T \bar{\mathbf{P}}^T \mathbf{M}_e [\mathbf{J}_c \mathbf{M}_c^{-1} \mathbf{J}_{cv}^T + \bar{\mathbf{P}} \mathbf{J}_d \mathbf{M}_d^{-1} \mathbf{J}_{dv}^T] \mathbf{f}_v \tag{4.14}$$

The above equation transforms the force $\mathbf{f}_v$ from v to d using the following steps (right-to-left) :

1. Transform forces from v to c and d using $\mathbf{J}_{cv}^T$ and $\mathbf{J}_{dv}^T$
2. Convert forces at d and c to accelerations using $\mathbf{M}_d^{-1}$ and $\mathbf{M}_c^{-1}$
3. Sum contributions to the corresponding embedded accelerations using $\mathbf{J}_c$ and $\mathbf{J}_d$
4. Compute the force at the embedded level using $\mathbf{M}_e$
5. Split the force on the master layer using kinetic filtering

By re-arranging the above equation using Eq.4.9, we get :

$$\mathbf{f}_d = (\mathbf{I} - \mathbf{P'}^T) \mathbf{J}_{dv}^T \mathbf{f}_v \tag{4.15}$$

$$\mathbf{P'} = \mathbf{M}_d^{-1} \mathbf{J}_d^T \mathbf{M}_e \mathbf{P} \mathbf{J}_d \tag{4.16}$$

$$\mathbf{J'} = \begin{bmatrix} \mathbf{J}_{cv} & \mathbf{J}_{dv}(\mathbf{I} - \mathbf{P'}) \end{bmatrix} \tag{4.17}$$

The square matrix $(\mathbf{I} - \mathbf{P'}^T)$ acts as a filter on the detail forces, while its transpose acts as a filter on the detail velocities. Filtering is thus moved to the detail side, which is smaller thus faster. Moreover, since the above formulation holds for any other slave layers such as s, it can be applied once to the force on d and then accumulated bottom up, as illustrated using d' in Fig.4.5b. In our implementation we precompute this filter at initialization. Theoretically, not updating the filter may give rise to artifacts such as the injection of coarse motion into the detail level. Such errors could be fixed by constraining the edges of the detail level to ensure continuity in the displacement, however, in our experiments, such artifacts were not observed.

4.5.2 Implementation Details

In this section we review some relevant implementation details as well as expound upon important optimizations that can be applied to MHMMs.

At initialization time, we first organize the model based on the property map of the object, as illustrated in Fig.4.5a. Computing the mass $\mathbf{M}_e$ at the embedded level and storing it as a constant in the master layer is a reasonable and efficient approximation. Based on the stiffness distribution and the embedding, we compute the volume samples of layer v. We then set up the direct embeddings and remove the embedded layer e as explained in Section 4.5.1 and illustrated in Fig.4.5b. Since gravity generates translational forces, its contribution to the detail is null when translation is kinematically feasible by the coarse model. In this case, we apply it directly at the coarse level. Otherwise, it is possible to split the weight across volume sampling points.

In general, the Jacobians change over time and must be updated at each step of the simulation, and the filters as well. However, many popular blendings such a linear FEM, linear modes, or affine frame-based blendings have constant Jacobians, and result in constant $\partial\mathcal{J}_c/\partial\mathbf{q}_c$ or $\partial\mathcal{J}_d/\partial\mathbf{q}_d$ matrices which allow us to save computation time.

Assuming that the fine displacement of the detail $\mathcal{J}_d$ is small, the coarse Jacobian matrix $\mathbf{J}_c$ and filter $\mathbf{P}$ can be considered constant. When the coarse displacement is large, the change of local frames $\mathcal{F}_c$ in Eq.4.5 requires updates of $\mathbf{J}_d$.

4.6 EXTENSIONS

4.6.1 Decoupled implicit integration

Time integration of MHMMs involves updating both velocity and positional DOFs at the master level in response to forces and constraints expressed at the embedded levels. After integration, positions and velocities at the embedded level can be updated using the embedding and the associated Jacobians. As usual, boundary conditions can be applied to the embedded levels using soft constraints or Lagrange Multipliers. In the case of stiff deformable models, very small time steps may be required for stable explicit integration, and it may be more efficient to apply more stable integration, such as the popular semi-implicit backward Euler method :

$$\left(\mathbf{M} - h^2\mathbf{K}\right) a = f + h\mathbf{K}\mathbf{v} \tag{4.18}$$

where $\mathbf{K} = \frac{\partial f}{\partial q}$ is the stiffness matrix, and h is the time step. Given the mass matrix $\mathbf{M}_e$ at the embedded level, the mass matrix at the master level is computed as explained in Section 4.4.2 using the filtered Jacobian of Eq.4.10. We do not assemble the stiffness matrix at the master level, since we use a Conjugate Gradient solver and propagations to compute the matrix-vector products. Let $\mathbf{H} = \left(\mathbf{M} - h^2\mathbf{K}\right)$ be the integration matrix. The filtering method to cancel the off-diagonal blocks of the mass matrix presented in Section 4.4.2 can straightforwardly be extended to this matrix by replacing the projection $\mathbf{P}$ of Eq.4.8 with :

$$\mathbf{v}'' = \mathbf{S}\mathbf{v} = \mathbf{J}_c\mathbf{H}_c^{-1}\mathbf{J}_c^T\mathbf{H}_e\mathbf{v}, \tag{4.19}$$

Equation 4.18 becomes :

$$\begin{bmatrix} \mathbf{J}_c^T\mathbf{H}_e\mathbf{J}_c & \\ & \mathbf{J}_d^T(\mathbf{I}-\mathbf{S}^T)\mathbf{H}_e(\mathbf{I}-\mathbf{S})\mathbf{J}_d \end{bmatrix} \begin{bmatrix} \mathbf{a}_c \\ \mathbf{a}_d \end{bmatrix} = \begin{bmatrix} \mathbf{J}_c^T(\mathbf{f}_e + h\mathbf{K}_e\mathbf{v}) \\ \mathbf{J}_d^T(\mathbf{I}-\mathbf{S}^T)(\mathbf{f}_e + h\mathbf{K}_e\mathbf{v}) \end{bmatrix} \tag{4.20}$$

This results in two systems coupled only through the right-hand term. These can be solved independently, possibly using specialized solvers or in parallel. An example is shown in Section 4.7.4 where the rigid dynamics is handled by a generic solver while the modal model is handled using a specialized one.

4.6.2 Pre-factorized detail systems

In MHMMs, detail motions are expressed in local frames relative to the coarse motion. The nature of the detail motion is that it is high-frequency, typically with lower amplitude - thus we can apply small deformation simplifications. When coupled with systems that can be pre-factorized, exploiting small strain can lead to computational gains. Examples of such systems include linear tetrahedral finite elements with small-strain, linear constitutive models (Figure 4.8), and linear modal simulations (Figure 4.11).

Due to the the constant nature of the pre-factorization, we lose the ability to interact implicitly with the detail model ; the interaction is necessarily explicit (i.e. ; only external forces are taken into account on the right hand side of the system, not the interaction stiffness). Note that the interaction with the coarse model can remain implicit.

However, this optimization can also be applied to non-constant systems albeit by using a more general formulation. Aggressive accelerations can be obtained by preconditionning the detail solver with a full pre-factorization of the system computed at initialization time (see Figure 4.9) : Performance improvements of up to 50% have been observed in our experiments. This greatly reduces the cost of adding extra detail to *any* simulation.

4.6.3 N-levels hierarchies

Kinetic filtering can be straightforwardly extended to handle more than two levels in the hierarchy. Let $\mathbf{q}_i$, $\mathcal{J}_i(t)(\mathbf{q}_i, \mathbf{X})$ and $\mathcal{F}_{i-1} = \frac{\partial \mathcal{J}_{i-1}}{\partial \mathbf{X}_{i-1}}$ respectively the coordinates of the DOFs, the detail and the local frame at level i. Each detail layer is applied in the parent frame, so that for N levels, we get :

$$\begin{aligned} \mathbf{u}_e &= \mathcal{J}_1 + \mathcal{F}_1\mathcal{J}_2 + \mathcal{F}_1\mathcal{F}_2\mathcal{J}_3 + \dots \\ &= \mathcal{J}_1 + \textstyle\sum_{k=2}^{N}(\prod_{j=1}^{k-1}\mathcal{F}_j)\mathcal{J}_k \end{aligned} \tag{4.21}$$

The corresponding Jacobian is :

$$\mathbf{J} = \begin{bmatrix}\mathbf{J}_1 & \dots & \bar{\mathbf{P}}_{i-1}\mathbf{J}_i & \dots\end{bmatrix} \tag{4.22}$$

$$\bar{\mathbf{P}}_0 = \mathbf{I},\ \bar{\mathbf{P}}_i = \bar{\mathbf{P}}_{i-1}.(\mathbf{I} - \mathbf{P}_i) \tag{4.23}$$

$$\mathbf{P}_i = \bar{\mathbf{P}}_{i-1}\mathbf{J}_i\mathbf{M}_{ii}^{-1}\mathbf{J}_i^T\bar{\mathbf{P}}_{i-1}^T\mathbf{M}_e\bar{\mathbf{P}}_{i-1} \tag{4.24}$$

$$\mathbf{M}_{ii} = \mathbf{J}_i^T\bar{\mathbf{P}}_{i-1}^T\mathbf{M}_e\bar{\mathbf{P}}_{i-1}\mathbf{J}_i \tag{4.25}$$

This formulation achieves the decoupling since off-diagonal blocks of the mass matrix are null (see proof in Appendix 4.9).

4.7 RESULTS

In this section, we exhibit the versatility of our approach using different combinations of deformation models (2d/3d finite elements, rigid, frame-based, modal subspace).

4.7.1 Validation

To validate the precision of our method, we have compared two simulations of a beam in extension, for which analytical results are well known. We used a fine FEM grid on top of two coarse hexahedra. The relative displacement error is less than 0.1%. The three-point bending of the same models leads to a maximum relative difference of less than 20% with respect to the fine FEM displacement. Qualitatively the simulations are indistinguishable (Fig.4.7).

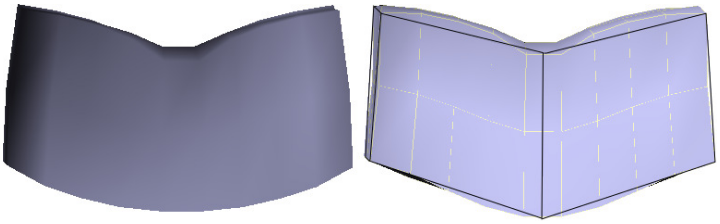

FIGURE 4.7 – *Comparison on flexion. Left : standard FEM. Right : MHMM with coarse FEM + detail*

In the accompanying video, the simulation of a cantilever beam in contact shows that MHMM simulations (both optimized and non-optimized solutions) closely match high resolution FEM simulations.

4.7.2 FEM on a rigid frame

Detail motion can be applied to the whole object, as shown in Fig.4.8. Here, a rigid model is enriched with tetrahedra FEM (red edges on Fig.4.8-left), covering the entire object. Note that there is no attach point between the rigid and the FEM models.

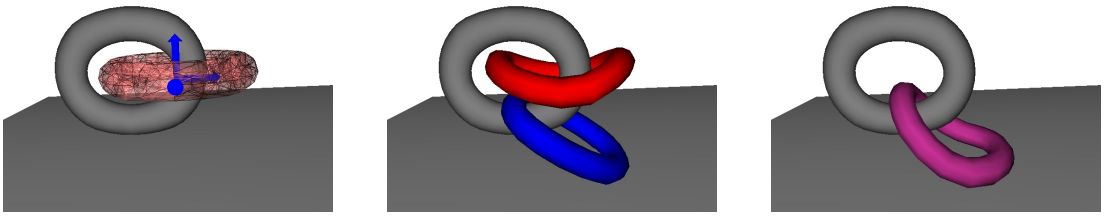

FIGURE 4.8 – *Rigid frame (blue) + global FEM (red). Left : initial position. Middle : simulated models shown separately. Right : Combined result. Grey objects are fixed colliders.*

Figure 4.9 shows an example of a local FEM volumetric patch hierarchically attached to a moving frame. This simple simulation, which could also be produced using traditional coupled models, shows that our detail model can undergo large deformations. The detail model is fixed at its boundary with the rest of the object, to enforce the continuity of the displacements.

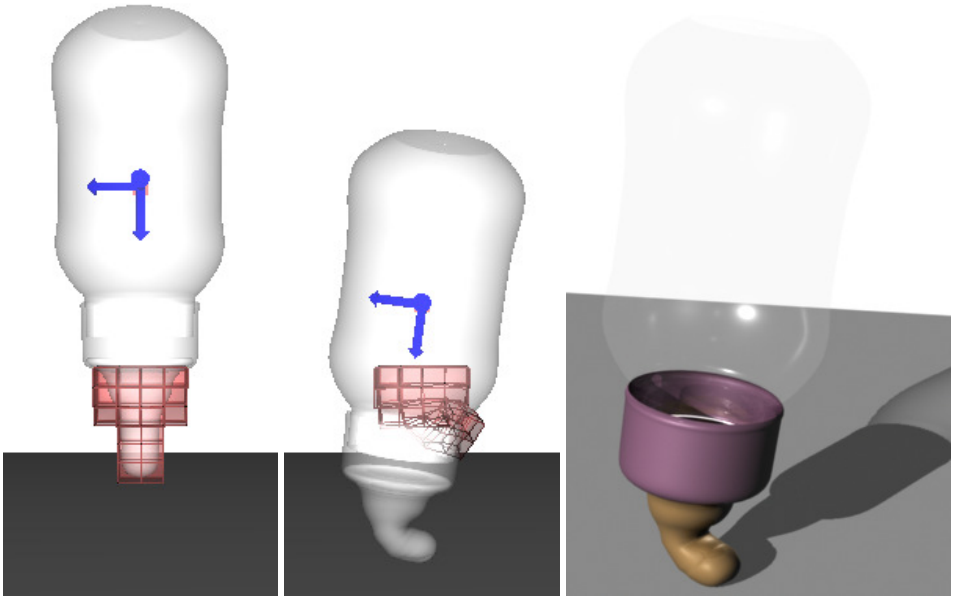

FIGURE 4.9 – *Rigid frame + local FEM : a baby bottle with a deformable soother. The detail level FEM is displayed with its local coordinate system centered on the origin.*

Even for a very stiff material, the weight is correctly simulated in these two examples, because the kinetic filter maps it to the rigid model. This alleviates the well-known gravity artifact in stiff FEM due to the incomplete solutions produced by iterative solvers.

4.7.3 FEM on frame-based deformation models

Our method allows us to easily combine the advantages of several models, as shown in Fig.4.1. The coarse model of the octopus is frame-based [Gilles et al., 2011], which allows the efficient simulation of the global motion using linear blend skinning, while a fine FE mesh would be necessary to simulate all the tentacles independently. Conversely, FEM are more convenient to model local deformations. Using our approach, getting the best of the two models is straightforward because we can embed finely deforming regions in a high-resolution volumetric mesh. We fix the vertices that are on the boundary of the detail mesh and inside the octopus in order to enforce continuity of the displacement field. This is implemented as a simple projective constraint on the detail DOFs (no mechanical coupling with coarse DOfs).

Different cubature schemes can be also combined. Sparse Gauss point sampling such as in [Faure et al., 2011] is performed in the region not covered by the detail, while standard 8-point cubature is applied to each hexahedron. The two non-overlapping sets of integration samples are combined together in layer v as illustrated by green spheres in the figures.

Adding DOFs only where they are needed produces significant gains in computational time as well as a corresponding reduction in memory footprint (Table 4.1). Figure 4.10 shows a similar example with a larger contact area.

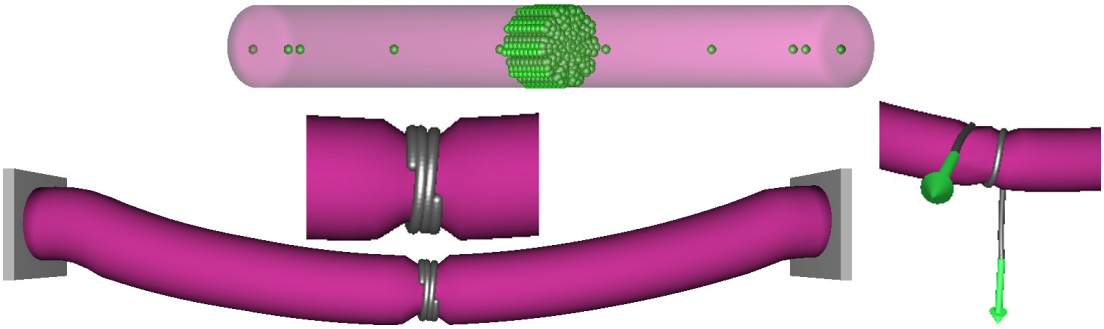

FIGURE 4.10 – *A string strangulates a deformable cylinder (purple). A local tetrahedral FEM patch (red) allows a precise deformation in the contact area while coarse affine frames (blue) simulate the global deformation.*

4.7.4 Non-linear Modal Subspace

Non-linear subspace deformation can be easily and efficiently achieved with our technique by combining a coarse frame-based deformation field and linear subspace deformation modes. Each deformation mode is locally transformed by the blended displacement of the frames. The well known artifacts due to linearity are reduced as the number of frames increases.

Compared to traditional one-level technique, we believe that MHMM allows for a better control of animations. As shown in the accompanying video, the scripted displacement of one of the frame can be automatically enriched with simulated deformations (based on the remaining frames and modal degrees of freedom).

To exhibit particular visual features, a third level can be added. In Figure 4.11, local detailed deformations are achieved using a local FEM patch, while in Fig.4.12, local subspace deformation modes allows for a finer tuning of the deformation degrees of freedom.

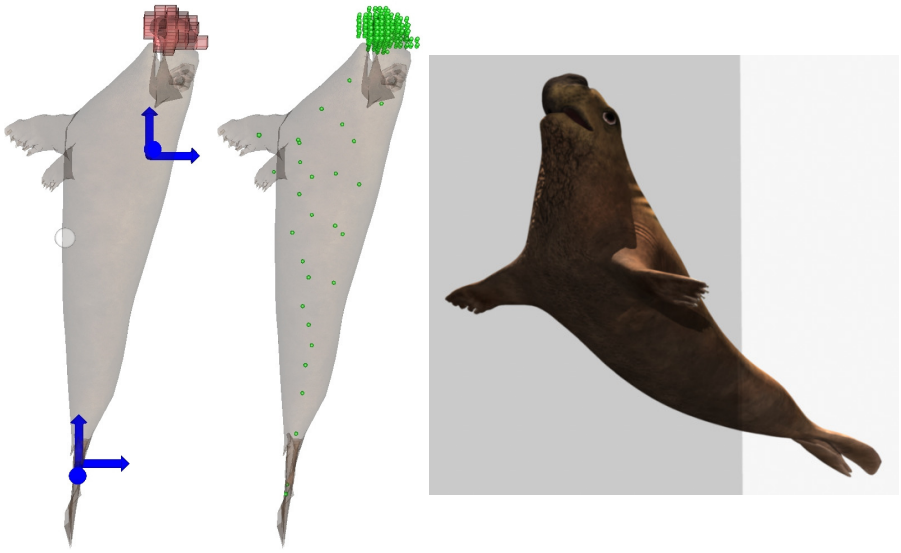

FIGURE 4.11 – *A 3-levels hierarchy combining frame-based, linear modal subspace, and hexahedral finite elements models. Left : Frame and FEM discretization ; Middle : volume samples ; Right : Simulation.*

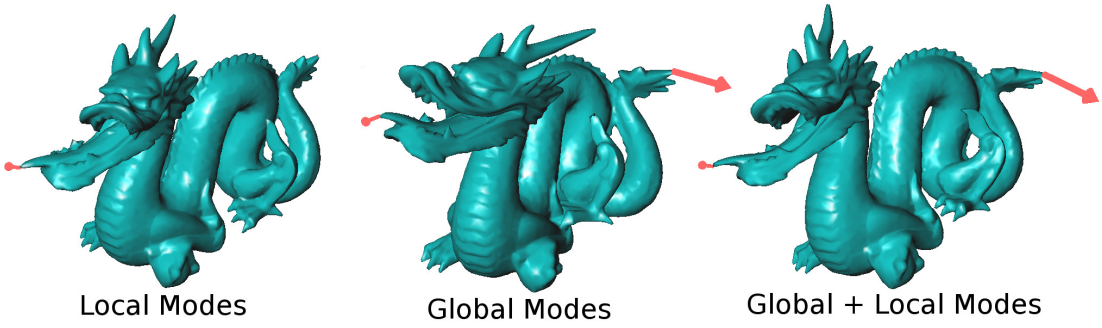

FIGURE 4.12 – *Frame-based, global subspace and local subspace deformation models combined in a 3-level hierarchy.*

4.7.5 Multi-dimensional material

Our approach makes no assumption on the topology of the models, and can mix objects of different dimensions. Figure 4.13 shows a stiff hull combined with a single coarse hexahedron. The coarse FE achieves volume preservation, while the fine surface creates folds. The coupling achieved by the kinetic filter generates the well-known buckling behavior without additional constraints.

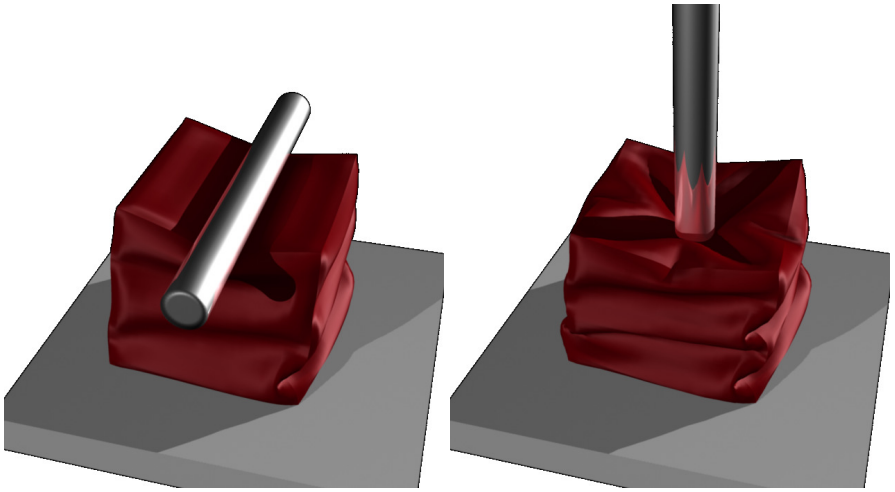

FIGURE 4.13 – *A detailed thin shell embedded in a single coarse hexahedral element.*

In Fig.4.14, we simulate the pinching of a patch of skin with hypoderm using the epiderm as 2D detail on top of a two-material coarse volumetric grid.

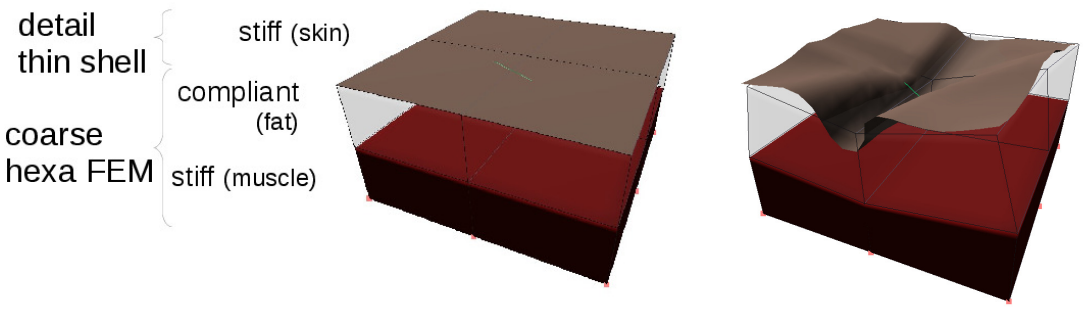

FIGURE 4.14 – *Skin folding simulation using a coarse volumetric FEM mesh (in blue) combined with a thin shell patch and several material properties.*

4.7.6 Artistic control

Our kinetic filter helps ensure that adding new detail levels to a simulation will not affect any underlying gross motion. This is particularly desirable for computer animation. Artists are free to kinematically define character and object motions while additional simulation layers can be added interactively in order to add emergent behavior via physical simulation. This is akin to the layered approach common to many image editing applications, except here we allow the artist to sculpt motion instead. Figure 4.15 shows a 3 level hierarchy applied to an animated character. The coarse motion is prescribed by an artist using standard skinning techniques. The artist has then added a coarse FEM grid to capture the jiggling of the character's belly along with a finer, local grid to add the indent caused by the character's finger. In this case, our method provides an alternative to Rig-Space physics but without the need for complicated tetrahedral meshing of the entire character [Hahn et al., 2012].

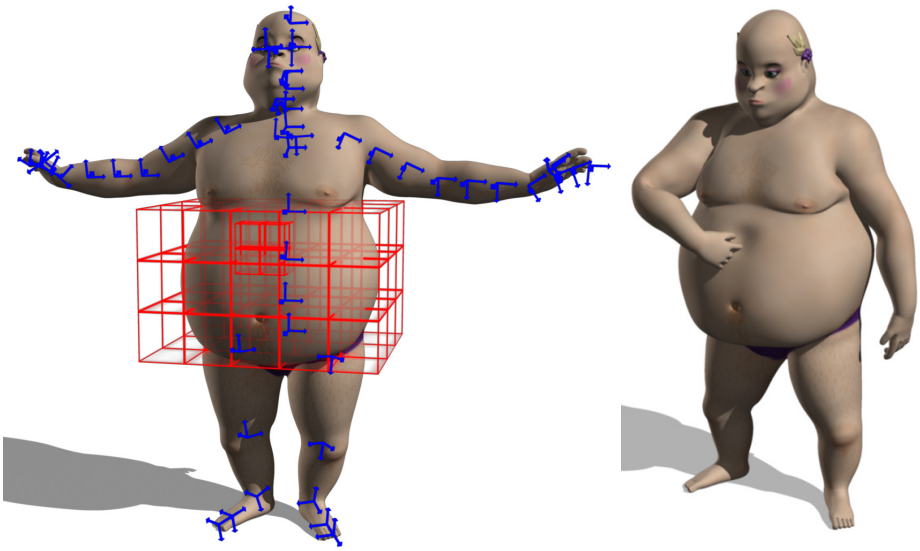

FIGURE 4.15 – *A full body with a coarse rigid motion and three levels of hierarchy easily controlled by an artist.*

4.7.7 Towards adaptivity

As it is possible to precompute different detail models during initialization, some of these regions may be activated or deactivated automatically at runtime following some criteria, for instance the location of contacts for the worm Figure 4.16, where two detail FE regions are defined, while the coarse motion is given by a frame-based model. All the detail models may be deactivated when the magnitude of their motion falls below some given threshold.

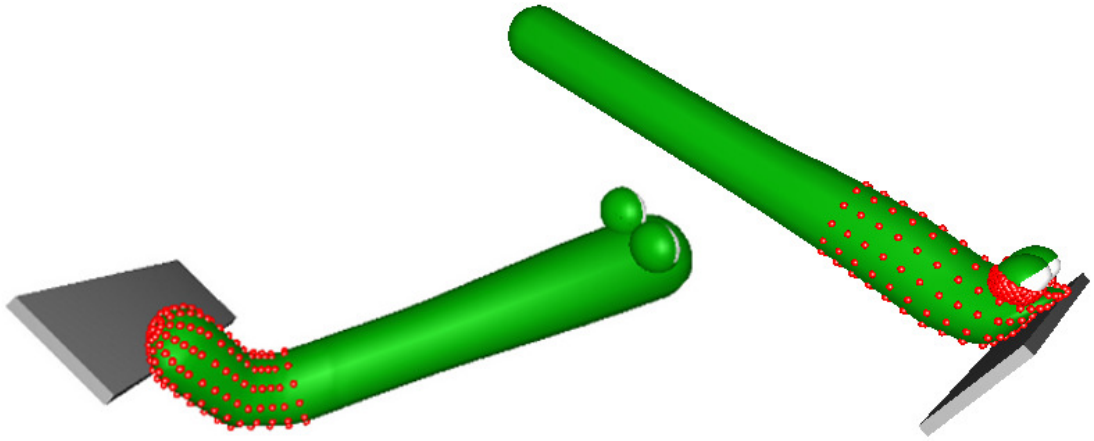

FIGURE 4.16 – *Two detail regions automatically activated or deactivated at runtime.*

Scene	Octopus (Fig.4.1)		
DOFs	10 affine	6878 points	10 affine + 48 points
Integration Points	10	37912	154
Frame Rate (Hz)	60	4	35 (pre-factorized) 25 (full solve)

Scene	Walrus (Fig.4.11)		
DOFs	4566 points	2 rigids + 16 modes	2 rigids + 16 modes + 111 points
Integration Points	26392	50	390
Frame Rate (Hz)	1	100	15 (pre-factorized) 10 (full solve)

Scene	Tourniquet (Fig.4.10)	
DOFs	7500 points	5 affine + 510 points
Integration Points	36450	2440
Frame Rate (Hz)	<0.1	2 (pre-factorized) 2 (full solve)

TABLE 4.1 – *Performances*

4.7.8 Performance

Frame rates for our examples are given in Table 4.1. For a fair comparison, we use the same solvers and contact handling mechanisms for all deformable models. MHMMs achieve large speedups compared to models with uniformly fine resolutions (corresponding to the detail we wish to simulate). As is the case with other techniques, the number of degrees of freedom impacts the performance of our method but, we gain invariance with respect to the spatial dimension of the detail. Therefore, for a given number of degrees of freedom, details at arbitrarily fine scales can be simulated in constant time. Other methods would require extremely dense discretizations, re-meshing or adaptive refinement to accomplish this.

The main bottleneck of MHMMs is potential coupling of all detail DOFs through coarse layer. This results in a dense kinetic filter matrix, which slows down the required matrix products. Pre-factorization mitigates this problem, as the filter is only required to compute the right hand side vector. We suspect that filtering may be accelerated using a multigrid approach, but defer this study to future work.

4.8 CONCLUSION

Multifarious Hierarchical Mechanical Models are a new approach to solid simulation, by hierarchically coupling models using a novel operator, the kinetic filter. We have demonstrated its ability to easily and efficiently combine the advantages of different physical models. The implementation, including all used models, will be distributed in open-source. An obvious avenue for future work is on-the-fly adaptivity without precomputation, by creating or displacing fine models where needed (e.g.,contact areas, regions undergoing large deformations, etc.).

The extension to mixed Lagrangian-Eulerian models for fluid or plastic material simulations is also an interesting perspective.

ACKNOWLEDGEMENTS

Laura Paiardini for her help with models, textures, rendering and video editing. Romain Testylier for his help with the rod simulation.

4.9 OFF-DIAGONAL BLOCKS FOR N-LEVELS

In the expression of an upper off-diagonal block $\mathbf{M}_{ij}$, $i < j$, we split $\bar{\mathbf{P}}_{j-1}$:

$$\begin{aligned}\mathbf{M}_{ij} &= \mathbf{J}_i^T \bar{\mathbf{P}}_{i-1}^T \mathbf{M}_e \bar{\mathbf{P}}_{j-1} \mathbf{J}_j \\ &= \mathbf{J}_i^T \bar{\mathbf{P}}_{i-1}^T \mathbf{M}_e \bar{\mathbf{P}}_{i-1} (\mathbf{I} - \mathbf{P}_i) \left(\prod_{k=i+1}^{j-1} (\mathbf{I} - \mathbf{P}_k) \right) \mathbf{J}_j\end{aligned}$$

The first part of this formula is null, due to the properties of our filters :

$$\begin{aligned}&\mathbf{J}_i^T \bar{\mathbf{P}}_{i-1}^T \mathbf{M}_e \bar{\mathbf{P}}_{i-1} (\mathbf{I} - \mathbf{P}_i) = \\ &\qquad \mathbf{J}_i^T \bar{\mathbf{P}}_{i-1}^T \mathbf{M}_e \bar{\mathbf{P}}_{i-1} - \underbrace{\mathbf{J}_i^T \bar{\mathbf{P}}_{i-1}^T \mathbf{M}_e \bar{\mathbf{P}}_{i-1} \bar{\mathbf{P}}_{i-1} \mathbf{J}_i}_{\mathbf{M}_i} \mathbf{M}_i^{-1} \mathbf{J}_i^T \bar{\mathbf{P}}_{i-1}^T \mathbf{M}_e \bar{\mathbf{P}}_{i-1} \\ &\qquad\qquad\qquad\qquad\qquad\qquad\qquad\qquad\qquad\qquad\qquad\qquad = \mathbf{0}\end{aligned}$$

The property $\bar{\mathbf{P}}_{i-1} \bar{\mathbf{P}}_{i-1} = \bar{\mathbf{P}}_{i-1}$ holds since $\bar{\mathbf{P}}_{i-1}$ is a projection.

CHAPTER

5

GENERAL CONCLUSION

In this work, we have mainly presented **two different physically based models** of plant at the cellular level as well as a **new methodology** to couple a coarse and a more detailed simulation.

Both models were only mechanicaly based, with stretching, bending and pressure. No gene activity was taken into account. Thus plant were modelled from a pure *physical point of view*. As the mechanical properties are at the cross between genetics and plant growth, they are key to analyse plant morphogenesis. In fact, as stated in chapter 1, they are directly influenced by genes and do directly drive growth.

Both models developped allows to take *internal layers* into account, which is crucial in order to understand morphogenesis in plants and which consist in a new approach. Our models were, thus, geometrically and physically realistic, though they didn't take any chemistry nor genetics into account.

The first type of model was designed to *extract mechanical parameters* from global deformation field. As the information contained in this deformation applies to the whole organ considered, it should be sufficient to retrieve the physical caracteristics of the underlying model. To this purpose, we have mixed a physically based simulation to get a static equilibrium, with an optimization algorithm. Each step of optimization calling the balance between inner forces. We have applied this methodology to various plant sub-domains : hypocotyl and roots first due to their shape, and we have tried to adapt it to the meristem. This has lead us to a two dimensional homomgeneous problem of degree zero.

But as we have seen, this type of complex biological structure often leads to ill-posed inverse systems. That is why it is still hard to deduce physical properties from cell displacements. Nevertheless, our method allowed us to statistically set apart different cell wall type, according to the geometry of the organ considered (i.e. surface wall, anticlinal wall of the L1, etc). Then, cell wall stiffness was deduced for each category described. Based on this citerion, we have seen that for embryonic stem as well as for roots, surface and anticlinal wall of the L1 play a different role than inner cell wall, as they seem to be much stiffer by a factor at least three.

Secondly, our local deformation model allowed the study of *Atomic Force Microscopy* on a plant organ. To this purpose, we have developped a geometrically realistic model of plant tissue, as it relied on confocal image, which gives insight in the structure and may provide access to internal layers. We were particularly interested in the meristematic zone, as the meristem is a key organ to analyse morphogenesis. But the framework enabled by our study may be applied to other plant sub-domain. We believe that the comprehensive exploration of the parameter space of A. F. M. will help biologists verifying assumptions and draw conclusions with respect to experiments. For instance different factors influencing the various results have been tested within our framework. But as the results of experiments are often due to a combination of these numerous parameters, it has been a tedious task to extract the precise role of each physical factor on experimental results.

Thus hypothesis and results of experiments may be reread under the light of our model. Whereas this latter is not enough detailed to take thickness into account, it fits well with many biologists assumption, as stated in chapter 3.

Finally we have developped a new approach : the *Multifarious Hierarchy of Mechanical Models* in order to couple a coarse simulation with a more detailed one. This novel method, based on a kinetic filter, which distribute forces, positions and velocities, is a general approach

that allows a motion to be decomposed using a set of arbitrary, overlapping degrees-of-freedom. Simulated objects are simultaneously embedded in several, separately designed deformation models with their own independent degrees of freedom.

The geometry in the overlapping region experiences a hierarchically combined deformation field and this eases modeling since no geometrical operation is required to achieve the coupling. It is faster than full finite element method at the same level of detail. Moreover it is eclectic as it allows to combine arbitrary types of physical models : meshless, modal physics, finite element, etc...

We have demonstrated its ability to easily and efficiently combine the advantages of these different models and this new approach may be of great interest whenever physically based simulation with local detail is required.

However applying this method to a simulated atomic force microscope as described in chapter 3, adresses other issues. Indeed the coarse behavior of the organ modeled, should be equivalent to the one as simulated in this chapter. For instance, choosing a frame based coarse behavior, the meristem should retrieve the same state when undergoing pressure, than the one simulated with full finite elements.

Interesting future study may thus consist in the choice of mechanical parameters for the new methodology proposed in chapter 4, that may accurately represent the behavior of full finite element models. This choice may not be obvious when other force fields like pressure are present in simulation or when the structure described is complex, like the realistic structure of meristem used in chapter 3. This may need the intervention of an optimization algorithm to adequatly choose the mechanical parameters of the coarse model corresponding to the full finite elements method. We could use the optimization loop described Figure 2.2 in chapter 2, where the unknown would be the mechanical caracteristics of the coarse model, and the comparison would be made with the full finite elements simulation.

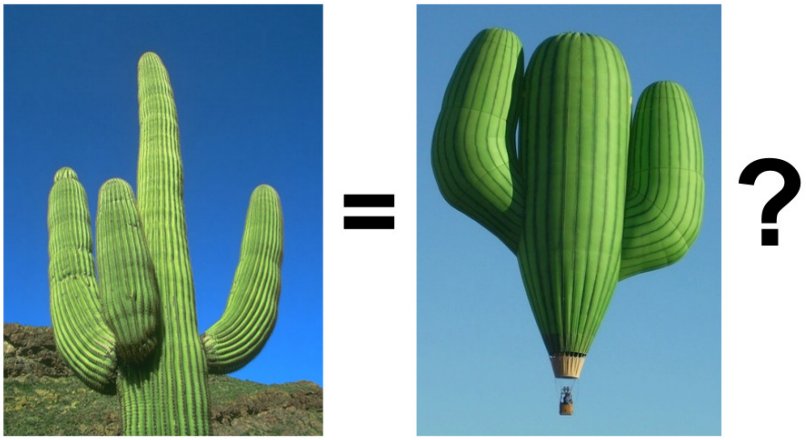

FIGURE 5.1 – *A cactus modelled from a pure physical point of view ?*

An obvious avenue for future work is also the *coupling* between our physically based models of plant cells, and genes activity or chemical reactions. Indeed, the restriction to physics only may help us understand plant mechanical caracteristics, but as genetics and chemistry influence these properties, next interesting analyse may consist in taking them into account.

Since the work of Turing in the early sixties, it is well known that patterning may be the fruit of diffusion reactions of chemical species. However, as stated by [Howard et al., 2011], directed transport and mechanical forces generated by motor proteins can also transmit signals over space to create patterns. A feedback loop may be created between chemistry and mechanical stress to explain patterning and morphogenesis.

For instance, coupling a chemical network as the work of [Yadav et al., 2013] on meristem, to our physical model may help us study this feedback loop which drives plant growth. This should lead to the development of new equations where chemistry interacts deeply with physics and could, then, provide a more complete framework to study morphogenesis.

To conclude, we hope to have provided the community new tools to analyse the physics of plants as well as a new computer graphics method, so that the way to understand morphogenesis is closest now.

REFERENCES

[Arganda-Carreras et al., 2006] Arganda-Carreras, I., Sorzano, C. O. S., Marabini, R., Carazo, J.-M., de Solorzano, C. O., and Kybic, J. (2006). *Consistent and Elastic Registration of Histological Sections using Vector-Spline Regularization*. Lecture Notes in Computer Science, Springer Berlin / Heidelberg, volume 4241/2006, CVAMIA : Computer Vision Approaches to Medical Image Analysis, pages 85-95.

[Ascher and Boxerman, 2003] Ascher, U. M. and Boxerman, E. (2003). On the modified conjugate gradient method in cloth simulation. *The Visual Computer*, 19(7-8).

[Baraff and Witkin, 1998] Baraff, D. and Witkin, A. (1998). Large steps in cloth simulation. In *Proceedings of the 25th annual conference on Computer graphics and interactive techniques (SIGGRAPH)*.

[Barbič and James, 2005] Barbič, J. and James, D. L. (2005). Real-time subspace integration for st. venant-kirchhoff deformable models. In *ACM Transactions on Graphics (Proc. SIGGRAPH)*, volume 24.

[Barbič and Zhao, 2011] Barbič, J. and Zhao, Y. (2011). Real-time large-deformation substructuring. *ACM Trans. Graph.*, 30(4) :91 :1–91 :8.

[Bargel and Neinhuis, 2004] Bargel, H. and Neinhuis, C. (2004). Altered tomato (lycopersicon esculentum mill.) fruit cuticle biomechanics of a pleiotropic non ripening mutant. *Journal of Plant Growth Regulation*, pages 61–75.

[Belytschko et al., 2000] Belytschko, T., Liu, W., and Moran, B. (2000). *Nonlinear finite elements for continua and structures*. Wiley.

[Boudon et al., 2014] Boudon, F., Chopard, J., Ali, O., Gilles, B., Hamant, O., Boudaoud, A., Traas, J., and Godin, C. (2014). A computational framework for 3d mechanical modeling of plant morphogenesis with cellular resolution (under review).

[Boudon et al., 2012] Boudon, F., Pradal, C., Cokelaer, T., Prusinkiewicz, P., and Godin, C. (2012). L-py : an L-system simulation framework for modeling plant architecture development based on a dynamic language. *Front Plant Sci*, 3 :76.

[Brodland et al., 2010] Brodland, G. W., Conte, V., Cranston, P. G., Veldhuis, J., Narasimhan, S., Hutson, M. S., Jacinto, A., Ulrich, F., Baum, B., and Miodownik, M. (2010). Video force

microscopy reveals the mechanics of ventral furrow invagination in drosophila. *Proceedings the National Academy of Science of the United States of America*, (51).

[Byrne and Drasdo, 2009] Byrne, H. and Drasdo, D. (2009). Individual-based and continuum models of growing cell populations : a comparison. *J Math Biol*, 58(4-5) :657–687.

[CHEN and HOGER, 2000] CHEN, Y.-C. and HOGER, A. (2000). Constitutive Functions of Elastic Materials in Finite Growth and Deformation. *Journal of Elasticity*, pages 175–193.

[Chiou et al., 2012] Chiou, K. K., Hufnagel, L., and Shraiman, B. I. (2012). Mechanical stress inference for two dimensional cell arrays. *PLOS Computational Biology*.

[Clausen et al., 2013] Clausen, P., Wicke, M., Shewchuk, J. R., and O'brien, J. F. (2013). Simulating liquids and solid-liquid interactions with lagrangian meshes. *ACM Trans. Graph.*, 32(2) :17 :1–17 :15.

[Coen et al., 2004] Coen, E., Rolland-Lagan, A.-G., Matthews, M., Bangham, J. A., and Prusinkiewicz, P. (2004). The genetics of geometry. *Proceedings National Academy of Sciencs USA*, 101 :4728–35.

[Corson et al., 2009] Corson, F., Hamant, O., Bohn, S., Traas, J., Boudaoud, A., and Couder, Y. (2009). Turning a plant tissue into a living cell froth through isotropic growth. *Proceedings of the National Academy of Sciences of the United States of America*, 106 no. 21 :8453–8458.

[Cranston et al., 2010] Cranston, P. G., Veldhuis, J. H., Narasimhan, S., and Brodland, G. W. (2010). Cinemechanometry (cmm) : A method to determine the forces that drive morphogenetic movements from time-lapse images. *Annals of Biomedical Engineering*, page 2937–2947.

[De Boer et al., 1992] De Boer, M., Fracchia, D., and Prusinkiewicz, P. (1992). *A model for cellular development in morphogenetic fields in : Lindenmayer Systems*. Springer.

[Debunne et al., 1999] Debunne, G., Desbrun, M., Barr, A. H., and Cani, M.-P. (1999). Interactive multiresolution animation of deformable models. In *Eurographics Workshop on Computer Animation and Simulation*, Milan, Italy.

[Douady and Couder,] Douady, S. and Couder, Y. Phyllotaxis as a Dynamical Self Organizing Process.

[Engl et al., 2009] Engl, H. W., Flamm, C., Kügler, P., Lu, J., Müller, S., and Schuster, P. (2009). Inverse problems in systems biology. *Inverse Problems*, page Vol 25.

[Espinosa-Soto et al., 2004] Espinosa-Soto, C., Padilla-Longoria, P., and Alvarez-Buylla, E. R. (2004). A gene regulatory network model for cell-fate determination during Arabidopsis thaliana flower development that is robust and recovers experimental gene expression profiles. *Plant Cell*, 16(11) :2923–2939.

[Faloutsos et al., 1997] Faloutsos, P., van de Panne, M., and Terzopoulos, D. (1997). Dynamic free-form deformations for animation synthesis. *IEEE Transactions on Visualization and Computer Graphics*, 3(3).

[Fan et al., 2013] Fan, Y., Litven, J., Levin, D. I. W., and Pai, D. K. (2013). Eulerian-on-lagrangian simulation. *ACM Transactions on Graphics*, 32(3).

[Faure et al., 2012] Faure, F., Duriez, C., Delingette, H., Allard, J., Gilles, B., Marchesseau, S., Talbot, H., Courtecuisse, H., Bousquet, G., Peterlik, I., and Cotin, S. (2012). SOFA : A Multi-Model Framework for Interactive Physical Simulation. In Payan, Y., editor, *Soft Tissue Biomechanical Modeling for Computer Assisted Surgery*, volume 11 of *Studies in Mechanobiology, Tissue Engineering and Biomaterials*, pages 283–321. Springer.

[Faure et al., 2011] Faure, F., Gilles, B., Bousquet, G., and Pai, D. K. (2011). Sparse Meshless Models of Complex Deformable Solids. In *ACM Transactions on Graphics (Proc. SIGGRAPH)*, volume 30.

[Fernandes et al., 2012] Fernandes, A. N., Chen, X., Scotchford, C. A., Walker, J., Wells, D. M., Roberts, C. J., and Everitt, N. M. (2012). Mechanical properties of epidermal cells of whole living roots of arabidopsis thaliana : An atomic force microscopy study. *Physical Review E*.

[Fernandez et al., 2010] Fernandez, R., Das, P., Mirabet, V., Moscardi, E., Traas, J., Verdeil, J.-L., Malandain, G., and Godin, C. (2010). Imaging plant growth in 4d : robust tissue reconstruction and lineaging at cell resolution. *Nature Methods*, 7 :547–53.

[Fletcher et al., 2014] Fletcher, A. G., Osterfield, M., Baker, R. E., and Shvartsman, S. Y. (2014). Vertex models of epithelial morphogenesis. *Biophysical Journal*, 106(11) :2291 – 2304.

[Geitmann, 2006] Geitmann, A. (2006). Experimental approaches used to quantify physical parameters at cellular and subcellular levels. *American Journal of Botany*, pages 1380–1390.

[Gibson and Ashby, 2001] Gibson, L. J. and Ashby, M. F. (2001). *Cellular solids Structure and Properties*. Cambridge University Press.

[Gilles et al., 2011] Gilles, B., Bousquet, G., Faure, F., and Pai, D. (2011). Frame-based Elastic Models. In *ACM Transactions on Graphics*, volume 30.

[Goriely and Ben Amar, 2007] Goriely, A. and Ben Amar, M. (2007). On the definition and modeling of incremental, cumulative, and continuous growth laws in morphoelasticity. *Biomech Model Mechanobiol*, 6(5) :289–296.

[Graner and Glazier, 1992] Graner, F. and Glazier, J. A. (1992). Simulation of Biological Cell Sorting Using a Two-Dimensional Extended Potts Model. *Physical Review Letters*, (13).

[Green et al., 2010] Green, A. A., Kennaway, J. R., Hanna, A. I., Bangham, J. A., and Coen, E. (2010). Genetic control of organ shape and tissue polarity. *PLoS Biol.*, 8(11).

[Grinspun et al., 2002] Grinspun, E., Krysl, P., and Schröder, P. (2002). Charms : a simple framework for adaptive simulation. In *ACM Transactions on Graphics (Proc. SIGGRAPH)*, volume 21.

[Hahn et al., 2012] Hahn, F., Martin, S., Thomaszewski, B., Sumner, R., Coros, S., and Gross, M. (2012). Rig-space physics. In *ACM Transactions on Graphics (Proc. SIGGRAPH)*, volume 31.

[Hamant, 2013] Hamant, O. (2013). Widespread mechanosensing controls the structure behind the architecture in plants. *Current Opinion in Plant Biology*, 16 :654–660.

[Hansen, 2006] Hansen, N. (2006). *The CMA evolution strategy : a comparing review,*Towards a new evolutionary computation. Advances on estimation of distribution algorithms. Springer.

[Harmon and Zorin, 2013] Harmon, D. and Zorin, D. (2013). Subspace integration with local deformations. *ACM Trans. Graph.*, 32(4) :107 :1–107 :10.

[Hepworth and Vincent, 1998] Hepworth, D. G. and Vincent, J. F. V. (1998). The mechanical properties of xylem tissue from tobacco plants (nicotiana tabacum ‘ samsun ’). *Annals of Botany*, page 751–759.

[Hermanowicz,] Hermanowicz, S. W. A simple 2D biofilm model yields a variety of morphological features.

[Hild and Roux, 2006] Hild, F. and Roux, S. (2006). Digital image correlation : from displacement measurement to identification of elastic properties – a review. *Strain*, pages Vol 42, pages 69–80.

[Honda et al., 2008] Honda, H., Motosugi, N., Nagai, T., Tanemura, M., and Hiiragi, T. (2008). Computer simulation of emerging asymmetry in the mouse blastocyst. *Development*, 135(8) :1407–1414.

[Howard et al., 2011] Howard, J., Grill, S. W., and Bois, J. S. (2011). Turing's next steps : the mechanochemical basis of morphogenesis. *Nature Reviews Molecular Cell Biology*, 12 :392–398.

[Ishihara et al., 2013] Ishihara, S., Sugimura, K., Cox, S. J., Bonnet, I., Bellaiche, Y., and Graner, F. (2013). Comparative study of non-invasive force and stress inference methods in tissue. *the European Physical Journal E*.

[Johnson, 1987] Johnson, K. (1987). *Contact mechanics*. Cambridge University Press.

[Kauffman et al., 2004] Kauffman, S., Peterson, C., Samuelsson, B., and Troein, C. (2004). Genetic networks with canalyzing Boolean rules are always stable. *Proc. Natl. Acad. Sci. U.S.A.*, 101(49) :17102–17107.

[Kennaway et al., 2011] Kennaway, R., Coen, E., Green, A., and Bangham, A. (2011). Generation of diverse biological forms through combinatorial interactions between tissue polarity and growth. *PLoS Comput. Biol.*, 7(6) :e1002071.

[Kerstens et al., 2001] Kerstens, S., Decraemer, W. F., and Verbelen, J.-P. (2001). Cell walls at the plant surface behave mechanically like fiber-reinforced composite materials. *Plant Physiology*, pages 381–385.

[Kierzkowska et al., 2012] Kierzkowska, A.-L. R., Weber, A., Kochova, P., Felekis, D., B.J.Nelson, Kuhlemeier, C., and Smith, R. S. (2012). Cellular force microscopy for in vivo measurements of plant tissue mechanics. *Plant Physiology*.

[Kim and James, 2012] Kim, T. and James, D. L. (2012). Physics-based character skinning using multidomain subspace deformations. *Visualization and Computer Graphics, IEEE Transactions on*, 18(8) :1228–1240.

[Kondo and Miura, 2010] Kondo, S. and Miura, T. (2010). Reaction-diffusion model as a framework for understanding biological pattern formation. *Science*, 329(5999) :1616–1620.

[Landau and Lifchitz, 1970] Landau, L. D. and Lifchitz, E. M. (1970). *Theory of Elasticity*. Pergamon Press.

[Lee et al., 2008] Lee, D., Barber, J. R., and Thouless, M. D. (2008). Indentation of an elastic half space with material properties varying with depth. *International Journal of Engineering Science*, pages 1274–1283.

[Meinhardt, 2008] Meinhardt, H. (2008). Models of biological pattern formation : from elementary steps to the organization of embryonic axes. *Curr. Top. Dev. Biol.*, 81 :1–63.

[Merks et al., 2011] Merks, R. M., Guravage, M., Inze, D., and Beemster, G. T. (2011). VirtualLeaf : an open-source framework for cell-based modeling of plant tissue growth and development. *Plant Physiol.*, 155(2) :656–666.

[Merks and A., 2005] Merks, R. M. H. and A., G. J. (2005). A cell-centered approach to developmental biology. *Physica A*, pages 113–130.

[Milani et al., 2013] Milani, P., Braybrook, S. A., and Boudaoud, A. (2013). Shrinking the hammer : micromechanical approaches to morphogenesis. *Journal of Experimental Botany*.

[Milani et al., 2011] Milani, P., Gholamirad, M., Traas, J., Arneodo, A., Boudaoud, A., Argoul, F., and Hamant, O. (2011). In vivo analysis of local wall stiffness at the shoot apical meristem in arabidopsis using atomic force microscopy. *The Plant Journal*.

[Milani et al., 2014] Milani, P., Mirabet, V., Cellier, C., Rozier, F., Hamant, O., Das, P., and Boudaoud, A. (2014). Matching patterns of gene expression to mechanical stiffness at cell resolution through quantitative tandem epifluorescence and nano-indentation. *Plant Physiology*, page 114.237115.

[Mirabet et al., 2011] Mirabet, V., Das, P., Boudaoud, A., and Hamant, O. (2011). The role of mechanical forces in plant morphogenesis. *Annual Reviews of Plant Biology*, 62 :365–85.

[Moyano et al., 2015] Moyano, T. C., Vidal, E. A., Contreras-Lopez, O., and Gutierrez, R. A. (2015). Constructing simple biological networks for understanding complex high-throughput data in plants. *Methods Mol. Biol.*, 1284 :503–526.

[Müller et al., 2002] Müller, M., Dorsey, J., McMillan, L., Jagnow, R., and Cutler, B. (2002). Stable real-time deformations. In *ACM Transactions on Graphics (Proc. SIGGRAPH)/Eurographics Symposium on Computer Animation*.

[Narain et al., 2013] Narain, R., Pfaff, T., and O'Brien, J. F. (2013). Folding and crumpling adaptive sheets. *ACM Trans. Graph.*, 32(4) :51 :1–51 :8.

[Narain et al., 2012] Narain, R., Samii, A., and O'Brien, J. F. (2012). Adaptive anisotropic remeshing for cloth simulation. *ACM Trans. Graph.*, 31(6) :152 :1–152 :10.

[Newman, 2005] Newman, T. J. (2005). Modeling multicellular systems using subcellular elements. *Math Biosci Eng*, 2(3) :613–624.

[Niklas, 1992] Niklas, K. (1992). *Plant Biomechanics, An Engineering Approach to Plant Form and Function*. The University of Chicago Press.

[Niklas and jr, 1997] Niklas, K. J. and jr, D. J. P. (1997). The role of the epidermis as a stiffening agent in tulipa (liliaceae) stems. *American Journal of Botany*, page 735–744.

[Onoda et al., 2015] Onoda, Y., Schieving, F., and Anten, N. P. (2015). A novel method of measuring leaf epidermis and mesophyll stiffness shows the ubiquitous nature of the sandwich structure of leaf laminas in broad-leaved angiosperm species. *Journal of Experimental Botany*.

[Peak et al.,] Peak, D., West, J. D., Messinger, S. M., and A., M. K.

[Peaucelle et al., 2011] Peaucelle, A., Braybrook, S., Guillou, L. L., Bron, E., Kuhlemeier, C., and Höfte, H. (2011). Pectin-induces changes in cell wall mechanics underlie organ initiation in arabidopsis. *Current Biology*, pages 1720–1726.

[Picioreanu et al., 2001] Picioreanu, C., Van Loosdrecht, M. C. M., and Heijnen, J. J. (2001). Two-Dimensional Model of Biofilm Detachment Caused by Internal Stress from Liquid Flow. *BioTechnology and BioEngineering*, (2).

[Press et al., 2007] Press, W. H., Teukolsky, S., Vetterling, W., and Flannery, B. (2007). *Numerical Recipes in C++*. Cambridge University Press.

[Prusinkiewicz and Lindenmayer, 1990] Prusinkiewicz, P. and Lindenmayer, A. (1990). *The Algorithmic Beauty of Plants*. Springer-Verlag.

[P.Volino and Magnenat-Thalmann, 2006] P.Volino and Magnenat-Thalmann, N. (2006). Simple linear bending stiffness in particle systems. *Eurographics/ ACM SIGGRAPH Symposium on Computer Animation*.

[Radotic et al., 2012] Radotic, K., Roduit, C., Simonovic, J., Hornitschek, P., Frankhauser, C., Mutavdzic, D., Steinbach, G., Dietler, G., and Kasas, S. (2012). Atomic force microscopy stiffness tomography on living arabidopsis thaliana cells reveals the mechanical properties of surface and deep cell-wall layers during growth. *Biophysical Journal*, pages 386–394.

[Ranft et al., 2010] Ranft, J., Basan, M., Elgeti, J., Joanny, J. F., Prost, J., and Julicher, F. (2010). Fluidization of tissues by cell division and apoptosis. *Proc. Natl. Acad. Sci. U.S.A.*, 107(49) :20863–20868.

[Rejniak and Anderson, 2008] Rejniak, K. A. and Anderson, A. R. (2008). A computational study of the development of epithelial acini : I. Sufficient conditions for the formation of a hollow structure. *Bull. Math. Biol.*, 70(3) :677–712.

[Rémillard and Kry, 2013] Rémillard, O. and Kry, P. G. (2013). Embedded thin shells for wrinkle simulation. *ACM Trans. Graph.*, 32(4) :50 :1–50 :8.

[Roduit et al., 2009] Roduit, C., Sekatski, S., Dietler, G., Catsicas, S., Lafont, F., and Kasas, S. (2009). Stiffness tomography by atomic force microscopy. *Biophysical Journal*, pages 674–677.

[Rohmer et al., 2010] Rohmer, D., Popa, T., Cani, M.-P., Hahmann, S., and Sheffer, A. (2010). Animation wrinkling : Augmenting coarse cloth simulations with realistic-looking wrinkles. In *ACM Transactions on Graphics (Proc. SIGGRAPH Asia)*.

[Routier-Kierzkowska and Smith, 2013] Routier-Kierzkowska, A.-L. and Smith, R. S. (2013). Measuring the mechanics of morphogenesis. *Current Opinion in Plant Biology*, pages 25–32.

[Sandersius and Newman, 2008] Sandersius, S. A. and Newman, T. J. (2008). Modeling cell rheology with the Subcellular Element Model. *Phys Biol*, 5(1) :015002.

[Schmidt et al., 2014] Schmidt, T., Pasternak, T., Liu, K., Blein, T., Aubry-Hivet, D., Dovzhenko, A., Duerr, J., Teale, W., Ditengou, F. A., Burkhardt, H., Ronneberger, O., and Palme, K. (2014). The irocs toolbox - 3d analysis of the plant root apical meristem at cellular resolution. *Plant J*.

[Seiler et al., 2012] Seiler, M., Spillmann, J., and Harders, M. (2012). Enriching coarse interactive elastic objects with high-resolution data-driven deformations. In *ACM Transactions on Graphics (Proc. SIGGRAPH)/Eurographics Symposium on Computer Animation*.

[Shapiro et al., 2013] Shapiro, B. E., Meyerowitz, E. M., and Mjolsness, E. (2013). Using cellzilla for plant growth simulations at the cellular level. *Front Plant Sci*, 4 :408.

[Sifakis et al., 2007] Sifakis, E., Shinar, T., Irving, G., and Fedkiw, R. (2007). *Hybrid Simulation of Deformable Solids*. ACM Transactions on Graphics (Proc. SIGGRAPH)/Eurographics Symposium on Computer Animation.

[Smith et al., 2012] Smith, A. M., Baker, R. E., Kay, D., and Maini, P. K. (2012). Incorporating chemical signalling factors into cell-based models of growing epithelial tissues. *J Math Biol*, 65(3) :441–463.

[Szabó et al., 2004] Szabó, B., Düster, A., and Rank, E. (2004). The p-version of the finite element method. *Encyclopedia of computational mechanics*.

[Tanaka et al., 2015] Tanaka, S., Sichau, D., and Iber, D. (2015). LBIBCell : a cell-based simulation environment for morphogenetic problems. *Bioinformatics*, 31(14) :2340–2347.

[Terzopoulos and Metaxas, 1990] Terzopoulos, D. and Metaxas, D. (1990). Dynamic 3d models with local and global deformations : deformable superquadrics. In *Computer Vision, 1990. Proceedings, Third International Conference on*, pages 606–615.

[Terzopoulos and Witkin, 1988] Terzopoulos, D. and Witkin, A. (1988). Physically based models with rigid and deformable components. *Computer Graphics and Applications, IEEE*, 8(6) :41–51.

[Traas and Moneger, 2010] Traas, J. and Moneger, F. (2010). Systems biology of organ initiation at the shoot apex. *Plant Physiol.*, 152(2) :420–427.

[Twigg and Kačić-Alesić, 2010] Twigg, C. D. and Kačić-Alesić, Z. (2010). Point cloud glue : Constraining simulations using the procrustes transform. In *ACM Transactions on Graphics (Proc. SIGGRAPH)/Eurographics Symposium on Computer Animation*.

[Vella et al., 2012a] Vella, D., Ajdari, A., Vaziri, A., and Boudaoud, A. (2012a). Indentation of ellipsoidal and cilindrical elastic shells. *Phisical Review Letters*.

[Vella et al., 2012b] Vella, D., Ajdari, A., Vaziri, A., and Boudaoud, A. (2012b). The indentation of pressurized elastic shells : from polymeric capsules to yeast cells. *Journal of the Royal Society Interface*, pages 448–455.

[Wang et al., 2010] Wang, H., Hecht, F., Ramamoorthi, R., and O'Brien, J. (2010). Example-based wrinkle synthesis for clothing animation. In *ACM Transactions on Graphics (Proc. SIGGRAPH)*.

[Weliky et al., 1991] Weliky, M., Minsuk, S., Keller, R., and Oster, G. (1991). Notochord morphogenesis in Xenopus laevis : simulation of cell behavior underlying tissue convergence and extension. *Development*, 113(4) :1231–1244.

[Weliky and Oster, 1990] Weliky, M. and Oster, G. (1990). The mechanical basis of cell rearrangement. I. Epithelial morphogenesis during Fundulus epiboly. *Development*, 109(2) :373–386.

[Wicke et al., 2010] Wicke, M., Ritchie, D., Klingner, B. M., Burke, S., Shewchuk, J. R., and O'Brien, J. F. (2010). Dynamic local remeshing for elastoplastic simulation. *ACM Trans. Graph.*, 29(4) :49 :1–49 :11.

[Wojtan et al., 2011] Wojtan, C., Müller-Fischer, M., and Brochu, T. (2011). Liquid simulation with mesh-based surface tracking. In *ACM SIGGRAPH 2011 Courses*, SIGGRAPH '11, pages 8 :1–8 :84, New York, NY, USA. ACM.

[Wojtan and Turk, 2008] Wojtan, C. and Turk, G. (2008). Fast viscoelastic behavior with thin features. *ACM Trans. Graph.*, 27(3) :47 :1–47 :8.

[Yadav et al., 2013] Yadav, R., Perales, M., Gruel, J., Ohno, C., Heisler, M., Girke, T., Jönsson, H., , and Reddy, G. (2013). Plant stem cell maintenance involves direct transcriptional repression of differentiation program. *Molecular Systems Biology*, page 9 :654.

[Zienkiewicz and Cheung, 1967] Zienkiewicz, O. C. and Cheung, Y. K. (1967). *The finite element method in structural and continuum mechanics*. McGraw-Hill Publ.

[Zurdo et al., 2013] Zurdo, J. S., Brito, J. P., and Otaduy, M. A. (2013). Animating wrinkles by example on non-skinned cloth. *IEEE Transactions on Visualization and Computer Graphics*, 19(1).